Maximally localized Wannier functions: Theory and applications

Nicola Marzari

Theory and Simulation of Materials (THEOS), École Polytechnique Fédérale de Lausanne, Station 12, 1015 Lausanne, Switzerland

Arash A. Mostofi

Departments of Materials and Physics, and the Thomas Young Centre for Theory and Simulation of Materials, Imperial College London, London SW7 2AZ, United Kingdom

Jonathan R. Yates

Department of Materials, University of Oxford, Parks Road, Oxford OX1 3PH, United Kingdom

Ivo Souza

Centro de Física de Materiales (CSIC) and DIPC, Universidad del País Vasco, 20018 San Sebastián, Spain and Ikerbasque Foundation, 48011 Bilbao, Spain

David Vanderbilt

Department of Physics and Astronomy, Rutgers University, Piscataway, New Jersey 08854-8019, USA

The electronic ground state of a periodic system is usually described in terms of extended Bloch orbitals, but an alternative representation in terms of localized "Wannier functions" was introduced by Gregory Wannier in 1937. The connection between the Bloch and Wannier representations is realized by families of transformations in a continuous space of unitary matrices, carrying a large degree of arbitrariness. Since 1997, methods have been developed that allow one to iteratively transform the extended Bloch orbitals of a first-principles calculation into a unique set of *maximally localized* Wannier functions, accomplishing the solid-state equivalent of constructing localized molecular orbitals, or "Boys orbitals" as previously known from the chemistry literature. These developments are reviewed here, and a survey of the applications of these methods is presented. This latter includes a description of their use in analyzing the nature of chemical bonding, or as a local probe of phenomena related to electric polarization and orbital magnetization. Wannier interpolation schemes are also reviewed, by which quantities computed on a coarse reciprocal-space mesh can be used to interpolate onto much finer meshes at low cost, and applications in which Wannier functions are used as efficient basis functions are discussed. Finally the construction and use of Wannier functions outside the context of electronic-structure theory is presented, for cases that include phonon excitations, photonic crystals, and cold-atom optical lattices.

PACS numbers: 71.15.Ap, 71.15.Dx, 71.23.An, 77.22.−d

CONTENTS

I. INTRODUCTION

In the independent-particle approximation, the electronic ground state of a system is determined by specifying a set of one-particle orbitals and their occupations. For the case of a periodic system, these one-particle orbitals are normally taken to be the Bloch functions $\psi_{n\mathbf{k}}(\mathbf{r})$ that are labeled, according to Bloch's theorem, by a crystal momentum $\mathbf{k}$ lying inside the Brillouin zone (BZ) and a band index n. Although this choice is by far the most widely used in electronic-structure calculations, alternative representations are possible. In particular, to arrive at the Wannier representation (Wannier, 1937; Kohn, 1959; des Cloizeaux, 1963), one carries out a unitary transformation from the Bloch functions to a set of localized "Wannier functions" (WFs) labeled by a cell index $\mathbf{R}$ and a bandlike index n, such that in a crystal the WFs at different $\mathbf{R}$ are translational images of one another. Unlike Bloch functions, WFs are not eigenstates of the Hamiltonian; in selecting them, one trades off localization in energy for localization in space.

In the earlier solid-state theory literature, WFs were typically introduced in order to carry out some formal derivation, for example, of the effective-mass treatment of electron dynamics, or of an effective spin Hamiltonian, but actual calculations of the WFs were rarely performed. The history is rather different in the chemistry literature, where "localized molecular orbitals" (LMOs) (Boys, 1960, 1966; Foster and Boys, 1960a, 1960b; Edmiston and Ruedenberg, 1963) have played a significant role in computational chemistry since its early days. Chemists have emphasized that such a representation can provide an insightful picture of the nature of the chemical bond in a material, otherwise missing from the picture of extended eigenstates, or can serve as a compact basis set for high-accuracy calculations.

The actual implementation of Wannier's vision in the context of first-principles electronic-structure calculations, such as those carried out in the Kohn-Sham framework of density-functional theory (DFT) (Kohn and Sham, 1965), has instead been slower to unfold. A major reason for this is that WFs are strongly nonunique. This is a consequence of the phase indeterminacy that Bloch orbitals $\psi_{n\mathbf{k}}$ have at every wave vector $\mathbf{k}$, or, more generally, the "gauge" indeterminacy associated with the freedom to apply any arbitrary unitary transformation to the occupied Bloch states at each $\mathbf{k}$. This second indeterminacy is all the more troublesome in the common case of degeneracy of the occupied bands at certain high-symmetry points in the Brillouin zone, making a partition into separate "bands," that could separately be transformed into Wannier functions, problematic. Therefore, even before one could attempt to compute the WFs for a given material, one has first to resolve the question of which states to use to compute WFs.

An important development in this regard was the introduction by Marzari and Vanderbilt (1997) of a "maximal-localization" criterion for identifying a unique set of WFs for a given crystalline insulator. The approach is similar in spirit to the construction of LMOs in chemistry, but its implementation in the solid-state context required significant developments, due to the ill-conditioned nature of the position operator in periodic systems (Nenciu, 1991), that was clarified in the context of the "modern theory" of polarization (King-Smith and Vanderbilt, 1993; Resta, 1994). Marzari and Vanderbilt showed that the minimization of a localization functional corresponding to the sum of the second-moment spread of each Wannier charge density about its own center of charge was both formally attractive and computationally tractable. In a related development, Souza, Marzari, and Vanderbilt (2001) generalized the method to handle the

case in which one wants to construct a set of WFs that spans a subspace containing, e.g., the partially occupied bands of a metal.

These developments touched off a transformational shift in which the computational electronic-structure community started constructing maximally localized WFs (MLWFs) explicitly and using these for different purposes. The reasons are manifold: WFs, akin to LMOs in molecules, provide an insightful chemical analysis of the nature of bonding, and its evolution during, say, a chemical reaction. As such, they have become an established tool in the postprocessing of electronic-structure calculations. More interestingly, there are formal connections between the centers of charge of the WFs and the Berry phases of the Bloch functions as they are carried around the Brillouin zone. This connection is embodied in the microscopic modern theory of polarization, alluded to above, and has led to important advances in the characterization and understanding of dielectric response and polarization in materials. Of broader interest to the entire condensed-matter community is the use of WFs in the construction of model Hamiltonians for, e.g., correlated-electron and magnetic systems. An alternative use of WFs as localized, transferable building blocks has taken place in the theory of ballistic (Landauer) transport, where Green's functions and self-energies can be constructed effectively in a Wannier basis, or that of first-principles tight-binding (TB) Hamiltonians, where chemically accurate Hamiltonians are constructed directly on the Wannier basis, rather than fitted or inferred from macroscopic considerations. Finally, the ideas that were developed for electronic WFs have also seen application in very different contexts. For example, MLWFs have been used in the theoretical analysis of phonons, photonic crystals, cold-atom lattices, and the local dielectric responses of insulators.

Here we review these developments. We first introduce the transformation from Bloch functions to WFs in Sec. II, discussing their gauge freedom and the methods developed for constructing WFs through projection or maximal localization. A "disentangling procedure" for constructing WFs for a nonisolated set of bands (e.g., in metals) is also described. In Sec. III we discuss variants of these procedures in which different localization criteria or different algorithms are used, and discuss the relationship to "downfolding" and linear-scaling methods. Section IV describes how the calculation of WFs has proved to be a useful tool for analyzing the nature of the chemical bonding in crystalline, amorphous, and defective systems. Of particular importance is the ability to use WFs as a local probe of electric polarization, as described in Sec. V. There we also discuss how the Wannier representation has been useful in describing orbital magnetization, NMR chemical shifts, orbital magnetoelectric responses, and topological insulators (TIs). Section VI describes Wannier interpolation schemes, by which quantities computed on a relatively coarse **k**-space mesh can be used to interpolate faithfully onto an arbitrarily fine **k**-space mesh at relatively low cost. In Sec. VII we discuss applications in which the WFs are used as an efficient basis for the calculations of quantum-transport properties, the derivation of semiempirical potentials, and for describing strongly correlated systems. Section VIII contains a brief discussion of the construction

and use of WFs in contexts other than electronic-structure theory, including for phonons in ordinary crystals, photonic crystals, and cold atoms in optical lattices. Finally, Sec. IX provides a short summary and conclusions.

II. REVIEW OF BASIC THEORY

A. Bloch functions and Wannier functions

Electronic-structure calculations are often carried out using periodic boundary conditions. This is the most natural choice for the study of perfect crystals, and also applies to the common use of periodic supercells for the study of non-periodic systems such as liquids, interfaces, and defects. The one-particle effective Hamiltonian H then commutes with the lattice-translation operator $T_{\mathbf{R}}$, allowing one to choose as common eigenstates the Bloch orbitals $|\psi_{n\mathbf{k}}\rangle$:

$$[H, T_{\mathbf{R}}] = 0 \Rightarrow \psi_{n\mathbf{k}}(\mathbf{r}) = u_{n\mathbf{k}}(\mathbf{r})e^{i\mathbf{k}\cdot\mathbf{r}}, \qquad (1)$$

where $u_{n\mathbf{k}}(\mathbf{r})$ has the periodicity of the Hamiltonian.

Several Bloch functions are sketched on the left-hand side of Fig. 1 for a toy model in which the band of interest is composed of p-like orbitals centered on each atom. We suppose that this band is an isolated band, i.e., it remains separated by a gap from the bands below and above at all **k**. Since Bloch functions at different **k** have different envelope functions $e^{i\mathbf{k}\cdot\mathbf{r}}$, one can expect to be able to build a localized "wave packet" by superposing Bloch functions of different **k**. To get a localized wave packet in real space, we need to use a very broad superposition in **k** space. But **k** lives in the periodic Brillouin zone, so the best we can do is to choose
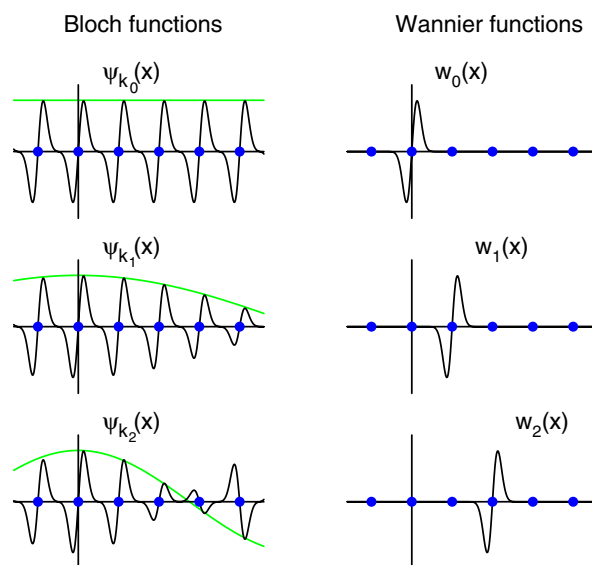
FIG. 1 (color online). Transformation from Bloch functions to Wannier functions (WFs). Left: Real-space representation of three of the Bloch functions $e^{ikx}u_k(x)$ associated with a single band in 1D, for three different values of the wave vector k. Filled circles indicate lattice vectors, and thin lines indicate the e^{ikx} envelopes of each Bloch function. Right: WFs associated with the same band, forming periodic images of one another. The two sets of Bloch functions at every k in the Brillouin zone and WFs at every lattice vector span the same Hilbert space.

equal amplitudes all across the Brillouin zone. Thus, we can construct

$$w_0(\mathbf{r}) = \frac{V}{(2\pi)^3} \int_{\text{BZ}} d\mathbf{k}\, \psi_{n\mathbf{k}}(\mathbf{r}), \qquad (2)$$

where V is the real-space primitive cell volume and the integral is carried over the BZ. (See Sec. II.A.3 for normalization conventions.) Equation (2) can be interpreted as the WF located in the home unit cell, as sketched in the top-right panel of Fig. 1.

More generally, we can insert a phase factor $e^{-i\mathbf{k}\cdot\mathbf{R}}$ into the integrand of Eq. (2), where $\mathbf{R}$ is a real-space lattice vector; this has the effect of translating the real-space WF by $\mathbf{R}$, generating additional WFs such as w_1 and w_2 sketched in Fig. 1. Switching to the Dirac bra-ket notation and introducing the notation that $\mathbf{R}n$ refers to the WF $w_{n\mathbf{R}}$ in cell $\mathbf{R}$ associated with band n, WFs can be constructed according to (Wannier, 1937)

$$|\mathbf{R}n\rangle = \frac{V}{(2\pi)^3} \int_{\text{BZ}} d\mathbf{k}\, e^{-i\mathbf{k}\cdot\mathbf{R}} |\psi_{n\mathbf{k}}\rangle. \qquad (3)$$

It is easily shown that the $|\mathbf{R}n\rangle$ form an orthonormal set (see Sec. II.A.3) and that two WFs $|\mathbf{R}n\rangle$ and $|\mathbf{R}'n\rangle$ transform into each other under translation by the lattice vector $\mathbf{R} - \mathbf{R}'$ (Blount, 1962). Equation (3) takes the form of a Fourier transform, and its inverse transform is

$$|\psi_{n\mathbf{k}}\rangle = \sum_{\mathbf{R}} e^{i\mathbf{k}\cdot\mathbf{R}} |\mathbf{R}n\rangle \qquad (4)$$

(see Sec. II.A.3). Any of the Bloch functions on the left side of Fig. 1 can thus be built up by linearly superposing the WFs shown on the right side, when the appropriate phases $e^{i\mathbf{k}\cdot\mathbf{R}}$ are used.

The transformations of Eqs. (3) and (4) constitute a unitary transformation between Bloch and Wannier states. Thus, both sets of states provide an equally valid description of the band subspace, even if the WFs are not Hamiltonian eigenstates. For example, the charge density obtained by summing the squares of the Bloch functions $|\psi_{n\mathbf{k}}\rangle$ or the WFs $|\mathbf{R}n\rangle$ is identical; a similar reasoning applies to the trace of any one-particle operator. The equivalence between the Bloch and Wannier representations can also be made manifest by expressing the band projection operator P in both representations, i.e., as

$$P = \frac{V}{(2\pi)^3} \int_{\text{BZ}} d\mathbf{k} |\psi_{n\mathbf{k}}\rangle\langle\psi_{n\mathbf{k}}| = \sum_{\mathbf{R}} |\mathbf{R}n\rangle\langle\mathbf{R}n|. \qquad (5)$$

WFs thus provide an attractive option for representing the space spanned by a Bloch band in a crystal, being localized while still carrying the same information contained in the Bloch functions.

1. Gauge freedom

The theory of WFs is made more complex by the presence of a "gauge freedom" that exists in the definition of the $\psi_{n\mathbf{k}}$. In fact, we can replace

$$|\tilde{\psi}_{n\mathbf{k}}\rangle = e^{i\varphi_n(\mathbf{k})} |\psi_{n\mathbf{k}}\rangle, \qquad (6)$$

or, equivalently,

$$|\tilde{u}_{n\mathbf{k}}\rangle = e^{i\varphi_n(\mathbf{k})} |u_{n\mathbf{k}}\rangle, \qquad (7)$$

without changing the physical description of the system, with $\varphi_n(\mathbf{k})$ being any real function that is periodic in reciprocal space.[1] A *smooth* gauge could, e.g., be defined such that $\nabla_{\mathbf{k}} |u_{n\mathbf{k}}\rangle$ is well defined at all $\mathbf{k}$. Henceforth we assume that the Bloch functions on the right-hand side of Eq. (3) belong to a smooth gauge, since we would not get well-localized WFs on the left-hand side otherwise. This is typical of Fourier transforms: the smoother the reciprocal-space object, the more localized the resulting real-space object, and vice versa.

One way to see this explicitly is to consider the $\mathbf{R} = 0$ home cell $w_{n0}(\mathbf{r})$ evaluated at a distant point $\mathbf{r}$; using Eq. (1) in Eq. (3), this is given by $\int_{\text{BZ}} u_{n\mathbf{k}}(\mathbf{r}) e^{i\mathbf{k}\cdot\mathbf{r}} d\mathbf{k}$, which will be small due to cancellations arising from the rapid variation of the exponential factor, provided that $u_{n\mathbf{k}}$ is a smooth function of $\mathbf{k}$ (Blount, 1962).

It is important to realize that the gauge freedom of Eqs. (6) and (7) propagates into the WFs. That is, different choices of smooth gauge correspond to different sets of WFs having in general different shapes and spreads. In this sense, the WFs are "more nonunique" than the Bloch functions, which acquire only a phase change. We also emphasize that there is no "preferred gauge" assigned by the Schrödinger equation to the Bloch orbitals. Thus, the nonuniqueness of the WFs resulting from Eq. (3) is unavoidable.

2. Multiband case

Before discussing how this nonuniqueness might be resolved, we first relax the condition that band n be a single isolated band, and consider instead a manifold of J bands that remain separated with respect to any lower or higher bands outside the manifold. Internal degeneracies and crossings among the J bands may occur in general. In the simplest case this manifold corresponds to the occupied bands of an insulator, but more generally it consists of any set of bands that is separated by a gap from both lower and higher bands everywhere in the Brillouin zone. Traces over this band manifold are invariant with respect to any unitary transformation among the J Bloch orbitals at a given wave vector, so it is natural to generalize the notion of a "gauge transformation" to

$$|\tilde{\psi}_{n\mathbf{k}}\rangle = \sum_{m=1}^{J} U_{mn}^{(\mathbf{k})} |\psi_{m\mathbf{k}}\rangle. \qquad (8)$$

Here $U_{mn}^{(\mathbf{k})}$ is a unitary matrix of dimension J that is periodic in $\mathbf{k}$, with Eq. (6) corresponding to the special case of a diagonal U matrix. It follows that the projection operator onto this band manifold at wave vector $\mathbf{k}$

$$P_{\mathbf{k}} = \sum_{n=1}^{J} |\psi_{n\mathbf{k}}\rangle\langle\psi_{n\mathbf{k}}| = \sum_{n=1}^{J} |\tilde{\psi}_{n\mathbf{k}}\rangle\langle\tilde{\psi}_{n\mathbf{k}}| \qquad (9)$$

---

[1] More precisely, the condition is that $\varphi_n(\mathbf{k}+\mathbf{G}) = \varphi_n(\mathbf{k}) + \mathbf{G}\cdot\Delta\mathbf{R}$ for any reciprocal-lattice translation $\mathbf{G}$, where $\Delta\mathbf{R}$ is a real-space lattice vector. This allows for the possibility that φ_n may shift by 2π times an integer upon translation by $\mathbf{G}$; the vector $\Delta\mathbf{R}$ expresses the corresponding shift in the position of the resulting WF.
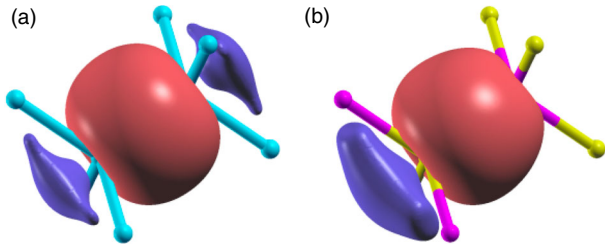
FIG. 2 (color online). Maximally localized Wannier functions (MLWFs) constructed from the four valence bands of Si (a) and GaAs [(b); Ga at upper right, As at lower left], displaying the character of σ-bonded combinations of sp^3 hybrids. Isosurfaces of different shades of gray correspond to two opposite values for the amplitudes of the real-valued MLWFs.

is invariant, even though the $|\tilde{\psi}_{n\mathbf{k}}\rangle$ resulting from Eq. (8) are no longer generally eigenstates of H, and n is no longer a band index in the usual sense.

Our goal is again to construct WFs out of these transformed Bloch functions using Eq. (3). Figures 2(a) and 2(b) show, for example, what the result might eventually look like for the case of the four occupied valence bands of Si or GaAs, respectively. From these four bands, one obtains four equivalent WFs per unit cell, each localized on one of the four nearest-neighbor Si-Si or Ga-As bonds. The presence of a bond-centered inversion symmetry for Si, but not GaAs, is clearly reflected in the shapes of the WFs.

Again, we emphasize that the gauge freedom expressed in Eq. (8) implies that the WFs are strongly nonunique. This is illustrated in Fig. 3, which shows an alternative construction of WFs for GaAs. The WF on the left was constructed from the lowest valence band $n = 1$, while the one on the right is one of three constructed from bands $n = 2$–4. The former has primarily As s character and the latter has primarily As p character, although both (and especially the latter) contain some Ga s and p character as well. The WFs of Figs. 2(b) and 3 are related to each other by a certain manifold of 4×4 unitary matrices $U_{nm}^{(\mathbf{k})}$ relating their Bloch transforms in the manner of Eq. (8).

However, before we can arrive at well-localized WFs such as those shown in Figs. 2 and 3, we again have to address questions of smoothness of the gauge choice expressed in Eq. (8). This issue is even more profound in the present multiband case, since this smoothness criterion is generally *incompatible* with the usual construction of Bloch functions. That is, if we simply insert the usual Bloch functions $|\psi_{n\mathbf{k}}\rangle$, defined to be eigenstates of H, into the right-hand side of Eq. (3), it is generally not possible to produce well-localized WFs. The problem arises when there are degeneracies among the bands in question at certain locations in the Brillouin
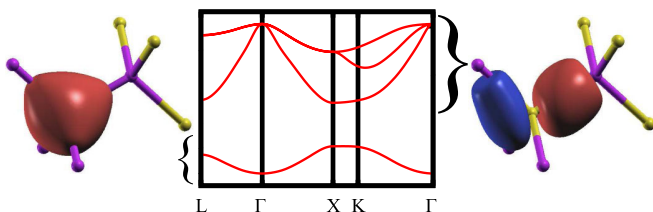
zone. Consider, for example, what happens if we try to construct a single WF from the highest occupied band $n = 4$ in GaAs. This would be doomed to failure, since this band becomes degenerate with bands two and three at the zone center Γ as shown in Fig. 3. As a result, band four is nonanalytic in $\mathbf{k}$ in the vicinity of Γ. The Fourier transform of Eq. (3) would then result in a poorly localized object having power-law tails in real space.

In such cases, therefore, the extra unitary mixing expressed in Eq. (8) is mandatory, even if it may be optional in the case of a set of discrete bands that do not touch anywhere in the BZ. So, generally speaking, our procedure must be that we start from a set of Hamiltonian eigenstates $|\psi_{n\mathbf{k}}\rangle$ that are not *per se* smooth in $\mathbf{k}$, and introduce unitary rotations $U_{mn}^{(\mathbf{k})}$ that "cancel out" the discontinuities in such a way that smoothness is restored, i.e., that the resulting $|\tilde{\psi}_{n\mathbf{k}}\rangle$ of Eq. (8) obey the smoothness condition that $\nabla_{\mathbf{k}}|\tilde{\psi}_{n\mathbf{k}}\rangle$ remains regular at all $\mathbf{k}$. Then, when these $|\tilde{\psi}_{n\mathbf{k}}\rangle$ are inserted into Eq. (3) in place of the $|\psi_{n\mathbf{k}}\rangle$, well-localized WFs should result. Explicitly, this results in WFs constructed according to

$$|\mathbf{R}n\rangle = \frac{V}{(2\pi)^3} \int_{\mathrm{BZ}} d\mathbf{k}\, e^{-i\mathbf{k}\cdot\mathbf{R}} \sum_{m=1}^{J} U_{mn}^{(\mathbf{k})} |\psi_{m\mathbf{k}}\rangle. \tag{10}$$

The question remains how to choose the unitary rotations $U_{mn}^{(\mathbf{k})}$ so as to accomplish this task. We will see that one way to do this is to use a projection technique, as outlined in Sec. II.A.3. Ideally, however, we want the construction to result in WFs that are "maximally localized" according to some criterion. Methods for accomplishing this are discussed in Sec. II.C

3. Normalization conventions

In the above equations, formulated for continuous $\mathbf{k}$, we adopted the convention that Bloch functions are normalized to one unit cell $\int_V d\mathbf{r}\, |\psi_{n\mathbf{k}}(\mathbf{r})|^2 = 1$, even though they extend over the entire crystal. We also define $\langle f|g\rangle$ as the integral of f^*g over all space. With this notation, $\langle \psi_{n\mathbf{k}}|\psi_{n\mathbf{k}}\rangle$ is not unity; instead, it diverges according to the rule

$$\langle \psi_{n\mathbf{k}}|\psi_{m\mathbf{k}'}\rangle = \frac{(2\pi)^3}{V} \delta_{nm} \delta^3(\mathbf{k}-\mathbf{k}'). \tag{11}$$

With these conventions it is easy to check that the WFs in Eqs. (3) and (4) are properly normalized, i.e., $\langle \mathbf{R}n|\mathbf{R}'m\rangle = \delta_{\mathbf{R}\mathbf{R}'}\delta_{nm}$.

It is often more convenient to work on a discrete uniform $\mathbf{k}$ mesh instead of continuous $\mathbf{k}$ space.[2] Letting N be the number of unit cells in the periodic supercell, or, equivalently, the number of mesh points in the BZ, it is possible to keep the conventions close to the continuous case by defining the Fourier transform pair as

---

[2] The discretization of $\mathbf{k}$ space amounts to imposing periodic boundary conditions on the Bloch wave functions over a supercell in real space. Thus, it should be kept in mind that the WFs given by Eqs. (12) and (14) are not truly localized, as they also display the supercell periodicity (and are normalized to a supercell volume). Under these circumstances the notion of "Wannier localization" refers to localization within one supercell, which is meaningful for supercells chosen large enough to ensure negligible overlap between a WF and its periodic images.

FIG. 3 (color online). MLWFs constructed from the s band (left) or from the three p bands (right) of GaAs.

$$|\psi_{n\mathbf{k}}\rangle = \sum_{\mathbf{R}} e^{i\mathbf{k}\cdot\mathbf{R}}|\mathbf{R}n\rangle$$

$$\Updownarrow \qquad\qquad\qquad (12)$$

$$|\mathbf{R}n\rangle = \frac{1}{N}\sum_{\mathbf{k}} e^{-i\mathbf{k}\cdot\mathbf{R}}|\psi_{n\mathbf{k}}\rangle$$

with $\langle\psi_{n\mathbf{k}}|\psi_{m\mathbf{k}'}\rangle = N\delta_{nm}\delta_{\mathbf{k}\mathbf{k}'}$, so that Eq. (5) becomes, after generalizing to the multiband case,

$$P = \frac{1}{N}\sum_{n\mathbf{k}}|\psi_{n\mathbf{k}}\rangle\langle\psi_{n\mathbf{k}}| = \sum_{n\mathbf{R}}|\mathbf{R}n\rangle\langle\mathbf{R}n|. \qquad (13)$$

Another commonly used convention is to write

$$|\psi_{n\mathbf{k}}\rangle = \frac{1}{\sqrt{N}}\sum_{\mathbf{R}} e^{i\mathbf{k}\cdot\mathbf{R}}|\mathbf{R}n\rangle$$

$$\Updownarrow \qquad\qquad\qquad (14)$$

$$|\mathbf{R}n\rangle = \frac{1}{\sqrt{N}}\sum_{\mathbf{k}} e^{-i\mathbf{k}\cdot\mathbf{R}}|\psi_{n\mathbf{k}}\rangle,$$

with $\langle\psi_{n\mathbf{k}}|\psi_{m\mathbf{k}'}\rangle = \delta_{nm}\delta_{\mathbf{k}\mathbf{k}'}$ and Eq. (13) replaced by

$$P = \sum_{n\mathbf{k}}|\psi_{n\mathbf{k}}\rangle\langle\psi_{n\mathbf{k}}| = \sum_{n\mathbf{R}}|\mathbf{R}n\rangle\langle\mathbf{R}n|. \qquad (15)$$

In either case, it is convenient to keep the $|u_{n\mathbf{k}}\rangle$ functions normalized to the unit cell, with inner products involving them, such as $\langle u_{m\mathbf{k}}|u_{n\mathbf{k}}\rangle$, understood as integrals over one unit cell. In the case of Eq. (14), this means that $u_{n\mathbf{k}}(\mathbf{r}) = \sqrt{N}e^{-i\mathbf{k}\cdot\mathbf{r}}\psi_{n\mathbf{k}}(\mathbf{r})$.

B. Wannier functions via projection

A simple yet often effective approach for constructing a smooth gauge in $\mathbf{k}$, and a corresponding set of well-localized WFs, is by projection, an approach that finds its roots in the analysis of des Cloizeaux (1964a). Here, as discussed, e.g., in Sec. IV.G.1 of Marzari and Vanderbilt (1997), one starts from a set of J localized trial orbitals $g_n(\mathbf{r})$ corresponding to some rough guess for the WFs in the home unit cell. Returning to the continuous-$\mathbf{k}$ formulation, these $g_n(\mathbf{r})$ are projected onto the Bloch manifold at wave vector $\mathbf{k}$ to obtain

$$|\phi_{n\mathbf{k}}\rangle = \sum_{m=1}^{J}|\psi_{m\mathbf{k}}\rangle\langle\psi_{m\mathbf{k}}|g_n\rangle, \qquad (16)$$

which are typically smooth in $\mathbf{k}$ space, albeit not orthonormal. (The integral in $\langle\psi_{m\mathbf{k}}|g_n\rangle$ is over all space as usual.) We note that in actual practice such projection is achieved by first computing a matrix of inner products $(A_{\mathbf{k}})_{mn} = \langle\psi_{m\mathbf{k}}|g_n\rangle$ and then using these in Eq. (16). The overlap matrix $(S_{\mathbf{k}})_{mn} = \langle\phi_{m\mathbf{k}}|\phi_{n\mathbf{k}}\rangle_V = (A_{\mathbf{k}}^{\dagger}A_{\mathbf{k}})_{mn}$ (where subscript V denotes an integral over one cell) is then computed and used to construct the Löwdin-orthonormalized Bloch-like states

$$|\tilde{\psi}_{n\mathbf{k}}\rangle = \sum_{m=1}^{J}|\phi_{m\mathbf{k}}\rangle(S_{\mathbf{k}}^{-1/2})_{mn}. \qquad (17)$$

These $|\tilde{\psi}_{n\mathbf{k}}\rangle$ have now a smooth gauge in $\mathbf{k}$, are related to the original $|\psi_{n\mathbf{k}}\rangle$ by a unitary transformation,[3] and when

---

[3]One can prove that this transformation is unitary by performing the singular value decomposition $A = ZDW^{\dagger}$, with Z and W unitary and D real and diagonal. It follows that $A(A^{\dagger}A)^{-1/2}$ is equal to $ZW^{\dagger}$, and thus unitary.

substituted into Eq. (3) in place of the $|\psi_{n\mathbf{k}}\rangle$ result in a set of well-localized WFs. We note that the $|\tilde{\psi}_{n\mathbf{k}}\rangle$ are uniquely defined by the trial orbitals $g_n(\mathbf{r})$ and the chosen (isolated) manifold, since any arbitrary unitary rotation among the $|\psi_{n\mathbf{k}}\rangle$ orbitals cancels out exactly and does not affect the outcome of Eq. (16), thus eliminating any gauge freedom.

We emphasize that the trial functions do not need to resemble the target WFs closely; it is often sufficient to choose simple analytic functions (e.g., spherical harmonics times Gaussians) provided they are roughly located on sites where WFs are expected to be centered and have appropriate angular character. The method is successful as long as the inner-product matrix $A_{\mathbf{k}}$ does not become singular (or nearly so) for any $\mathbf{k}$, which can be ensured by checking that the ratio of maximum and minimum values of det $S_{\mathbf{k}}$ in the Brillouin zone does not become too large. For example, spherical (s-like) Gaussians located at the bond centers will suffice for the construction of well-localized WFs, akin to those shown in Fig. 2, spanning the four occupied valence bands of semiconductors such as Si and GaAs.

C. Maximally localized Wannier functions

The projection method described in Sec. II.B has been used by many (Stephan, Martin, and Drabold, 2000; Ku *et al.*, 2002; Lu *et al.*, 2004; Qian *et al.*, 2008), as has a related method involving downfolding of the band structure onto a minimal basis (Andersen and Saha-Dasgupta, 2000; Zurek, Jepsen, and Andersen, 2005); some of these approaches will also be discussed in Sec. III.B. Others made use of symmetry considerations, analyticity requirements, and variational procedures (Sporkmann and Bross, 1994, 1997; Smirnov and Usvyat, 2001). A very general and now widely used approach, however, has been that developed by Marzari and Vanderbilt (1997) in which localization is enforced by introducing a well-defined *localization criterion*, and then refining the $U_{mn}^{(\mathbf{k})}$ in order to satisfy that criterion. We first give an overview of this approach and then provide details in the following sections.

First, the localization functional

$$\Omega = \sum_{n}[\langle\mathbf{0}n|r^2|\mathbf{0}n\rangle - \langle\mathbf{0}n|\mathbf{r}|\mathbf{0}n\rangle^2] = \sum_{n}[\langle r^2\rangle_n - \bar{\mathbf{r}}_n^2] \qquad (18)$$

is defined, measuring the sum of the quadratic spreads of the J WFs in the home unit cell around their centers. This turns out to be the solid-state equivalent of the Foster-Boys criterion of quantum chemistry (Boys, 1960, 1966; Foster and Boys, 1960a, 1960b). The next step is to express Ω in terms of the Bloch functions. This requires some care, since expectation values of the position operator are not well defined in the Bloch representation. The needed formalism will be discussed briefly in Sec. II.C.1 and more extensively in Sec. V.A.1, with much of the conceptual work stemming from the earlier development of the modern theory of polarization (Blount, 1962; Resta, 1992, 1994; King-Smith and Vanderbilt, 1993; Vanderbilt and King-Smith, 1993).

Once a $\mathbf{k}$-space expression for Ω has been derived, maximally localized WFs are obtained by minimizing it with respect to the $U_{mn}^{(\mathbf{k})}$ appearing in Eq. (10). This is done as a

postprocessing step after a conventional electronic-structure calculation has been self-consistently converged and a set of ground-state Bloch orbitals $|\psi_{m\mathbf{k}}\rangle$ has been chosen once and for all. The $U_{mn}^{(\mathbf{k})}$ are then iteratively refined in a direct minimization procedure of the localization functional that is outlined in Sec. II.D. This procedure also provides the expectation values $\langle r^2\rangle_n$ and $\bar{\mathbf{r}}_n$; the latter, in particular, are the primary quantities needed to compute many of the properties, such as the electronic polarization, discussed in Sec. V. If desired, the resulting $U_{mn}^{(\mathbf{k})}$ can also be used to explicitly construct the maximally localized WFs via Eq. (10). This step is typically only necessary, however, if one wants to visualize the resulting WFs or to use them as basis functions for some subsequent analysis.

1. Real-space representation

An interesting consequence stemming from the choice of Eq. (18) as the localization functional is that it allows a natural decomposition of the functional into gauge-invariant and gauge-dependent parts. That is, we can write

$$\Omega = \Omega_{\mathrm{I}} + \tilde{\Omega}, \tag{19}$$

where

$$\Omega_{\mathrm{I}} = \sum_n \left[\langle \mathbf{0}n|r^2|\mathbf{0}n\rangle - \sum_{\mathbf{R}m} |\langle \mathbf{R}m|\mathbf{r}|\mathbf{0}n\rangle|^2 \right] \tag{20}$$

and

$$\tilde{\Omega} = \sum_n \sum_{\mathbf{R}m \neq \mathbf{0}n} |\langle \mathbf{R}m|\mathbf{r}|\mathbf{0}n\rangle|^2. \tag{21}$$

It can be shown that not only $\tilde{\Omega}$ but also Ω_{I} is *positive definite*, and moreover that Ω_{I} is *gauge invariant*, i.e., invariant under any arbitrary unitary transformation (8) of the Bloch orbitals (Marzari and Vanderbilt, 1997). This follows straightforwardly from recasting Eq. (20) in terms of the band-group projection operator P, as defined in Eq. (15), and its complement $Q = 1 - P$:

$$\Omega_{\mathrm{I}} = \sum_{n\alpha} \langle \mathbf{0}n|r_\alpha Q r_\alpha|\mathbf{0}n\rangle = \sum_\alpha \mathrm{Tr}_{\mathrm{c}}[P r_\alpha Q r_\alpha]. \tag{22}$$

The subscript "c" indicates trace per unit cell. Clearly Ω_{I} is gauge invariant, since it is expressed in terms of projection operators that are unaffected by any gauge transformation. It can also be seen to be positive definite by using the idempotency of P and Q to write $\Omega_{\mathrm{I}} = \sum_\alpha \mathrm{Tr}_{\mathrm{c}}[(P r_\alpha Q)(P r_\alpha Q)^\dagger] = \sum_\alpha \|P r_\alpha Q\|_{\mathrm{c}}^2$.

The minimization procedure of Ω thus actually corresponds to the minimization of the noninvariant part $\tilde{\Omega}$ only. At the minimum, the off-diagonal elements $|\langle \mathbf{R}m|\mathbf{r}|\mathbf{0}n\rangle|^2$ are as small as possible, realizing the best compromise in the simultaneous diagonalization, within the subspace of the Bloch bands considered, of the three position operators x, y, and z, which do not in general commute when projected onto this space.

2. Reciprocal-space representation

As shown by Blount (1962), matrix elements of the position operator between WFs take the form

$$\langle \mathbf{R}n|\mathbf{r}|\mathbf{0}m\rangle = i\frac{V}{(2\pi)^3} \int d\mathbf{k}\, e^{i\mathbf{k}\cdot\mathbf{R}} \langle u_{n\mathbf{k}}|\nabla_{\mathbf{k}}|u_{m\mathbf{k}}\rangle \tag{23}$$

and

$$\langle \mathbf{R}n|r^2|\mathbf{0}m\rangle = -\frac{V}{(2\pi)^3} \int d\mathbf{k}\, e^{i\mathbf{k}\cdot\mathbf{R}} \langle u_{n\mathbf{k}}|\nabla_{\mathbf{k}}^2|u_{m\mathbf{k}}\rangle. \tag{24}$$

These expressions provide the needed connection with our underlying Bloch formalism, since they allow one to express the localization functional Ω in terms of the matrix elements of $\nabla_{\mathbf{k}}$ and $\nabla_{\mathbf{k}}^2$. In addition, they allow one to calculate the effects on the localization of any unitary transformation of the $|u_{n\mathbf{k}}\rangle$ without having to recalculate expensive (especially when plane-wave basis sets are used) scalar products. We thus determine the Bloch orbitals $|u_{m\mathbf{k}}\rangle$ on a regular mesh of $\mathbf{k}$ points and use finite differences to evaluate the above derivatives. In particular, we make the assumption that the BZ has been discretized into a uniform Monkhorst-Pack mesh, and the Bloch orbitals have been determined on that mesh.[4]

For any $f(\mathbf{k})$ that is a smooth function of $\mathbf{k}$, it can be shown that its gradient can be expressed by finite differences as

$$\nabla f(\mathbf{k}) = \sum_{\mathbf{b}} w_b \mathbf{b}[f(\mathbf{k}+\mathbf{b}) - f(\mathbf{k})] + \mathcal{O}(b^2) \tag{25}$$

calculated on stars ("shells") of near-neighbor $\mathbf{k}$ points; here $\mathbf{b}$ is a vector connecting a $\mathbf{k}$ point to one of its neighbors and w_b is an appropriate geometric factor that depends on the number of points in the star and its geometry [see Appendix B in Marzari and Vanderbilt (1997) and Mostofi *et al.* (2008) for a detailed description]. In a similar way,

$$|\nabla f(\mathbf{k})|^2 = \sum_{\mathbf{b}} w_b[f(\mathbf{k}+\mathbf{b}) - f(\mathbf{k})]^2 + \mathcal{O}(b^3). \tag{26}$$

It now becomes straightforward to calculate the matrix elements in Eqs. (23) and (24). All the information needed for the reciprocal-space derivatives is encoded in the overlaps between Bloch orbitals at neighboring $\mathbf{k}$ points:

$$M_{mn}^{(\mathbf{k},\mathbf{b})} = \langle u_{m\mathbf{k}}|u_{n,\mathbf{k}+\mathbf{b}}\rangle. \tag{27}$$

These overlaps play a central role in the formalism, since all contributions to the localization functional can be expressed in terms of them. Thus, once the $M_{mn}^{(\mathbf{k},\mathbf{b})}$ have been calculated, no further interaction with the electronic-structure code that calculated the ground-state wave functions is necessary, making the entire Wannierization procedure a code-independent postprocessing step.[5] There is no unique form for the localization functional in terms of the overlap elements, as it is

---

[4]Even the case of Γ sampling, where the Brillouin zone is sampled with a single $\mathbf{k}$ point, is encompassed by the above formulation. In this case the neighboring $\mathbf{k}$ points are given by reciprocal-lattice vectors $\mathbf{G}$ and the Bloch orbitals differ only by phase factors $\exp(i\mathbf{G}\cdot\mathbf{r})$ from their counterparts at Γ. The algebra does become simpler, though, as discussed in Sec. II.F.2.

[5]In particular, see Ferretti *et al.* (2007) for the extension to ultrasoft pseudopotentials and the projector-augmented wave method, and Posternak *et al.* (2002), Freimuth *et al.* (2008), and Kuneš *et al.* (2010) for the full-potential linearized augmented plane-wave method.

possible to write down many alternative finite-difference expressions for $\bar{\mathbf{r}}_n$ and $\langle r^2 \rangle_n$ which agree numerically to leading order in the mesh spacing b (first and second order for $\bar{\mathbf{r}}_n$ and $\langle r^2 \rangle_n$, respectively). We give here the expressions of Marzari and Vanderbilt (1997), which have the desirable property of transforming correctly under gauge transformations that shift $|\mathbf{0}n\rangle$ by a lattice vector. They are

$$\bar{\mathbf{r}}_n = -\frac{1}{N} \sum_{\mathbf{k},\mathbf{b}} w_b \mathbf{b} \, \text{Im} \, \ln M_{nn}^{(\mathbf{k},\mathbf{b})} \tag{28}$$

[where we use, as outlined in Sec. II.A.3, the convention of Eq. (14)] and

$$\langle r^2 \rangle_n = \frac{1}{N} \sum_{\mathbf{k},\mathbf{b}} w_b \{ [1 - |M_{nn}^{(\mathbf{k},\mathbf{b})}|^2] + [\text{Im} \, \ln M_{nn}^{(\mathbf{k},\mathbf{b})}]^2 \}. \tag{29}$$

The corresponding expressions for the gauge-invariant and gauge-dependent parts of the spread functional are

$$\Omega_{\text{I}} = \frac{1}{N} \sum_{\mathbf{k},\mathbf{b}} w_b \left(J - \sum_{mn} |M_{mn}^{(\mathbf{k},\mathbf{b})}|^2 \right) \tag{30}$$

and

$$\tilde{\Omega} = \frac{1}{N} \sum_{\mathbf{k},\mathbf{b}} w_b \sum_{m \neq n} |M_{mn}^{(\mathbf{k},\mathbf{b})}|^2$$
$$+ \frac{1}{N} \sum_{\mathbf{k},\mathbf{b}} w_b \sum_n (-\text{Im} \, \ln M_{nn}^{(\mathbf{k},\mathbf{b})} - \mathbf{b} \cdot \bar{\mathbf{r}}_n)^2. \tag{31}$$

As mentioned, it is possible to write down alternative discretized expressions which agree numerically with Eqs. (28)–(31) up to the orders indicated in the mesh spacing b; at the same time, one needs to be careful in realizing that certain quantities, such as the spreads, will display slow convergence with respect to the BZ sampling (see Sec. II.F.2 for a discussion), or that some exact results (e.g., that the sum of the centers of the Wannier functions is invariant with respect to unitary transformations) might acquire some numerical noise. In particular, Stengel and Spaldin (2006a) showed how to modify the above expressions in a way that renders the spread functional strictly invariant under BZ folding.

D. Localization procedure

In order to minimize the localization functional, we consider the first-order change of the spread functional Ω arising from an infinitesimal gauge transformation $U_{mn}^{(\mathbf{k})} = \delta_{mn} + dW_{mn}^{(\mathbf{k})}$, where dW is an infinitesimal anti-Hermitian matrix, $dW^\dagger = -dW$, so that $|u_{n\mathbf{k}}\rangle \rightarrow |u_{n\mathbf{k}}\rangle + \sum_m dW_{mn}^{(\mathbf{k})} |u_{m\mathbf{k}}\rangle$. We use the convention

$$\left(\frac{d\Omega}{dW} \right)_{nm} = \frac{d\Omega}{dW_{mn}} \tag{32}$$

(note the reversal of indices) and introduce $\mathcal{A}$ and $\mathcal{S}$ as the superoperators $\mathcal{A}[B] = (B - B^\dagger)/2$ and $\mathcal{S}[B] = (B + B^\dagger)/2i$. Defining

$$q_n^{(\mathbf{k},\mathbf{b})} = \text{Im} \, \ln M_{nn}^{(\mathbf{k},\mathbf{b})} + \mathbf{b} \cdot \bar{r}_n, \tag{33}$$

$$R_{mn}^{(\mathbf{k},\mathbf{b})} = M_{mn}^{(\mathbf{k},\mathbf{b})} M_{nn}^{(\mathbf{k},\mathbf{b})*}, \tag{34}$$

$$T_{mn}^{(\mathbf{k},\mathbf{b})} = \frac{M_{mn}^{(\mathbf{k},\mathbf{b})}}{M_{nn}^{(\mathbf{k},\mathbf{b})}} q_n^{(\mathbf{k},\mathbf{b})}, \tag{35}$$

and referring to Marzari and Vanderbilt (1997) for the details, we arrive at the explicit expression for the gradient $G^{(\mathbf{k})} = d\Omega/dW^{(\mathbf{k})}$ of the spread functional Ω as

$$G^{(\mathbf{k})} = 4 \sum_{\mathbf{b}} w_b (\mathcal{A}[R^{(\mathbf{k},\mathbf{b})}] - \mathcal{S}[T^{(\mathbf{k},\mathbf{b})}]). \tag{36}$$

This gradient is used to drive the evolution of the $U_{mn}^{(\mathbf{k})}$ [and, implicitly, of the $|\mathbf{R}n\rangle$ of Eq. (10)] toward the minimum of Ω. A simple steepest-descent implementation, for example, takes small finite steps in the direction opposite to the gradient G until a minimum is reached.

For details of the minimization strategies and the enforcement of unitarity during the search, the interested reader is referred to Mostofi *et al.* (2008). We point out here, however, that most of the operations can be performed using inexpensive matrix algebra on small matrices. The most computationally demanding parts of the procedure are typically the calculation of the self-consistent Bloch orbitals $|u_{n\mathbf{k}}^{(0)}\rangle$ in the first place, and then the computation of a set of overlap matrices

$$M_{mn}^{(0)(\mathbf{k},\mathbf{b})} = \langle u_{m\mathbf{k}}^{(0)} | u_{n,\mathbf{k}+\mathbf{b}}^{(0)} \rangle \tag{37}$$

that are constructed once and for all from the $|u_{n\mathbf{k}}^{(0)}\rangle$. After every update of the unitary matrices $U^{(\mathbf{k})}$, the overlap matrices are updated with inexpensive matrix algebra

$$M^{(\mathbf{k},\mathbf{b})} = U^{(\mathbf{k})\dagger} M^{(0)(\mathbf{k},\mathbf{b})} U^{(\mathbf{k}+\mathbf{b})} \tag{38}$$

without any need to access the Bloch wave functions themselves. This not only makes the algorithm computationally fast and efficient, but also makes it independent of the basis used to represent the Bloch functions. That is, any electronic-structure code package capable of providing the set of overlap matrices $M^{(\mathbf{k},\mathbf{b})}$ can easily be interfaced to a common Wannier maximal-localization code.

E. Local minima

It should be noted that the localization functional can display, in addition to the desired global minimum, multiple local minima that do not lead to the construction of meaningful localized orbitals. Heuristically, it is also found that the WFs corresponding to these local minima are intrinsically complex, while they are found to be real, apart from a single complex phase, at the desired global minimum (provided of course that the calculations do not include spin-orbit coupling). Such observation in itself provides a useful diagnostic tool to weed out undesired solutions.

These false minima either correspond to the formation of topological defects (e.g., "vortices") in an otherwise smooth gauge field in discrete $\mathbf{k}$ space or they can arise when the branch cuts for the complex logarithms in Eqs. (28) and (29) are inconsistent, i.e., when at any given $\mathbf{k}$ point the contributions from different $\mathbf{b}$ vectors differ by random amounts of 2π in the logarithm. Since a locally appropriate choice of branch cuts can always be performed, this problem is less

severe than the topological problem. The most straightforward way to avoid local minima altogether is to initialize the minimization procedure with a gauge choice that is already fairly smooth. For this purpose, the projection method described in Sec. II.B has been found to be extremely effective. Therefore, minimization is usually preceded by a projection step, to generate a set of analytic Bloch orbitals to be further optimized, as discussed more fully by Marzari and Vanderbilt (1997) and Mostofi *et al.* (2008).

F. The limit of isolated systems or large supercells

The formulation introduced above can be significantly simplified in two important and related cases, which merit a separate discussion. The first is the case of open boundary conditions: this is the most appropriate choice for treating finite, isolated systems (e.g., molecules and clusters) using localized basis sets, and is a common approach in quantum chemistry. The localization procedure can then be entirely recast in real space and corresponds exactly to determining Foster-Boys localized orbitals. The second is the case of systems that can be described using very large periodic supercells. This is the most appropriate strategy for nonperiodic bulk systems, such as amorphous solids or liquids (see Fig. 4 for a paradigmatic example), but obviously includes also periodic systems with large unit cells. In this approach, the Brillouin zone is considered to be sufficiently small such that integrations over **k** vectors can be approximated with a single **k** point (usually at the Γ point, i.e., the origin in reciprocal space). The localization procedure in this second case is based on the procedure for periodic boundary conditions described above, but with some notable simplifications. Isolated systems can also be artificially repeated and treated using the supercell approach, although care may be needed in dealing with the long-range electrostatics if the isolated entities are charged or have significant dipole or multipolar character (Makov and Payne, 1995; Dabo *et al.*, 2008).

1. Real-space formulation for isolated systems

For an isolated system, described with open boundary conditions, all orbitals are localized to begin with, and further localization is achieved via unitary transformations within this set. We adopt a simplified notation $|\mathbf{R}n\rangle \rightarrow |w_i\rangle$ to refer
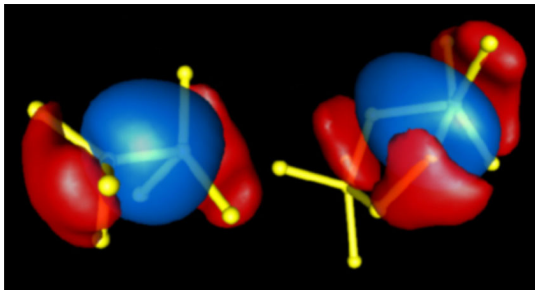

FIG. 4 (color online). MLWFs in amorphous Si, either around distorted but fourfold-coordinated atoms or in the presence of a fivefold defect. Adapted from Fornari *et al.*, 2001.

to the localized orbitals of the isolated system that will become maximally localized. We decompose again the localization functional $\Omega = \sum_i [\langle r^2 \rangle_i - \bar{\mathbf{r}}_i^2]$ into a term $\Omega_I = \sum_\alpha \mathrm{tr}[Pr_\alpha Qr_\alpha]$ (where $P = \sum_i |w_i\rangle\langle w_i|$, $Q = \mathbf{1} - P$, and "tr" refers to a sum over all the states w_i) that is invariant under unitary rotations, and a remainder $\tilde{\Omega} = \sum_\alpha \sum_{i \neq j} |\langle w_i | r_\alpha | w_j \rangle|^2$ that needs to be minimized. Defining the matrices $X_{ij} = \langle w_i | x | w_j \rangle$, $X_{D,ij} = X_{ij}\delta_{ij}$, $X' = X - X_D$ (and similarly for Y and Z), $\tilde{\Omega}$ can be rewritten as

$$\tilde{\Omega} = \mathrm{tr}[X'^2 + Y'^2 + Z'^2]. \tag{39}$$

If X, Y, and Z could be simultaneously diagonalized, then $\tilde{\Omega}$ would be minimized to zero (leaving only the invariant part). This is straightforward in one dimension, but is not generally possible in higher dimensions. The general solution to the three-dimensional problem consists instead in the optimal, but approximate, simultaneous codiagonalization of the three Hermitian matrices X, Y, and Z by a single unitary transformation that minimizes the numerical value of the localization functional. Although a formal solution to this problem is missing, implementing a numerical procedure (e.g., by steepest-descent or conjugate-gradients minimization) is fairly straightforward. It should be noted that the problem of simultaneous codiagonalization arises also in the context of multivariate analysis (Flury and Gautschi, 1986) and signal processing (Cardoso and Soulomiac, 1996), and has been recently revisited in relation to the present localization approach (Gygi, Fattebert, and Schwegler, 2003) [see also Sec. III.A in Berghold *et al.* (2000)].

To proceed further, we write

$$d\Omega = 2\,\mathrm{tr}[X'dX + Y'dY + Z'dZ], \tag{40}$$

exploiting the fact that $\mathrm{tr}[X'X_D] = 0$, and similarly for Y and Z. We then consider an infinitesimal unitary transformation $|w_i\rangle \rightarrow |w_i\rangle + \sum_j dW_{ji}|w_j\rangle$ (where dW is anti-Hermitian), from which $dX = [X, dW]$, and similarly for Y and Z. Inserting in Eq. (40) and using $\mathrm{tr}[A[B,C]] = \mathrm{tr}[C[A,B]]$ and $[X', X] = [X', X_D]$, we obtain $d\Omega = \mathrm{tr}[dWG]$ where the gradient of the spread functional $G = d\Omega/dW$ is given by

$$G = 2\{[X', X_D] + [Y', Y_D] + [Z', Z_D]\}. \tag{41}$$

The minimization can then be carried out using a procedure similar to that outlined above for periodic boundary conditions. Last, we note that minimizing $\tilde{\Omega}$ is equivalent to maximizing $\mathrm{tr}[X_D^2 + Y_D^2 + Z_D^2]$, since $\mathrm{tr}[X'X_D] = \mathrm{tr}[Y'Y_D] = \mathrm{tr}[Y'Y_D] = 0$.

2. Γ-point formulation for large supercells

A similar formulation applies in reciprocal space when dealing with isolated or very large systems in periodic boundary conditions, i.e., whenever it becomes appropriate to sample the wave functions only at the Γ point of the Brillouin zone. For simplicity, we start with the case of a simple cubic lattice of spacing L, and define the matrix

$$\mathcal{X}_{mn} = \langle w_m | e^{-2\pi i x/L} | w_n \rangle \tag{42}$$

and similarly for $\mathcal{Y}$, and $\mathcal{Z}$ [the extension to supercells of arbitrary symmetry has been derived by Silvestrelli (1999)].[6] The coordinate x_n of the nth WF center (WFC) can then be obtained from

$$x_n = -\frac{L}{2\pi} \operatorname{Im} \ln\langle w_n | e^{-i(2\pi/L)x} | w_n \rangle = -\frac{L}{2\pi} \operatorname{Im} \ln \mathcal{X}_{nn},$$
(43)

and similarly for y_n and z_n. Equation (43) has been shown by Resta (1998) to be the correct definition of the expectation value of the position operator for a system with periodic boundary conditions, and had been introduced several years ago to deal with the problem of determining the average position of a single electronic orbital in a periodic supercell (Selloni *et al.*, 1987) (the above definition becomes self-evident in the limit where w_n tends to a Dirac delta function).

Following the derivation of Sec. II.F.1, or of Silvestrelli *et al.* (1998), it can be shown that the maximum-localization criterion is equivalent to maximizing the functional

$$\Xi = \sum_{n=1}^{J}(|\mathcal{X}_{nn}|^2 + |\mathcal{Y}_{nn}|^2 + |\mathcal{Z}_{nn}|^2).$$
(44)

The first term of the gradient $d\Xi/dA_{mn}$ is given by $\mathcal{X}_{nm}(\mathcal{X}_{nn}^* - \mathcal{X}_{mm}^*) - \mathcal{X}_{mn}^*(\mathcal{X}_{mm} - \mathcal{X}_{nn})$, and similarly for the second and third terms. Again, once the gradient is determined, minimization can be performed using a steepest-descent or conjugate-gradients algorithm; as always, the computational cost of the localization procedure is small, given that it involves only small matrices of dimension $J \times J$, once the scalar products needed to construct the initial $\mathcal{X}^{(0)}$, $\mathcal{Y}^{(0)}$, and $\mathcal{Z}^{(0)}$ have been calculated, which takes an effort of order $J^2 * N_{\text{basis}}$. We note that in the limit of a single $\mathbf{k}$ point the distinction between Bloch orbitals and WFs becomes irrelevant, since no Fourier transform from $\mathbf{k}$ to $\mathbf{R}$ is involved in the transformation Eq. (10); rather, we want to find the optimal unitary matrix that rotates the ground-state self-consistent orbitals into their maximally localized representation, making this problem exactly equivalent to the one of isolated systems. Interestingly, it should also be mentioned that the local minima alluded to in Sec. II.E are typically not found when using Γ sampling in large supercells.

Before concluding, we note that care should be taken when comparing the spreads of MLWFs calculated in supercells of different sizes. The Wannier centers and the general shape of the MLWFs often converge rapidly as the cell size is increased, but even for the ideal case of an isolated molecule, the total spread Ω often displays much slower convergence. This behavior derives from the finite-difference representation of the invariant part Ω_I of the localization functional (essentially, a second derivative); while Ω_I does not enter into the localization procedure, it does contribute to the spread, and, in fact, usually represents the largest term. This slow

convergence was noted by Marzari and Vanderbilt (1997) when commenting on the convergence properties of Ω with respect to the spacing of the Monkhorst-Pack mesh and has been studied in detail by others (Umari and Pasquarello, 2003; Stengel and Spaldin, 2006a). For isolated systems in a supercell, this problem can be avoided simply by using a very large L in Eq. (43), since in practice the integrals only need to be calculated in the small region where the orbitals are nonzero (Wu, 2004). For extended bulk systems, this convergence problem can be ameliorated significantly by calculating the position operator using real-space integrals (Lee, Nardelli, and Marzari, 2005; Lee, 2006; Stengel and Spaldin, 2006a).

G. Exponential localization

The existence of exponentially localized WFs, i.e., WFs whose tails decay exponentially fast, is a famous problem in the band theory of solids, with close ties to the general properties of the insulating state (Kohn, 1964). While the asymptotic decay of a Fourier transform can be related to the analyticity of the function and its derivatives [see, e.g., Duffin (1953) and Duffin and Shaffer (1960) and references therein], proofs of exponential localization for the Wannier transform were obtained over the years only for limited cases, starting with the work of Kohn (1959), who considered a one-dimensional crystal with inversion symmetry. Other milestones include the work of des Cloizeaux (1964b), who established the exponential localization in 1D crystals without inversion symmetry and in the centrosymmetric 3D case, and the subsequent removal of the requirement of inversion symmetry in the latter case by Nenciu (1983). The asymptotic behavior of WFs was further clarified by He and Vanderbilt (2001), who found that the exponential decay is modulated by a power law. In dimensions $d > 1$ the problem is further complicated by the possible existence of band degeneracies, while the proofs of des Cloizeaux and Nenciu were restricted to isolated bands. The early work on composite bands in 3D established only the exponential localization of the projection operator P, Eq. (13), not of the WFs themselves (des Cloizeaux, 1964a).

The question of exponential decay in 2D and 3D was finally settled by Brouder *et al.* (2007) who showed, as a corollary to a theorem by Panati (2007), that a necessary and sufficient condition for the existence of exponentially localized WFs in 2D and 3D is that the so-called ''Chern invariants'' for the composite set of bands vanish identically. Panati (2007) demonstrated that this condition ensures the possibility of carrying out the gauge transformation of Eq. (8) in such a way that the resulting cell-periodic states $|\tilde{u}_{n\mathbf{k}}\rangle$ are analytic functions of $\mathbf{k}$ across the entire BZ;[7] this in turn implies the exponential falloff of the WFs given by Eq. (10).

It is natural to ask whether the MLWFs obtained by minimizing the quadratic spread functional Ω are also exponentially localized. Marzari and Vanderbilt (1997) established this in 1D by simply noting that the MLWF

---

[6] We point out that the definition of the $\mathcal{X}$, $\mathcal{Y}$, and $\mathcal{Z}$ matrices for extended systems, now common in the literature, is different from the one used in Sec. II.F.1 for the X, Y, and Z matrices for the isolated system. We preserved these two notations for consistency with published work, at the cost of making less evident the close similarities that exist between the two minimization algorithms.

[7] Conversely, nonzero Chern numbers pose an obstruction to finding a *globally* smooth gauge in $\mathbf{k}$ space. The mathematical definition of a Chern number is given in Sec. V.C.4.

construction then reduces to finding the eigenstates of the projected position operator PxP, a case for which exponential localization had already been proven (Niu, 1991). The more complex problem of demonstrating the exponential localization of MLWFs for composite bands in 2D and 3D was finally solved by Panati and Pisante (2011).

H. Hybrid Wannier functions

It is sometimes useful to carry out the Wannier transform in one spatial dimension only, leaving wave functions that are still delocalized and Bloch periodic in the remaining directions (Sgiarovello, Peressi, and Resta, 2001). Such orbitals are usually denoted as "hermaphrodite" or "hybrid" WFs. Explicitly, Eq. (10) is replaced by the hybrid WF definition

$$|l, n\mathbf{k}_\parallel\rangle = \frac{c}{2\pi} \int_0^{2\pi/c} |\psi_{n\mathbf{k}}\rangle e^{-ilk_\perp c} dk_\perp, \qquad (45)$$

where $\mathbf{k}_\parallel$ is the wave vector in the plane (delocalized directions) and $k_\perp$, l, and c are the wave vector, cell index, and cell dimension in the direction of localization. The 1D Wannier construction can be done independently for each $\mathbf{k}_\parallel$ using direct (i.e., noniterative) methods as described in Sec. IV.C.1 of Marzari and Vanderbilt (1997).

Such a construction proved useful for a variety of purposes, from verifying numerically exponential localization in one dimension, to treating electric polarization or applied electric fields along a specific spatial direction (Giustino, Umari, and Pasquarello, 2003; Giustino and Pasquarello, 2005; Stengel and Spaldin, 2006a; Wu *et al.*, 2006; Murray and Vanderbilt, 2009) or for analyzing aspects of topological insulators (Coh and Vanderbilt, 2009; Soluyanov and Vanderbilt, 2011a, 2011b). Examples will be discussed in Secs. V.B.2 and VI.A.4.

I. Entangled bands

The methods described in the previous sections were designed with *isolated* groups of bands in mind, separated from all other bands by finite gaps throughout the entire Brillouin zone. However, in many applications the bands of interest are not isolated. This can happen, for example, when studying electron transport, which is governed by the partially filled bands close to the Fermi level, or when dealing with empty bands, such as the four low-lying antibonding bands of tetrahedral semiconductors, which are attached to higher conduction bands. Another case of interest is when a partially filled manifold is to be downfolded into a basis of WFs, e.g., to construct model Hamiltonians. In all these examples the desired bands lie within a limited energy range but overlap and hybridize with other bands which extend further out in energy. We refer to them as *entangled bands*.

The difficulty in treating entangled bands stems from the fact that it is unclear exactly which states to choose to form J WFs, particularly in those regions of $\mathbf{k}$ space where the bands of interest are hybridized with other unwanted bands. Before a Wannier localization procedure can be applied, some prescription is needed for constructing J states per $\mathbf{k}$ point from a linear combination of the states in this larger manifold. Once a suitable J-dimensional Bloch manifold has been identified at each $\mathbf{k}$, the same procedure described earlier for an isolated

group of bands can be used to generate localized WFs spanning that manifold.

The problem of computing well-localized WFs starting from entangled bands is thus broken down into two distinct steps, subspace selection and gauge selection. As we see, the same guiding principle can be used for both steps, namely, to achieve "smoothness" in $\mathbf{k}$ space. In the subspace selection step a J-dimensional Bloch manifold which varies smoothly as a function of $\mathbf{k}$ is constructed. In the gauge-selection step that subspace is represented using a set of J Bloch functions which are themselves smooth functions of $\mathbf{k}$, such that the corresponding WFs are well localized.

1. Subspace selection via projection

The projection technique discussed in Sec. II.B can be easily adapted to produce J smoothly varying Bloch-like states starting from a *larger* set of Bloch bands (Souza, Marzari, and Vanderbilt, 2001). The latter can be chosen, for example, as the bands lying within a given energy window, or within a specified range of band indices. Their number $\mathcal{J}_{\mathbf{k}} \geq J$ is not required to be constant throughout the BZ.

We start from a set of J localized trial orbitals $g_n(\mathbf{r})$ and project each of them onto the space spanned by the chosen eigenstates at each $\mathbf{k}$,

$$|\phi_{n\mathbf{k}}\rangle = \sum_{m=1}^{\mathcal{J}_{\mathbf{k}}} |\psi_{m\mathbf{k}}\rangle\langle\psi_{m\mathbf{k}}|g_n\rangle. \qquad (46)$$

This is identical to Eq. (16), except for the fact that the overlap matrix $(A_{\mathbf{k}})_{mn} = \langle\psi_{m\mathbf{k}}|g_n\rangle$ has become rectangular with dimensions $\mathcal{J}_{\mathbf{k}} \times J$. We then orthonormalize the resulting J orbitals using Eq. (17), to produce a set of J smoothly varying Bloch-like states across the BZ,

$$|\tilde{\psi}_{n\mathbf{k}}\rangle = \sum_{m=1}^{J} |\phi_{m\mathbf{k}}\rangle (S_{\mathbf{k}}^{-1/2})_{mn}. \qquad (47)$$

As in Eq. (17), $(S_{\mathbf{k}})_{mn} = \langle\phi_{m\mathbf{k}}|\phi_{n\mathbf{k}}\rangle_V = (A_{\mathbf{k}}^\dagger A_{\mathbf{k}})_{mn}$, but with rectangular $A_{\mathbf{k}}$ matrices.

The above procedure simultaneously achieves the two goals of subspace selection and gauge selection, although neither of them is performed optimally. The gauge selection can be further refined by minimizing $\tilde{\Omega}$ within the projected subspace. It is also possible to refine iteratively the subspace selection itself, as will be described in Sec. II.I.2. However, for many applications this one-shot procedure is perfectly adequate, and in some cases it may even be preferable to more sophisticated iterative approaches (see also Sec. III.C). For example, it often results in "symmetry-adapted" WFs which inherit the symmetry properties of the trial orbitals (Ku *et al.*, 2002).

As an example, we plot in Fig. 5 the eight disentangled bands obtained by projecting the band structure of silicon, taken within an energy window that coincides with the entire energy axis shown, onto eight atomic-like sp^3 hybrids. The disentangled bands, generated using Wannier interpolation (see Sec. VI.A), are shown as triangles, along with the original first-principle bands (solid lines). While the overall agreement is quite good, significant deviations can be seen
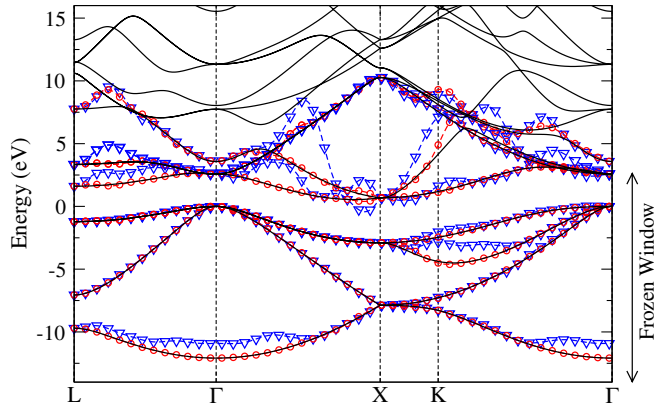
FIG. 5 (color online). Band structure of bulk crystalline Si. Solid lines: Original bands generated directly from a DFT calculation. Triangles: Wannier-interpolated bands obtained from the subspace selected by an unconstrained projection onto atomic sp^3 orbitals. Circles: Wannier-interpolated bands obtained with the same procedure and the additional constraint of reproducing exactly the original valence manifold and parts of the conduction manifold, using a frozen energy window (see text).

wherever higher unoccupied and unwanted states possessing some significant sp^3 character are admixed into the projected manifold. This behavior can be avoided by forcing certain Bloch states to be preserved identically in the projected manifold; we refer to those as belonging to a frozen "inner" window, since this is often the simplest procedure for selecting them. The placement and range of this frozen window will depend on the problem at hand. For example, in order to describe the low-energy physics for, e.g., transport calculations, the frozen window would typically include all states in a desired range around the Fermi level.

We show as circles in Fig. 5 the results obtained by forcing the entire valence manifold to be preserved, leading to a set of eight projected bands that reproduce exactly the four valence bands, and follow quite closely the four low-lying conduction bands. For the modifications to the projection algorithm required to enforce a frozen window, we refer to Sec. III.G of Souza, Marzari, and Vanderbilt (2001).

Projection techniques can work very well, and an application of this approach to graphene is shown in Fig. 6, where the $\pi/\pi^\star$ manifold is disentangled with great accuracy by a simple projection onto atomic p_z orbitals, or the entire occupied manifold together with the $\pi/\pi^\star$ manifold is obtained by projection onto atomic p_z and sp^2 orbitals (one every other atom, for the case of the sp^2 orbitals, although bond-centered s orbitals would work equally well).

Projection methods have been extensively used to study strongly correlated systems (Ku *et al.*, 2002; Anisimov *et al.*, 2005), in particular, to identify a "correlated subspace" for LDA + U or dynamical mean-field theory (DMFT) calculations, as will be discussed in more detail in Sec. VII. It has also been argued (Ku, Berlijn, and Lee, 2010) that projected WFs provide a more appropriate basis for the study of defects, as the pursuit of better localization in a MLWF scheme risks defining the gauge differently for the defect WF as compared to the bulk. Instead, a straightforward projection approach ensures the similarity between the WF
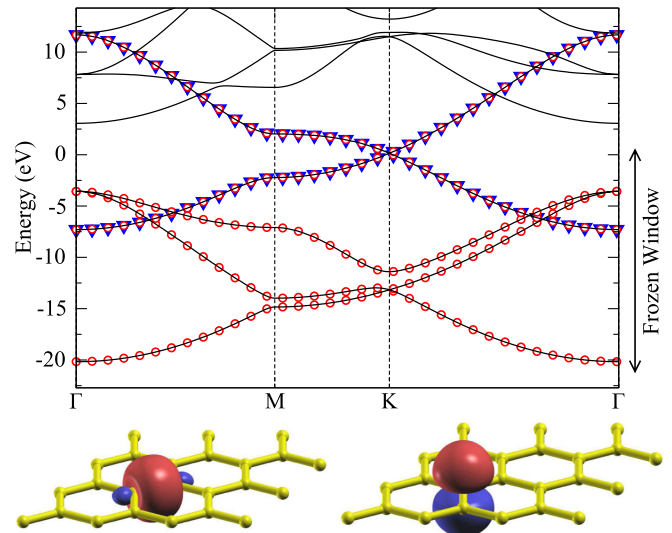

FIG. 6 (color online). Band structure of graphene. Solid lines: Original bands generated directly from a DFT calculation. Triangles: Wannier-interpolated bands obtained from the subspace selected by an unconstrained projection onto atomic p_z orbitals. Circles: Wannier-interpolated bands obtained from the subspace selected by projecting onto atomic p_z orbitals on each atom and sp^2 orbitals on every other atom, and using a frozen energy window. The lower panels shows the MLWFs obtained from the standard localization procedure applied to the first or second projected manifolds (a p_z-like MLWF, or a p_z-like MLWF and a bond MLWF, respectively).

in the defect (supercell) and in the pristine (primitive cell) calculations, and this has been exploited to develop a scheme to unfold the band structure of disordered supercells into the Brillouin zone of the underlying primitive cell, allowing a direct comparison with angle-resolved photoemission spectroscopy (ARPES) experiments (Ku, Berlijn, and Lee, 2010).

2. Subspace selection via optimal smoothness

The projection onto trial orbitals provides a simple and effective way of extracting a smooth Bloch subspace starting from a larger set of entangled bands. The reason for its success is easily understood: the localization of the trial orbitals in real space leads to smoothness in $\mathbf{k}$ space. In order to further refine the subspace selection procedure, it is useful to introduce a precise measure of the smoothness in $\mathbf{k}$ space of a manifold of Bloch states. The search for an optimally smooth subspace can then be formulated as a minimization problem, similar to the search for an optimally smooth gauge.

As it turns out, smoothness in $\mathbf{k}$ of a Bloch space is precisely what is measured by the functional Ω_I introduced in Sec. II.C.1. We know from Eq. (19) that the quadratic spread Ω of the WFs spanning a Bloch space of dimension J comprises two positive-definite contributions, one gauge invariant (Ω_I), and the other gauge dependent ($\tilde{\Omega}$). Given such a Bloch space (e.g., an isolated group of bands, or a group of bands previously disentangled via projection), we have seen that the optimally smooth gauge can be found by minimizing $\tilde{\Omega}$ with respect to the unitary mixing of states within that space.

From this perspective, the gauge invariance of Ω_I means that this quantity is insensitive to the smoothness of the individual Bloch states $|\tilde{u}_{n\mathbf{k}}\rangle$ chosen to represent the Hilbert space. But considering that Ω_I is a part of the spread functional, it must describe smoothness in some other sense. What Ω_I manages to capture is the *intrinsic* smoothness of the underlying Hilbert space. This can be seen starting from the discretized $\mathbf{k}$-space expression for Ω_I, Eq. (30), and noting that it can be written as

$$\Omega_I = \frac{1}{N}\sum_{\mathbf{k,b}} w_b T_{\mathbf{k,b}} \tag{48}$$

with

$$T_{\mathbf{k,b}} = \mathrm{Tr}[P_{\mathbf{k}}Q_{\mathbf{k+b}}], \tag{49}$$

where $P_{\mathbf{k}} = \sum_{n=1}^{J}|\tilde{u}_{n\mathbf{k}}\rangle\langle\tilde{u}_{n\mathbf{k}}|$ is the gauge-invariant projector onto the Bloch subspace at $\mathbf{k}$, $Q_{\mathbf{k}} = \mathbf{1} - P_{\mathbf{k}}$, and "Tr" denotes the electronic trace over the full Hilbert space. It is now evident that $T_{\mathbf{k,b}}$ measures the degree of mismatch (or "spillage") between the neighboring Bloch subspaces at $\mathbf{k}$ and $\mathbf{k+b}$, vanishing when they are identical, and that Ω_I provides a BZ average of the local subspace mismatch.

The optimized subspace selection procedure can now be formulated as follows (Souza, Marzari, and Vanderbilt, 2001). A set of $\mathcal{J}_{\mathbf{k}} \geq J$ Bloch states is identified at each point on a uniform BZ grid, using, for example, a range of energies or bands. We refer to this range, which in general can be k dependent, as the "disentanglement window." An iterative procedure is then used to extract self-consistently at each $\mathbf{k}$ -point the J-dimensional subspace that, when integrated across the BZ, will give the smallest possible value of Ω_I. Viewed as a function of $\mathbf{k}$, the Bloch subspace obtained at the end of this iterative minimization is "optimally smooth" in that it changes as little as possible with $\mathbf{k}$. Typically the minimization starts from an initial guess for the target subspace given, e.g., by projection onto trial orbitals. The algorithm is also easily modified to preserve identically a chosen subset of the Bloch eigenstates inside the disentanglement window, e.g., those spanning a narrower range of energies or bands; we refer to these as comprising a "frozen energy window."

As in the case of the one-shot projection, the outcome of this iterative procedure is a set of J Bloch-like states at each $\mathbf{k}$ which are linear combinations of the initial $\mathcal{J}_{\mathbf{k}}$ eigenstates. One important difference is that the resulting states are not guaranteed to be individually smooth, and the minimization of Ω_I must therefore be followed by a gauge-selection step, which is in every way identical to the one described earlier for isolated groups of bands. Alternatively, it is possible to combine the two steps, and minimize $\Omega = \Omega_I + \tilde{\Omega}$ simultaneously with respect to the choice of Hilbert subspace and the choice of gauge (Thygesen, Hansen, and Jacobsen, 2005a, 2005b); this should lead to the most-localized set of J WFs that can be constructed from the initial $\mathcal{J}_{\mathbf{k}}$ Bloch states. In all three cases, the entire process amounts to a linear transformation taking from $\mathcal{J}_{\mathbf{k}}$ initial eigenstates to J smooth Bloch-like states,
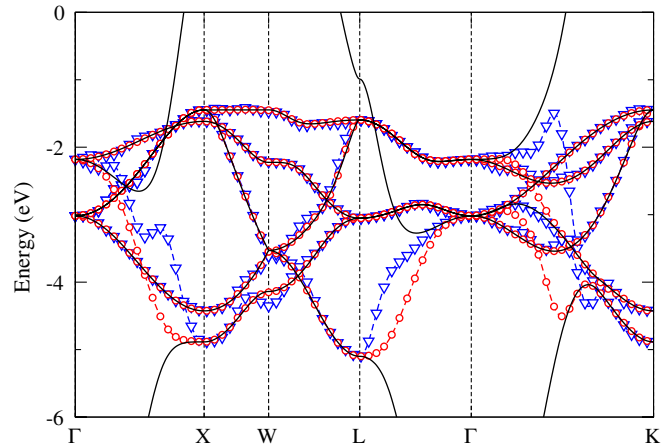

FIG. 7 (color online). (Energy bands of fcc Cu around the d manifold. Solid lines: Original bands generated directly from a DFT calculation. Triangles: Wannier-interpolated bands obtained from the subspace selected by projection onto atomic $3d$ orbitals. Circles: Wannier-interpolated bands obtained from a subspace derived from the previous one, after the criterion of optimal smoothness has been applied. The zero of energy is the Fermi level.

$$|\tilde{\psi}_{n\mathbf{k}}\rangle = \sum_{m=1}^{\mathcal{J}_{\mathbf{k}}}|\psi_{m\mathbf{k}}\rangle V_{\mathbf{k},mn}. \tag{50}$$

In the case of the projection procedure, the explicit expression for the $\mathcal{J}_{\mathbf{k}} \times J$ matrix $V_{\mathbf{k}}$ can be surmised from Eqs. (46) and (47).

We now compare the one-shot projection and iterative procedures for subspace selection, using crystalline copper as an example. Suppose we want to disentangle the five narrow d bands from the wide s band that crosses and hybridizes with them, to construct a set of well-localized d-like WFs. The bands that result from projecting onto five d-type atomic orbitals (AOs) are shown as triangles in Fig. 7. They follow very closely the first-principle bands away from the s-d hybridization regions, where the interpolated bands remain narrow.

The circles show the results obtained using the iterative scheme to extract an optimally smooth five-dimensional manifold. The maximal "global smoothness of connection" is achieved by keeping the five d-like states and excluding the s-like state. This happens because the smoothness criterion embodied by Eqs. (48) and (49) implies that the orbital character is preserved as much as possible while traversing the BZ. Inspection of the resulting MLWFs confirms their atomic d-like character. They are also significantly more localized than the ones obtained by projection and the corresponding disentangled bands are somewhat better behaved, displaying less spurious oscillations in the hybridization regions.

In addition, there are cases where the flexibility of the minimization algorithm leads to surprising optimal states whose symmetries would not have been self-evident in advance. One case is shown in Fig. 8. Here we want to construct a minimal Wannier basis for copper, describing both the narrow d-like bands and the wide free-electron-like band with which they hybridize. By choosing different dimensions
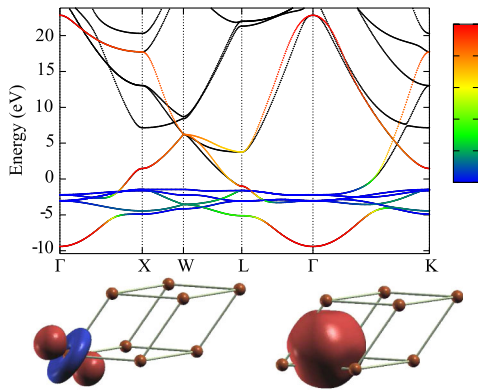
FIG. 8 (color online). Energy bands of fcc Cu over a wide energy range. Solid lines: Original bands generated directly from a DFT calculation. Lines: Wannier-interpolated bands obtained using a disentanglement window corresponding to the entire band manifold shown, and a target dimensionality of seven. This gives rise to five atom-centered d-like MLWFs and two s-like MLWFs located in the tetrahedral interstitial sites, as shown in the lower panel. The color coding of the disentangled bands reflects their projection onto the seven MLWFs, smoothly varying from light s-like interstitial MLWFs to dark atom-centered d-like MLWFs. The zero of energy is the Fermi level.

for the disentangled subspace, it was found that the composite set of bands is faithfully represented by seven MLWFs, of which five are the standard d-like orbitals, and the remaining two are s-like orbitals centered at the tetrahedral interstitial sites of the fcc structure. The latter arise from the constructive interference between sp^3 orbitals that would be part of the ideal sp^3d^5 basis set; in this case, bands up to 20 eV above the Fermi energy can be meaningfully described with a minimal basis set of seven orbitals that would have been difficult to identify using only educated guesses for the projections.

The concept of a natural dimension for the disentangled manifold was explored further by Thygesen, Hansen, and Jacobsen (2005a, 2005b). As illustrated in Fig. 9, they showed that by minimizing $\Omega = \Omega_I + \tilde{\Omega}$ for different choices of J, one can find an optimal J such that the resulting "partially occupied" Wannier functions are most localized
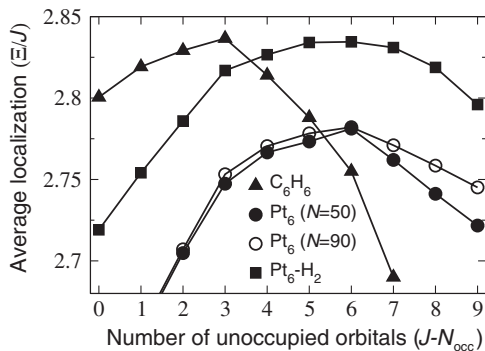

FIG. 9. Average localization [Ξ per Wannier function, with Ξ as defined in Eq. (44)] vs size of the Wannier space for several molecules; larger values indicate greater localization. N_{occ} is the number of occupied states, J is the size of the Wannier space, and N is the total number of states included in the DFT calculation. Adapted from Thygesen, Hansen, and Jacobsen, 2005a.

(provided enough bands are used to capture the bonding and antibonding combinations of those atomic-like WFs).

3. Iterative minimization of Ω_I

The minimization of Ω_I inside an energy window is conveniently done using an algebraic algorithm (Souza, Marzari, and Vanderbilt, 2001). The stationarity condition $\delta\Omega_I(\{\tilde{u}_{n\mathbf{k}}\}) = 0$, subject to orthonormality constraints, is equivalent to solving the set of eigenvalue equations

$$\left[\sum_{\mathbf{b}} w_b P_{\mathbf{k}+\mathbf{b}}\right]|\tilde{u}_{n\mathbf{k}}\rangle = \lambda_{n\mathbf{k}}|\tilde{u}_{n\mathbf{k}}\rangle. \qquad (51)$$

Clearly these equations, one for each $\mathbf{k}$ point, are coupled, so that the problem has to be solved self-consistently throughout the Brillouin zone. This can be done using an iterative procedure: on the ith iteration go through all the $\mathbf{k}$ points in the grid, and for each of them find J orthonormal states $|\tilde{u}_{n\mathbf{k}}^{(i)}\rangle$, defining a subspace whose spillage over the neighboring subspaces from the previous iteration is as small as possible. At each step the set of equations

$$\left[\sum_{\mathbf{b}} w_b P_{\mathbf{k}+\mathbf{b}}^{(i-1)}\right]|\tilde{u}_{n\mathbf{k}}^{(i)}\rangle = \lambda_{n\mathbf{k}}^{(i)}|\tilde{u}_{n\mathbf{k}}^{(i)}\rangle \qquad (52)$$

is solved, and the J eigenvectors with largest eigenvalues are selected. That choice ensures that at self-consistency the stationary point corresponds to the absolute minimum of Ω_I.

In practice Eq. (52) is solved in the basis of the original $\mathcal{J}_{\mathbf{k}}$ Bloch eigenstates $|u_{n\mathbf{k}}\rangle$ inside the energy window. Each iteration then amounts to diagonalizing the following $\mathcal{J}_{\mathbf{k}} \times \mathcal{J}_{\mathbf{k}}$ Hermitian matrix at every $\mathbf{k}$:

$$Z_{mn}^{(i)}(\mathbf{k}) = \langle u_{m\mathbf{k}}|\sum_{\mathbf{b}} w_b [P_{\mathbf{k}+\mathbf{b}}^{(i-1)}]_{\text{in}}|u_{n\mathbf{k}}\rangle. \qquad (53)$$

Since these are small matrices, each step of the iterative procedure is computationally inexpensive.

As a final comment, we mention that in the case of degeneracies or quasidegeneracies in the spreads of orbitals centered on the same site, the localization algorithm will perform a rather arbitrary mixing of these (as can be the case, e.g., for the d or f electrons of a transition-metal ion, or for its t_{2g} or e_g groups). A solution to this problem is to diagonalize an operator with the desired symmetry in the basis of the Wannier functions that have been obtained [see Posternak *et al.* (2002) for the example of the d orbitals in MnO].

4. Localization and local minima

Empirical evidence and experience suggests that localized Wannier functions can be readily constructed also in the case of an entangled manifold of bands: Even for metals, smooth manifolds can be disentangled and "Wannierized" to give MLWFs. Such disentangled MLWFs, e.g., the p_z MLWFs describing the π/π^* manifold of graphene shown in Fig. 6, are found to be strongly localized. While exponential localization has not been proven, both numerical evidence and the analogy with the isolated composite case suggest this might be the case.

Problems associated with reaching local minima of the spread functional, and with obtaining Wannier functions that are not real valued, are more pronounced in the case of entangled bands. They are usually alleviated by careful reconsideration of the energy windows used, in order to include higher energy states of the appropriate symmetry, and/or by using a better initial guess for the projections. We infer, therefore, that such problems are associated not with the Wannierization part of the procedure, but rather with the initial selection of the smooth subspace from the full manifold of entangled bands.

It is worth noting that the Γ-point formulation (see Sec. II.F.2) appears to be less affected by these problems. In cases where it is not intuitive or obvious what the MLWFs should be, therefore, it can often be a fruitful strategy to use the Γ-point formulation to obtain approximate MLWFs that may then be used to inform the initial guess for a subsequent calculation with a full k-point mesh.

J. Many-body generalizations

The concept of WFs is closely tied to the framework of single-particle Hamiltonians. Only in this case can we define J occupied single-particle Bloch functions at each wave vector $\mathbf{k}$ and treat all J of them on an equal footing, allowing for invariance with respect to unitary mixing among them. Once the two-particle electron-electron interaction is formally included in the Hamiltonian, the many-body wave function cannot be reduced to any simple form allowing for the construction of WFs in the usual sense.

One approach is to consider the reduced one-particle density matrix

$$n(\mathbf{r}, \mathbf{r}') = \int \Psi^*(\mathbf{r}, \mathbf{r}_2, \ldots)\Psi(\mathbf{r}', \mathbf{r}_2, \ldots)d\mathbf{r}_2 d\mathbf{r}_3 \ldots \quad (54)$$

for a many-body insulator. Since $n(\mathbf{r}, \mathbf{r}')$ is periodic in the sense of $n(\mathbf{r} + \mathbf{R}, \mathbf{r}' + \mathbf{R}) = n(\mathbf{r}, \mathbf{r}')$, its eigenvectors, the so-called "natural orbitals," have the form of Bloch functions carrying a label $n, \mathbf{k}$. If the insulator is essentially a correlated version of a band insulator having J bands, then at each $\mathbf{k}$ there will typically be J occupation eigenvalues $\nu_{n\mathbf{k}}$ that are close to unity, as well as some small ones that correspond to the quantum fluctuations into conduction-band states. If one focuses just on the subspace of one-particle states spanned by the J valencelike natural orbitals, one can use them to construct one-particle WFs following the methods described earlier, as suggested by Koch and Goedecker (2001). However, while such an approach may provide useful qualitative information, it cannot provide the basis for any exact theory. For example, the charge density, or expectation value of any other one-particle operator, obtained by tracing over these WFs will not match their exact many-body counterparts.

A somewhat related approach, adopted by Hamann and Vanderbilt (2009), is to construct WFs out of the quasiparticle (QP) states that appear in the GW approximation (Aryasetiawan and Gunnarsson, 1998). Such an approach will be described more fully in Sec. VI.A.3. Here again, this approach may give useful physical and chemical intuition, but the one-electron quasiparticle wave functions do not have the physical interpretation of occupied states, and charge densities and other ground-state properties cannot be computed quantitatively from them.

Finally, a more fundamentally exact framework for a many-body generalization of the WF concept, introduced by Souza, Wilkens, and Martin (2000), is to consider a many-body system with twisted boundary conditions applied to the many-body wave function in a supercell. For example, consider M electrons in a supercell consisting of $M_1 \times M_2 \times M_3$ primitive cells and impose the periodic boundary condition

$$\Psi_{\mathbf{q}}(\ldots, \mathbf{r}_j + \mathbf{R}, \ldots) = e^{i\mathbf{q}\cdot\mathbf{R}}\Psi_{\mathbf{q}}(\ldots, \mathbf{r}_j, \ldots) \quad (55)$$

for $j = 1, \ldots, M$, where $\mathbf{R}$ is a lattice vector of the superlattice. One can then construct a single "many-body WF" in a manner similar to Eq. (3), but with $\mathbf{k} \rightarrow \mathbf{q}$ and $|\psi_{n\mathbf{k}}\rangle \rightarrow |\Psi_q\rangle$ on the right side. The resulting many-body WF is a complex function of $3M$ electron coordinates, and as such it is unwieldy to use in practice. However, it is closely related to Kohn's theory of the insulating state (Kohn, 1964), and in principle it can be used to formulate many-body versions of the theory of electric polarization and related quantities, as mentioned in Sec. V.A.4.

III. RELATION TO OTHER LOCALIZED ORBITALS

A. Alternative localization criteria

As we have seen, WFs are inherently nonunique and, in practice, some strategy is needed to determine the gauge. Two possible approaches were already discussed in Sec. II, namely, projection and maximal localization. The latter approach is conceptually more satisfactory, as it does not depend on a particular choice of trial orbitals. However, it still does not uniquely solve the problem of choosing a gauge, as different localization criteria are possible and there is, *a priori*, no reason to choose one over another.

While MLWFs for extended systems have been generated for the most part by minimizing the sum of quadratic spreads, Eq. (17), a variety of other localization criteria have been used over the years for molecular systems. We briefly survey and compare some of the best known schemes. What they all have in common is that the resulting LMOs $\phi_i(\mathbf{r})$ can be expressed as linear combinations of a set of molecular eigenstates $\psi_i(\mathbf{r})$ (the "canonical" MOs), typically chosen to be the occupied ones,

$$\phi_i(\mathbf{r}) = \sum_{j=1}^{J} U_{ji}\psi_j(\mathbf{r}). \quad (56)$$

The choice of gauge then arises from minimizing or maximizing some appropriate functional of the LMOs with respect to the coefficients U_{ij}, under the constraint that the transformation (56) is unitary, which ensures the orthonormality of the resulting LMOs.

The Foster-Boys (FB) criterion (Boys, 1960, 1966; Foster and Boys, 1960a): This is essentially the same as the Marzari-Vanderbilt criterion of minimizing the sum of the quadratic spreads, except that the sum runs over the orbitals in the molecule, rather than in one crystal cell,

$$\Omega_{\text{FB}} = \sum_{i=1}^{J} [\langle \phi_i | \mathbf{r}^2 | \phi_i \rangle - \langle \phi_i | \mathbf{r} | \phi_i \rangle^2]. \tag{57}$$

Interestingly, this criterion is equivalent to minimizing the "self-extension" of the orbitals (Boys, 1966),

$$\sum_{i=1}^{J} \int d\mathbf{r}_1 d\mathbf{r}_2 |\phi_i(\mathbf{r}_1)|^2 (\mathbf{r}_1 - \mathbf{r}_2)^2 |\phi_i(\mathbf{r}_1)|^2 \tag{58}$$

and also to maximizing the sum of the squares of the distance between the charge centers of the orbitals

$$\sum_{i,j=1}^{J} |\langle \phi_i | \mathbf{r} | \phi_i \rangle - \langle \phi_j | \mathbf{r} | \phi_j \rangle|^2, \tag{59}$$

which is closely related to Eq. (44) of Sec. II.F.2. The relation between Eqs. (57) and (59) is discussed by Boys (1966).

The Edmiston-Ruedenberg (ER) criterion: Here localization is achieved by maximizing the Coulomb self-interaction of the orbitals (Edmiston and Ruedenberg, 1963)

$$\Omega_{\text{ER}} = \sum_{i=1}^{J} \int d\mathbf{r}_1 d\mathbf{r}_2 |\phi_i(\mathbf{r}_1)|^2 (\mathbf{r}_1 - \mathbf{r}_2)^{-1} |\phi_i(\mathbf{r}_2)|^2. \tag{60}$$

From a computational point of view, the ER approach is more demanding (it scales as J^4 versus J^2 for FB), but recently more efficient implementations have been developed (Subotnik, Sodt, and Head-Gordon, 2007).

The von Niessen (VN) criterion: The goal here is to maximize the density overlap of the orbitals (von Niessen, 1972)

$$\Omega_{\text{VN}} = \sum_{i=1}^{J} \int d\mathbf{r}_1 d\mathbf{r}_2 |\phi_i(\mathbf{r}_1)|^2 \delta(\mathbf{r}_1 - \mathbf{r}_2) |\phi_i(\mathbf{r}_2)|^2. \tag{61}$$

The Pipek-Mezey (PM) criterion (Pipek and Mezey, 1989): This approach differs from the ones above in that it makes reference to some extrinsic objects. The idea is to maximize the sum of the squares of the Mulliken atomic charges (Mulliken, 1955). These are obtained with respect to a set of atomic orbitals χ_μ centered on atomic sites A. We define

$$P_A = \sum_{\mu \in A} \sum_{\nu} D_{\mu\nu} S_{\mu\nu}, \tag{62}$$

where the sum over μ involves all of the atomic states on atom site A, $D_{\mu\nu}$ is the density matrix in the atomic basis, and $S_{\mu\nu} = \langle \chi_\mu | \chi_\nu \rangle$ is the overlap operator. The functional to be maximized is given by

$$\Omega_{\text{PM}} = \sum_{i=1}^{J} \sum_{A=1}^{N_A} |\langle \phi_i | P_A | \phi_i \rangle|^2. \tag{63}$$

This is somewhat similar in spirit to the projection scheme discussed in Sec. II.B, except that it is not a one-shot procedure.

As indicated in Eq. (56), all of these schemes amount to unitary transformations among the canonical MOs and, as such, they give rise to representations of the electronic structure of the system that are equivalent to those provided by the original set of eigenstates. For the purpose of providing
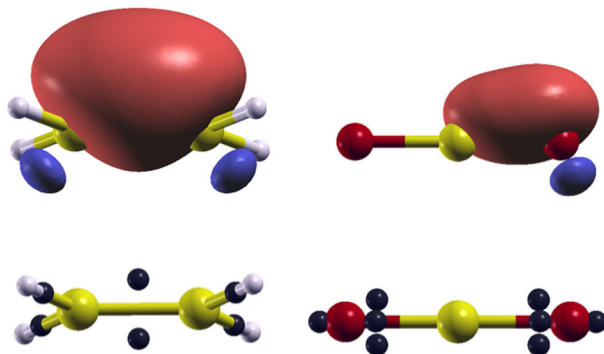

FIG. 10 (color online). Ethane (left panels) and CO_2 (right panels), showing one of the τ-type ("banana") MLWFs (top panels) and a full set of valence Wannier centers (bottom panels). The Wannier centers are shown as small dark spheres. The MLWFs are calculated in a large supercell with Γ-point sampling of the Brillouin zone, as described in Sec. II.F.2, and are equivalent to Foster-Boys orbitals.

chemical intuition, the usefulness of a given scheme depends on how well it matches a particular viewpoint of bonding. There have been few studies of the VN scheme, but the FB, ER, and PM schemes have been extensively compared. In many cases all three approaches lead to similar localized orbitals which agree with the simple Lewis picture of bonding. A notable exception is for systems that exhibit both σ and π bonding. For a double bond, both the FB and ER schemes mix the σ and π orbitals, giving rise to two bent "banana bond" (or τ) orbitals (Pauling, 1960) as shown in Fig. 10. When applied to benzene, both schemes give alternating σ and τ orbitals. Trivially, there are two equivalent sets of these orbitals, reminiscent of the two Kekulé structures for benzene. In contrast to the FB and ER schemes, PM provides a clear separation of σ and π orbitals. For example, in benzene PM gives a framework of six σ orbitals and three π orbitals around the ring.

In some situations the FB and ER orbitals have been found to be quite different. This has been observed when the bonding in a molecule can be represented as two distinct resonant structures. The ER scheme generally gives orbitals corresponding to one of the possible structures, while the FB orbitals correspond to a hybrid of the structures. An extreme example is CO_2 (Brown, Kleier, and Lipscomb, 1977). In agreement with the O = C = O Lewis picture, ER gives two lone pairs on each oxygen and two τ orbitals between each carbon and oxygen. In contrast, the FB scheme gives a single lone pair on each oxygen and three highly polarized τ orbitals between the carbon and each oxygen, as shown in Fig. 10.

MLWFs, which may be thought of as the solid-state equivalent of FB orbitals, have been widely used to examine chemical bonding, as discussed in detail in Sec. IV. The ER scheme has not been extensively examined, an isolated exception being the work of Miyake and Aryasetiawan (2008) who proposed a method to maximize the Coulomb self-interaction of the orbitals in periodic systems (see also Sec. VII.B.1). They examined a range of bulk transition metals and $SrVO_3$ and in each case found that the resulting WFs were essentially identical to MLWFs.

B. Minimal-basis orbitals

In the same way as was described for the Marzari-Vanderbilt scheme of Sec. II.C, the alternative localization criteria described above can be applied in a solid-state context to isolated groups of bands. One is often interested in the more general situation where the bands of interest are not isolated. The challenge then is to generate a "disentangled" set of J localized WFs starting from some larger set of bands. Two procedures for doing so were discussed in Sec. II.I, namely, projection and iterative minimization of the spread functional Ω, not only with respect to the choice of gauge, but also with respect to the choice of Hilbert space.

Here we discuss two further procedures which achieve the same goal by different means. They have in common the fact that the resulting orbitals constitute a minimal basis of atomic-like orbitals.

1. Quasiatomic orbitals

The quasiatomic orbitals (QOs) scheme (Lu *et al.*, 2004; Chan *et al.*, 2007; Qian *et al.*, 2008) is a projection-based approach that has the aim of extracting a minimal tight-binding basis from an initial first-principles calculation. In this regard it is similar in spirit to the Wannier interpolation techniques discussion in Sec. VI. Unlike WFs, however, the quasiatomic orbitals form a *nonorthogonal* basis of *atom-centered* functions, each with a specified angular character. Their radial part, and hence their detailed local shape, depends on the bonding environment.

As in the Wannier scheme, the first step is to construct a suitable J-dimensional subspace $\{\phi_n\}$ starting from a larger set of $\mathcal{J}$ Bloch eigenstates $\{\psi_n\}$. For simplicity, we consider a Γ-point only sampling of the BZ and hence omit the **k** index. The goal is to identify a disentangled subspace with the desired atomic-orbital character, as specified by a given set of J AOs $|A_i\rangle$, where i is a composite site and angular-character index. One possible strategy would be to employ the one-shot projection approach of Sec. II.I.1, using the AOs as trial orbitals. Lu *et al.* (2004) proposed a more optimized procedure, based on maximizing the similarity measure[8]

$$\mathcal{L} = \sum_{i=1}^{J} \sum_{n=1}^{J} |\langle \phi_n | A_i \rangle|^2 \qquad (64)$$

with respect to the orthonormal set $\{\phi_n\}$, expressed as linear combinations of the original set $\{\psi_n\}$. It is usually required that a subset of $N \leq J$ of the original eigenstates are identically preserved ("frozen in") in the disentangled subspace, in which case the optimization is performed with respect to the remaining $J-N$ states ϕ_n. $\mathcal{J}$ must be of sufficient size to capture all of the antibonding character of the AOs.

In later work it was realized (Qian *et al.*, 2008) that the QOs can be constructed without explicit calculation of the eigenstates outside the frozen window. The key insight is to realize that the QOs will only have a contribution from the finite subset of this basis spanned by the AOs [see Eq. (67)].

---

[8]This is similar in spirit to the Pipek-Mazey procedure, Eq. (62), but applied to subspace selection rather than gauge selection.

The component of the AOs projected onto the N states within the frozen window $|A_i^\parallel\rangle$ is given by

$$|A_i^\parallel\rangle = \sum_{n=1}^{N} |\psi_n\rangle\langle\psi_n|A_i\rangle. \qquad (65)$$

The component of $|A_i\rangle$ projected onto the states outside the frozen window can hence be constructed directly using only the AOs and the states within the frozen window as

$$|A_i^\perp\rangle = |A_i\rangle - |A_i^\parallel\rangle. \qquad (66)$$

Using $|A_i^\perp\rangle$ as a basis, the set of $\{\phi_n\}$ which maximize $\mathcal{L}$ can be obtained using linear algebra as reported by Qian *et al.* (2008).

Once a subspace with the correct orbital character has been identified, a basis of quasiatomic orbitals can be obtained by retaining the portion of the original AOs that "lives" on that subspace,

$$|Q_i\rangle = \sum_{n=1}^{J} |\phi_n\rangle\langle\phi_n|A_i\rangle. \qquad (67)$$

In general the angular dependence of the resulting QOs is no longer that of pure spherical harmonics, but only approximately so. Qian *et al.* (2008) obtained QOs for simple metals and semiconductors. Later applications used the orbitals for the study of quantum transport in nanostructures (Qian, Li, and Yip, 2010).

2. The *N*th-order muffin-tin-orbital (NMTO) approach and downfolding

An alternative scheme for obtaining a minimal-basis representation is the perturbation approach introduced by Löwdin (1951). Here the general strategy is to partition a set of orbitals into an "active" set that is intended to describe the states of interest, and a "passive" set that will be integrated out. We write the Hamiltonian for the system in a block representation,

$$H = \begin{pmatrix} H_{00} & 0 \\ 0 & H_{11} \end{pmatrix} + \begin{pmatrix} 0 & V_{01} \\ V_{10} & 0 \end{pmatrix}, \qquad (68)$$

where H_{00} (H_{11}) is the projection onto the active (passive) subspace, and V_{01} is the coupling between the two subspaces. An eigenfunction can be written as the sum of its projections onto the two subspaces $|\psi\rangle = |\psi_0\rangle + |\psi_1\rangle$. This leads to

$$(H_{00} - \varepsilon)|\psi_0\rangle + V_{01}|\psi_1\rangle = 0, \qquad (69)$$

$$V_{10}|\psi_0\rangle + (H_{11} - \varepsilon)|\psi_1\rangle = 0, \qquad (70)$$

where ε is the eigenvalue corresponding to $|\psi\rangle$. Elimination of $|\psi_1\rangle$ gives an effective Hamiltonian for the system which acts only on the active subspace:

$$H_{00}^{\text{eff}}(\varepsilon) = H_{00} - V_{01}(H_{11} - \varepsilon)^{-1}V_{10}. \qquad (71)$$

This apparent simplification introduced an energy dependence into the Hamiltonian. One practical way forward is to approximate this as an energy-independent Hamiltonian $H_{00}^{\text{eff}}(\varepsilon_0)$, choosing the reference energy ε_0 to be the average energy of the states of interest. This approach has been used

Carbon *s*-orbital
isosurface = +/- 0.04

Carbon p_x-orbital
isosurface = +/- 0.04

Carbon p_y-orbital
isosurface = +/- 0.04

Graphite σ bonding-bands

Carbon *sp2*-bond orbital
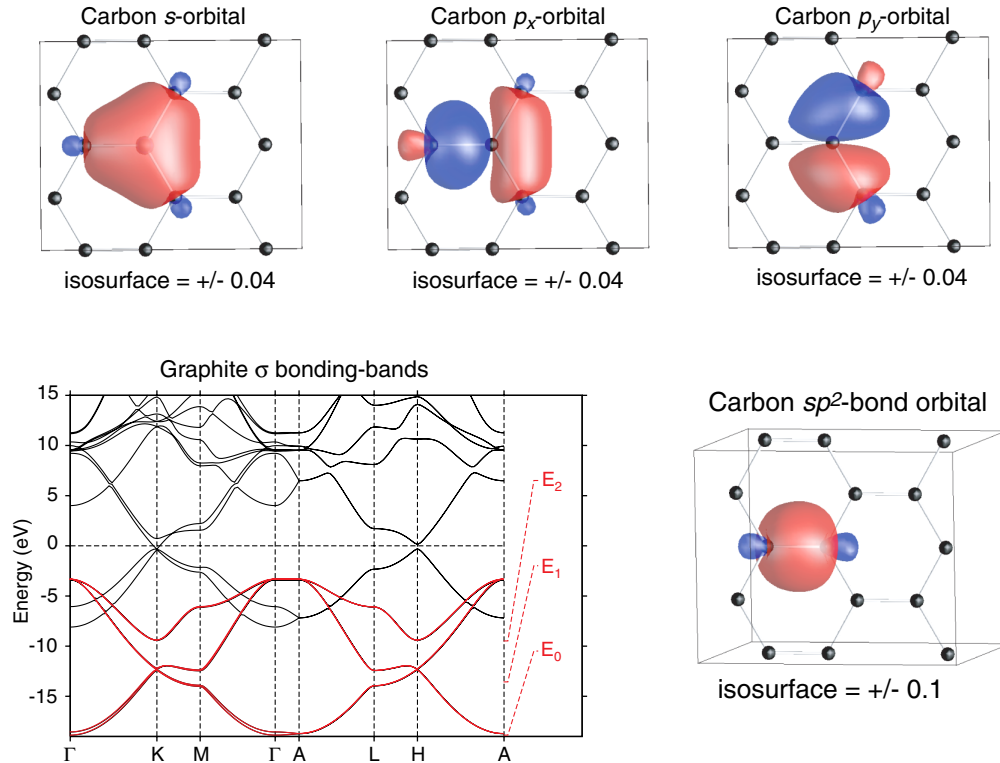isosurface = +/- 0.1

FIG. 11 (color online). Bottom left panel: The band structure of graphite as calculated with a full *N*th-order muffin-tin orbital (NMTO) *s*, *p*, *d* basis, or with an *s*, p_x, and p_y orbital on every second carbon atom (lighter bands). Bottom right panel: One of the sp^2 bond orbitals which arise by symmetrical orthonormalization of the *s*, p_x, and p_y orbitals (top panels). The energy meshes used for each calculation are given to the right of the band structure. From Zurek, Jepsen, and Andersen, 2005.

to construct tight-binding Hamiltonians from full electronic-structure calculations (Solovyev, 2004).

A form of Löwdin partitioning has been widely used in connection with the linear-muffin-tin-orbital (LMTO) method, particularly in its most recent formulation, the *N*th-order muffin-tin-orbital (NMTO) approach (Andersen and Saha-Dasgupta, 2000; Zurek, Jepsen, and Andersen, 2005). In this context it is usually referred to as downfolding, although we note that some use this term to refer to any scheme to produce a minimal basis-set representation.

In studies of complex materials there may be a significant number of MTOs, typically one for each angular-momentum state (*s*, *p*, *d*) on every atomic site. One may wish to construct a minimal basis to describe states within a particular energy region, e.g., the occupied states, or those crossing the Fermi level. Assume we have basis orbitals (MTOs in this case) which we wish to partition into active and passive sets. Using the notation of Eq. (68), Löwdin partitioning gives a set of energy-dependent orbitals $\phi_0(\varepsilon, \mathbf{r})$ for the active space according to (Zurek, Jepsen, and Andersen, 2005)

$$\phi_0(\varepsilon, \mathbf{r}) = \phi_0(\mathbf{r}) - \phi_1(\mathbf{r})(H_{11} - \varepsilon)^{-1}V_{10}. \qquad (72)$$

Taking into account the energy dependence, this reduced set of orbitals spans the same space as the original full set of orbitals and can be seen to be the original orbitals of the active set dressed by an energy-dependent linear combination of orbitals from the passive set. In the NMTO scheme, the next step is to form an energy-independent set

of orbitals through an *n*th-order polynomial fit to the energy dependence.

To give a specific example, accurate calculations on tetrahedral semiconductors will require the inclusion of *d* states in the MTO basis, i.e., nine states (*s*, *p*, *d*) per site. However, it would be desirable to construct a minimal basis to describe the valence and lower conduction states with only four states (*s*, *p*) on each site (Lambrecht and Andersen, 1986). We therefore designate *s* and *p* as active channels and *d* as passive. Downfolding will result in an MTO with either *s* or *p* character on a given site, with the inclusion of *d* character on neighboring sites. In other words, the tail of the MTO is modified to "fold in" the character of the passive orbitals.

In Fig. 11, the band structure of graphite calculated using a full *s*, *p*, and *d* basis on each carbon atom is shown (Zurek, Jepsen, and Andersen, 2005), and compared to the bands obtained by choosing *s*, p_x, and p_y states on every second carbon atom as the active channels and downfolding all other states. The energy mesh spans the energy range of the sp^2 bonding states (shown on the right-hand side of the band-structure plot in Fig. 11). For these bands the agreement with the full calculation is perfect to within the resolution of the figure. Symmetric orthonormalization of the three NMTOs gives the familiar set of three symmetry related σ-bonding orbitals (compare with the MLWF of graphene in Fig. 6). Lechermann *et al.* (2006) compared MLWFs and NMTO orbitals for a set of t_{2g} states located around the Fermi level SrVO₃. It was found that both schemes gave essentially identical orbitals.

C. Comparative discussion

At this point it is worth commenting briefly on some of the advantages and disadvantages of various choices of WFs. We emphasize again that no choice of WFs, whether according to maximal localization or other criteria, can be regarded as "more correct" than another. Because WFs are intrinsically gauge dependent, it is impossible, even in principle, to determine the WFs experimentally. By the same token, certain properties obtained from the WFs, such as the dipole moments of molecules in condensed phases (see Sec. V.B.3), must be interpreted with caution. The measure of a WF construction procedure is, instead, its *usefulness* in connection with theoretical or computational manipulations.

Whether or not the WFs are to be used as basis functions for Wannier interpolation (see Sec. VI) or other purposes (see Sec. VII), some variety of maximally localized WFs are probably most natural both because the real-space matrix elements can be restricted to relatively near neighbors, and because Fourier-transformed quantities become relatively smooth in **k** space. However, in cases in which the set of MLWFs does not preserve the space-group symmetry, it may be better to insist on symmetry-preserving WFs even at the expense of some delocalization (see also the discussion in Sec. II.I.1). In this way, properties computed from the WFs, such as interpolated band structures, will have the correct symmetry properties. When using WFs to interpret the nature of chemical bonds, as in Sec. IV, the results may depend to some degree on the choice of WF construction method, and the optimal choice may in the end be a matter of taste.

D. Nonorthogonal orbitals and linear scaling

In recent years there has been much progress in the development of practical linear-scaling methods for electronic-structure calculations, that is, methods in which the computational cost of the calculation grows only linearly with the size of the system. The fundamental principle behind such approaches is the fact that electronic structure is inherently local (Heine, 1980), or "nearsighted" (Kohn, 1996). This manifests itself in the exponential localization of the WFs in insulators (discussed in Sec. II.G) and, more generally, in the localization properties of the single-particle density matrix

$$\rho(\mathbf{r}, \mathbf{r}') = \langle \mathbf{r} | P | \mathbf{r}' \rangle$$
$$= \frac{V}{(2\pi)^3} \int_{BZ} d\mathbf{k} \sum_n f_{n\mathbf{k}} \psi_{n\mathbf{k}}(\mathbf{r}) \psi_{n\mathbf{k}}^*(\mathbf{r}'), \qquad (73)$$

where, following Janak (1978), the projection operator P of Eq. (5) has been generalized to the case of fractional eigenstate occupancies $f_{n\mathbf{k}}$. The quantity $\rho(\mathbf{r}, \mathbf{r}')$ has been shown to decay exponentially as $\exp(-\gamma|\mathbf{r} - \mathbf{r}'|)$ in insulators and semiconductors, where the exponent γ can be heuristically related to the direct band gap of the system (des Cloizeaux, 1964a; Ismail-Beigi and Arias, 1999; Taraskin, Drabold, and Elliott, 2002). It has also been shown to take the same form in metals at finite temperature,[9] but with γ determined by the

ratio between the thermal energy $k_B T$ and the Fermi velocity (Goedecker, 1998).

Exponential localization may seem a surprising result given that the Bloch eigenstates extend across the entire system. Expressing the density matrix in terms of WFs using Eq. (10), we find

$$\rho(\mathbf{r}, \mathbf{r}') = \sum_{ij} \sum_{\mathbf{R}\mathbf{R}'} w_{i\mathbf{R}}(\mathbf{r}) K_{ij}(\mathbf{R}' - \mathbf{R}) w_{j\mathbf{R}'}^*(\mathbf{r}'), \qquad (74)$$

where we have defined the *density kernel*[10]

$$K_{ij}(\mathbf{R}) = \frac{V}{(2\pi)^3} \int_{BZ} d\mathbf{k} \, e^{-i\mathbf{k}\cdot\mathbf{R}} \sum_n [U^{(\mathbf{k})\dagger}]_{in} f_{n\mathbf{k}} [U^{(\mathbf{k})}]_{nj}, \qquad (75)$$

which reduces to $\delta_{ij}\delta_{\mathbf{R}0}$ in the case of a set of fully occupied bands. We now see that the spatial localization of the density matrix is closely linked to that of the Wannier functions themselves. This locality is exploited in linear-scaling methods by retaining an amount of information in the density matrix that scales only linearly with system size.

Many different linear-scaling DFT approaches exist; for comprehensive reviews, see Galli (1996), Goedecker (1999), and Bowler and Miyazaki (2012). Many of them are based on the variational minimization of an energy functional expressed either in terms of localized Wannier-like orbitals or the density operator itself. The common point between these variational methods is that the idempotency of the density operator or the orthogonality of the Wannier orbitals is not imposed explicitly during the minimization procedure. Instead, the energy functionals are constructed such that these properties are satisfied automatically at the minimum, which coincides with the true ground state of the system.

Many of these methods also make use of nonorthogonal localized orbitals, referred to as "support functions" (Hernández and Gillan, 1995) or "nonorthogonal generalized Wannier functions" (NGWFs) (Skylaris *et al.*, 2002), in contrast to canonical WFs, which are orthogonal. The density matrix in Eq. (74) can be generalized so as to be represented in terms of a set of nonorthogonal localized orbitals $\{\phi_{\alpha\mathbf{R}}(\mathbf{r})\}$ and a corresponding nonunitary (and, in general, nonsquare) transformation matrix $M^{(\mathbf{k})}$, which take the place of $\{w_{i\mathbf{R}}(\mathbf{r})\}$ and $U^{(\mathbf{k})}$, respectively. Two main benefits arise from allowing nonorthogonality. First, it is no longer necessary to enforce explicit orthogonality constraints on the orbitals during the energy minimization procedure (Galli and Parrinello, 1992; Mauri, Galli, and Car, 1993; Ordejón *et al.*, 1993; Hierse and Stechel, 1994; Hernández, Gillan, and Goringe, 1996). Second, a nonorthogonal representation can be more localized than an essentially equivalent orthogonal one (Anderson, 1968; He and Vanderbilt, 2001). In practice, linear-scaling methods target large systems, which means that Γ-point only sampling of the BZ is usually sufficient. In this case, the separable form for the density matrix simplifies to

$$\rho(\mathbf{r}, \mathbf{r}') = \sum_{\alpha\beta} \phi_\alpha(\mathbf{r}) K^{\alpha\beta} \phi_\beta^*(\mathbf{r}'), \qquad (76)$$

---

[9]For metals at zero temperature, the discontinuity in occupancies as a function of **k** results in the well-known *algebraic* decay of the density matrix.

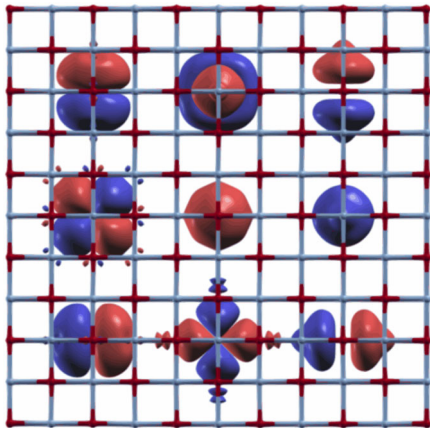[10]This term was, to our knowledge, first used by McWeeny (1960).

FIG. 12 (color online). Isosurfaces of the set of nine nonorthogonal generalized Wannier functions (NGWFs) on a nickel atom in NiO (shown centered on different, symmetrically equivalent, Ni atoms in the lattice). The isosurface is set to half of the maximum for the s and p-like NGWFs and 10^{-3} times the maximum for the d-like NGWFs. Adapted from O'Regan, Payne, and Mostofi, 2011.

where the density kernel is[11]

$$K^{\alpha\beta} = \sum_n [M^\dagger]_n^\alpha f_n [M]_n^\beta. \tag{77}$$

Minimization of an appropriate energy functional with respect to the degrees of freedom present in the density matrix leads to ground-state nonorthogonal orbitals that are very similar in appearance to (orthogonal) MLWFs. Figure 12 shows, for example, NGWFs on a Ni atom in bulk NiO, obtained using the ONETEP linear-scaling DFT code (Skylaris *et al.*, 2005). A recent comparison of static polarizabilities for molecules, calculated using Eq. (89) with both MLWFs and NGWFs, demonstrates remarkable agreement between the two (O'Regan, Payne, and Mostofi, 2012).

E. Other local representations

Over the years, a number of other computational schemes have been devised to provide a local analysis of the electronic structure in molecules and solids. Here we briefly mention those most commonly used in solid-state studies. The first choice is whether to work with the electronic wave function or with the charge density.

One of the earliest and still most widely used wave function based schemes is the "Mulliken population analysis" (Mulliken, 1955). This starts from a representation of the density operator in a linear combination of atomic orbitals (LCAO) basis. If an extended basis, such as plane waves, has been used, this can be obtained after first performing a projection onto a suitable set of atomic orbitals (Sánchez-Portal, Artacho, and Soler, 1995). Using the quantity P_A introduced in Eq. (62) the Mulliken charge on an atomic site A is given by

---

[11]It is worth noting that the nonorthogonality of the orbitals results in an important distinction between covariant and contravariant quantities, as denoted by raised and lowered Greek indices (Artacho and Miláns del Bosch, 1991; O'Regan, Payne, and Mostofi, 2011).

$$Q_A = \sum_{i=1}^J \langle \phi_i | P_A | \phi_i \rangle. \tag{78}$$

The Mulliken scheme also provides a projection into local angular-momentum eigenstates and an overlap (or bond) population between atom pairs. The major disadvantage of the scheme is the fact that the absolute values obtained have a marked dependence on the LCAO basis. In fact, the results tend to become less meaningful as the basis is expanded, as orbitals on one atomic site contribute to the wave function on neighboring atoms. However, it is generally accepted that so long as calculations using the same set of local orbitals are compared, trends in the values can provide some chemical intuition (Segall *et al.*, 1996). An early application was to the study of bonding at grain boundaries of TiO_2 (Dawson *et al.*, 1996).

An alternative approach is to work directly with the charge density. The scheme of Hirshfeld (1977) attempted to partition the charge density by first defining a so-called prodensity for the system, typically a superposition of free-atom charge densities $\rho^i(\mathbf{r})$. The ground-state charge density is then partitioned between atoms according to the proportions of the procharge at each point in space. This can easily be integrated to give, for example, a total charge

$$Q_H^i = \int \mathbf{dr} \rho(\mathbf{r}) \frac{\rho^i(\mathbf{r})}{\Sigma_i \rho^i(\mathbf{r})} \tag{79}$$

for each atomic site. Hirschfield charges have recently been used to parametrize dispersion corrections to local-density functionals (Tkatchenko and Scheffler, 2009).

Partitioning schemes generally make reference to some arbitrary auxiliary system; in the case of Hirschfield charges, this is the free-atom charge density, which must be obtained within some approximation. In contrast, the atoms in molecules (AIM) approach developed by Bader (1991) provides a uniquely defined way to partition the charge density. It uses the vector field corresponding to the gradient of the charge density. In many cases the only maxima in the charge density occur at the atomic sites. As all field lines must terminate on one of these atomic "attractors," each point in space can be assigned to a particular atom according to the basin of attraction that is reached by following the density gradient. Atomic regions are now separated by zero-flux surfaces $S(\mathbf{r}_s)$ defined by the set of points $(\mathbf{r}_s)$ at which

$$\nabla \rho(\mathbf{r}_s) \cdot \mathbf{n}(\mathbf{r}_s) = 0, \tag{80}$$

where $\mathbf{n}(\mathbf{r}_s)$ is the unit normal to $S(\mathbf{r}_s)$. Having made such a division it is straightforward to obtain values for the atomic charges (and also dipoles, quadrupoles, and higher moments). The AIM scheme has been widely used to analyze bonding in both molecular and solid-state systems, as well as to give a localized description of response properties such as infrared absorption intensities (Matta, Boyd, and Becke, 2007).

A rather different scheme is the electron localization function (ELF) introduced by Becke and Edgecombe (1990) as a simple measure of electron localization in physical systems. Their original definition is based on the same-spin pair probability density $P(\mathbf{r}, \mathbf{r}')$, i.e., the probability to find two like-spin electrons at positions $\mathbf{r}$ and $\mathbf{r}'$. Savin *et al.* (1992) introduced a form for the ELF $\epsilon(\mathbf{r})$ which can be applied to an independent-particle model:
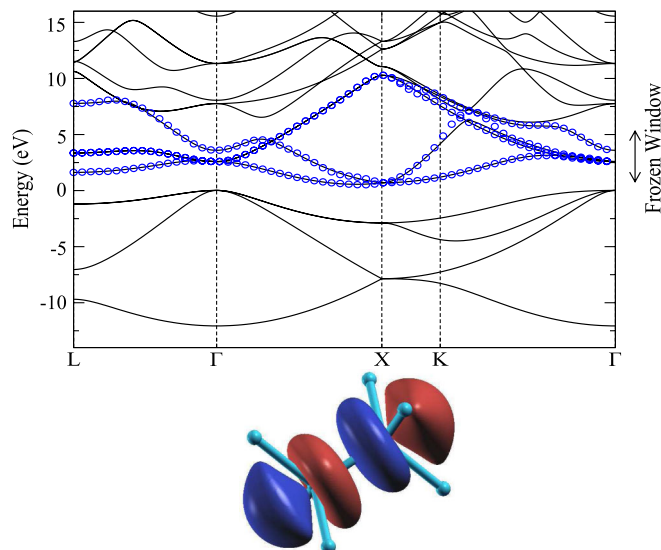
FIG. 13 (color online). Band structure of crystalline Si and corresponding conduction MLWFs. Top: Circles indicate a four-dimensional manifold which has been disentangled from the full band structure (solid lines). The frozen window is also indicated. Bottom: One of the four antibonding MLWFs obtained from this manifold (the other three are equivalent under space-group symmetry operations).

$$\epsilon(\mathbf{r}) = \frac{1}{1 + (D/D_h)^2}, \tag{81}$$

$$D = \frac{1}{2} \sum_{i=1}^{J} |\nabla \psi_i|^2 - \frac{1}{8} \frac{|\nabla \rho|^2}{\rho}, \tag{82}$$

$$D_h = \frac{3}{10} (3\pi^2)^{2/3} \rho^{5/3}, \qquad \rho = \sum_{i=1}^{J} |\psi_i|^2, \tag{83}$$

where the sum is over all occupied orbitals. D represents the difference between the noninteracting kinetic energy and the kinetic energy of an ideal Bose gas. D_h is the kinetic energy of a homogeneous electron gas with a density equal to the local density. As defined, $\epsilon(\mathbf{r})$ is a scalar function which ranges from 0 to 1. Regions of large kinetic energy (i.e., electron delocalization) have ELF values close to zero while larger values correspond to paired electrons in a shared covalent bond or in a lone pair. In a uniform electron gas of any density, $\epsilon(\mathbf{r})$ will take the value of $\frac{1}{2}$. Early application of the ELF in condensed phases provided insight into the nature of the bonding at surfaces of Al (Santis and Resta, 2000) and Al_2O_3 (Jarvis and Carter, 2001), and a large number of other applications have appeared since.

IV. ANALYSIS OF CHEMICAL BONDING

As discussed in Sec. III.A, there is a long tradition in the chemistry literature of using localized molecular orbitals (Boys, 1960, 1966; Foster and Boys, 1960a, 1960b; Edmiston and Ruedenberg, 1963) as an appealing and intuitive avenue for investigating the nature of chemical bonding in molecular systems. MLWFs provide the natural generalization of this concept to the case of extended or solid-state systems. Since MLWFs are uniquely defined for the case of insulators and semiconductors, they are particularly suited to discuss hybridization, covalency, and ionicity in both crystalline and disordered systems. In addition, in the supercell approximation they can be used to describe any disordered bulk, amorphous, or liquid system (Payne *et al.*, 1992), providing a compact description of electronic states in terms of their Wannier centers, their coordination with other atoms, and the spatial distribution and symmetry of the MLWFs. As such, they are often very useful for extracting chemical trends and for allowing for statistics to be gathered on the nature of bonds (e.g., covalent bonds versus lone pairs), be it in the presence of structural complexity, as is the case of an amorphous solid, or following the intrinsic dynamics of a liquid or an unfolding chemical reaction. They also share the same strengths and weaknesses alluded to in Sec. III.A, whereby different localization criteria can provide qualitatively different representations of chemical bonds. This arbitrariness seems less common in an extended system, and often some of the most chemically meaningful information comes from the statistics of bonds as obtained in large-scale simulations, or in long first-principles molecular-dynamics runs. Finally, localized orbitals can embody the chemical concept of transferable functional groups, and thus be used to construct a good approximation for the electronic structure of complex systems starting from the orbitals for the different fragments (Hierse and Stechel, 1994; Benoit, Sebastiani, and Parrinello, 2001; Lee, Nardelli, and Marzari, 2005), as discussed in Sec. VII.

A. Crystalline solids

One of the most notable, albeit qualitative, characteristics of MLWFs is their ability to highlight the chemical signatures of different band manifolds. This was realized early on, as is apparent from Fig. 2, showing the isosurfaces for one of the four MLWFs in crystalline silicon and gallium arsenide, respectively. These are obtained from the closed manifold of four valence bands, yielding four equivalent MLWFs that map into one another under the space-group symmetry operations of the crystal.[12] It is clearly apparent that these MLWFs represent the intuitive chemical concept of a covalent bond, with each MLWF representing the bonding orbital created by the constructive interference of two atomic sp^3 orbitals centered on neighboring atoms. In addition, it can be seen that in gallium arsenide this covalent bond and its WFC are shifted toward the more electronegative arsenic atom. This was explored further by Abu-Farsakh and Qteish (2007) to introduce a formal definition of electronegativity, or rather of a bond-ionicity scale, based on the deviation of WFCs from their geometrical bond centers. It is worth mentioning that these qualitative features of Wannier functions tend to be robust and often independent of the details of the method used to obtained them, maximally localized or not.

---

[12]It should be noted that the maximal-localization procedure does not necessarily lead to WFs that respect the space-group symmetry. If desired, symmetries can be enforced by imposing codiagonalization of appropriate operators (Posternak *et al.*, 2002) or by using projection methods (Ku *et al.*, 2002; Qian *et al.*, 2008).

For example, similar results are obtained for covalent conductors whether one makes use of symmetry considerations (Satpathy and Pawlowska, 1988; Smirnov and Usvyat, 2001; Smirnov, Evarestov, and Usvyat, 2002; Usvyat, Evarestov, and Smirnov, 2004), finite-support regions in linear-scaling methods (Fernandez *et al.*, 1997; Skylaris *et al.*, 2002), or projection approaches (Stephan, Martin, and Drabold, 2000), or even if the MLWF algorithm is applied within Hartree-Fock (Zicovich-Wilson, Dovesi, and Saunders, 2001) rather than DFT.

Once conduction bands are included via the disentanglement procedure, results depend both on the target dimensions of the disentangled manifold and on the states considered in the procedure (e.g., the disentanglement window). In this case, it becomes riskier to draw conclusions from the qualitative features of the MLWFs. Still, it is easy to see how MLWFs can make the connection between atomic constituents and solid-state bands, representing a formal derivation of "atoms in solids." That is, it can reveal the atomic-like orbitals that conceptually lie behind any tight-binding formulation, but that can now be obtained directly from first principles according to a well-defined procedure. For crystalline silicon, the four-dimensional manifold disentangled from the lowest part of the conduction bands gives rise to four identical antibonding orbitals (see Fig. 13) originating from the destructive interference of two atomic sp^3 orbitals centered on neighboring atoms, to be contrasted with the constructive interference shown in Fig. 2 for the valence WFs. In addition, an eight-dimensional manifold disentangled from an energy window including both the valence bands and the lowest part of the conduction bands gives rise to the atomic sp^3 tight-binding orbitals of crystalline silicon (see Fig. 14). These can form the basis of the construction of Hamiltonians

FIG. 15 (color online).   The three MLWFs derived from the O $2p$ bands of BaTiO$_3$ in the centrosymmetric structure, showing covalent hybridization with the nominally empty Ti $3d$ orbitals. The left panel shows the O$[2p_z] -$ Ti$[3d_{z^2}]$ MLWF, the central panel adds the O$[2p_y] -$ Ti$[3d_{yz}]$ MLWF, and the right panel adds to these the O$[2p_x] -$ Ti$[3d_{xz}]$ MLWF. For the locations of the ions, see Fig. 22.

for model systems (e.g., strongly correlated) or large-scale nanostructures, as discussed in Sec. VII.

These considerations also extend to more complex systems. The case of ferroelectric perovskites was studied relatively early by Marzari and Vanderbilt (1998), Baranek *et al.* (2001), and Evarestov, Smirnov, and Usvyat (2003), thanks to the presence of well-separated manifolds of bands (King-Smith and Vanderbilt, 1994). A classic example is shown in Fig. 15, showing for BaTiO$_3$ the three MLWFs per oxygen derived from the nine oxygen $2p$ bands. While in the classical ionic picture of perovskites the *B*-cation (here Ti) is completely ionized in a 4+ state, the covalent nature of the bond becomes clearly apparent here, with the MLWFs showing a clear hybridization in the form of mixed *p-d* orbitals. Such hybridization is at the origin of the ferroelectric instability, as argued by Posternak, Resta, and Baldereschi (1994). The analysis of the MLWF building blocks can also extend to quite different crystal types. For example, Cangiani *et al.* (2004) discussed the case of TiO$_2$ polytypes, where bonding MLWFs associated with the O $2s/2p$ valence manifold are seen to be similar in the rutile and anatase form, with the third polytype (brookite) an average between the two (Posternak *et al.*, 2006). Applications to other complex systems can be found, e.g., for antiferromagnetic MnO (Posternak *et al.*, 2002) or for silver halides (Evarestov, Smirnov, and Usvyat, 2004).

B. Complex and amorphous phases

Once the electronic ground state has been decomposed into well-localized orbitals, it becomes possible and meaningful to study their spatial distribution or the distribution of their centers of charge (the WFCs). Silvestrelli *et al.* (1998) were the first to argue that the WFCs can be a powerful tool for understanding bonding in low-symmetry cases, representing an insightful and an economical mapping of the continuous electronic degrees of freedom into a set of classical descriptors, i.e., the center positions and spreads of the WFs.

The benefits of this approach become apparent when studying the properties of disordered systems. In amorphous
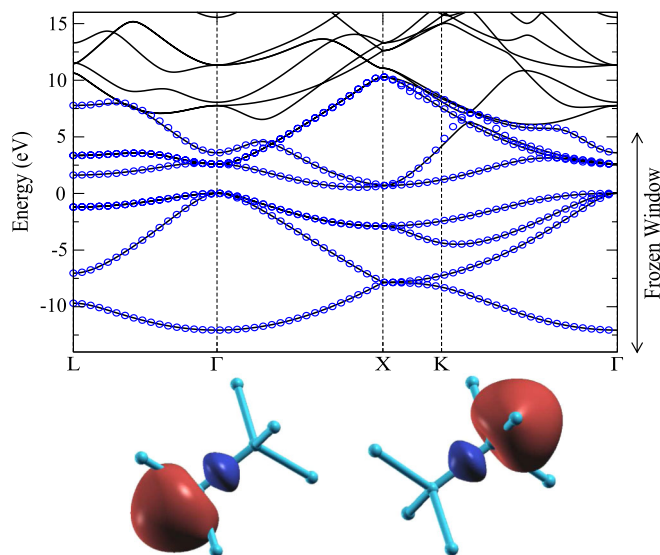

FIG. 14 (color online).   Band structure of crystalline Si and corresponding valence and conduction MLWFs. Top: Circles indicate an eight-dimensional manifold which has been disentangled from the full band structure (solid lines). The frozen window is also indicated. Bottom: Two of the eight off-bond atom-centered sp^3 MLWFs obtained from this manifold (the other six are equivalent under space-group symmetry operations; for the discussion of on-bond vs off-bond MLWFs, see Sec. IV.D).
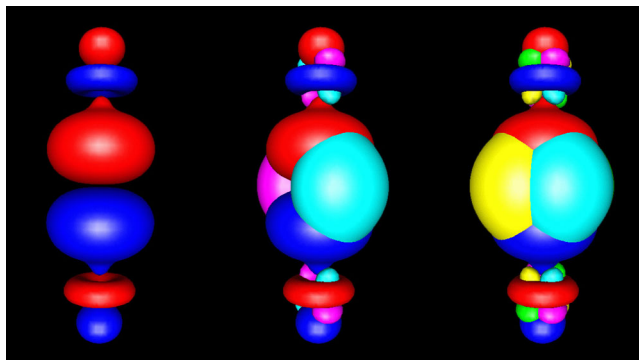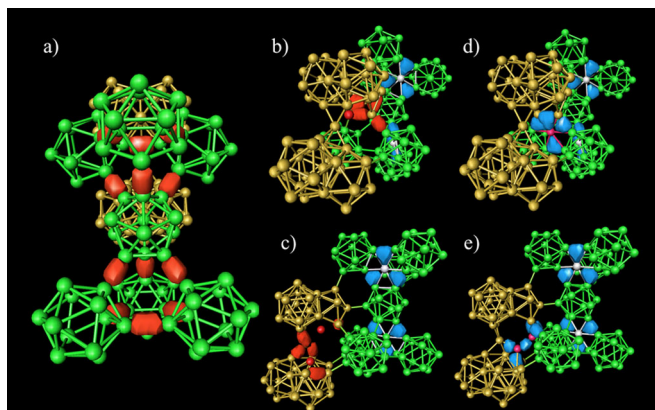
FIG. 16 (color online). Charge densities for the MLWFs in β-rhombohedral boron. Darker isosurfaces correspond to electron-deficient bonds; lighter ones correspond to fully occupied bonds. From Ogitsu *et al.*, 2009.
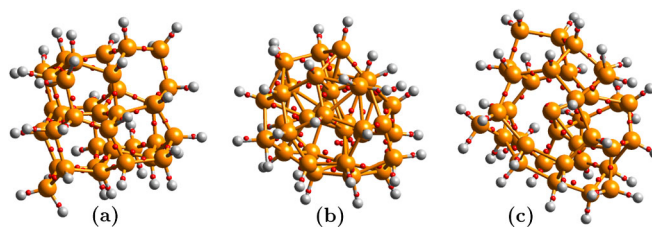

FIG. 17 (color online). Collapse and amorphization of a hydrogenated Si cluster under pressure, (a) first at 25 GPa, (b) then at 35 GPa, and (c) back to 5 GPa. Small dark spheres indicate the Wannier centers. From Martonak, Molteni, and Parrinello, 2001.

solids the analysis of the microscopic properties is usually based on the coordination number, i.e., on the number of atoms lying inside a sphere of a chosen radius r_c centered on the selected atom (r_c is typically inferred from the first minimum in the pair-correlation function). This purely geometrical analysis is completely blind to the actual electronic charge distribution, which ought to be important in any description of chemical bonding. An analysis of the full charge distribution and bonding in terms of the Wannier functions, as, for example, in Fig. 4 for the distorted tetrahedral network of amorphous silicon, would be rather complex, albeit useful to characterize the most common defects (Fornari *et al.*, 2001).

Instead, just the knowledge of the positions of the WFCs and their spreads can capture most of the chemistry in the system and can identify the defects present. In this approach, the WFCs are treated as a second species of ''classical particles'' (representing electrons), and the amorphous solid is treated as a statistical assembly of the two kinds of particles (ions and WFCs). Pair-correlation functions can thus be constructed for ions and classical electrons, leading to the definition of novel bonding criteria based on the locations of the WFCs. For the case of amorphous silicon, for example, the existence of a bond between two ions can be defined by their sharing a common WFC within a distance that is smaller than the first minimum of the silicon-WFC pair-correlation function. Following this definition, one can provide a more meaningful definition of atomic coordination number, argue for the presence (or absence) of bonds in defective configurations, and propose specific electronic signatures for identifying different defects (Silvestrelli *et al.*, 1998).

The ability of Wannier functions to capture the electronic structure of complex materials has also been demonstrated in the study of boron allotropes. Boron is almost unique among the elements in having at least four major crystalline phases, all stable or metastable at room temperature and with complex unit cells of up to 320 atoms, together with an amorphous phase. In their study of β-rhombohedral boron, Ogitsu *et al.* (2009) were able to identify and study the relation between two-center and three-center bonds and boron vacancies, identifying the most electron-deficient bonds as the most

chemically active. Examples are shown in Fig. 16. Tang and Ismail-Beigi (2009) were also able to study the evolution of 2D boron sheets as they were made more compact (from hexagonal to triangular), and showed that the in-plane bonding pattern of the hexagonal system was preserved, with only minor changes in the shape and position of the MLWFs.

Besides its application to the study of disordered networks (Meregalli and Parrinello, 2001; Lim *et al.*, 2002; Fitzhenry *et al.*, 2003), the above analysis can also be effectively employed to elucidate the chemical and electronic properties accompanying structural transformations. In work on silicon nanoclusters under pressure (Martonak, Molteni, and Parrinello, 2000, 2001; Molteni, Martonak, and Parrinello, 2001), the location of the WFCs was monitored during compressive loading (up to 35 GPa) and unloading. Some resulting configurations are shown in Fig. 17. The analysis of the ''bond angles'' formed by two WFCs and their common Si atom shows considerable departure from the tetrahedral rule at the transition pressure. The MLWFs also become significantly more delocalized at that pressure, hinting at a metallization transition similar to the one that occurs in Si in going from the diamond to the β-tin structure.

C. Defects

Interestingly, the MLWFs analysis can also point to structural defects that do not otherwise exhibit any significant electronic signature. Goedecker, Deutsch, and Billard (2002) predicted, entirely from first principles, the existence of a new fourfold-coordinated defect that is stable inside the Si lattice (see Fig. 18). This defect had not been considered before, but displays by far the lowest formation energy, at the DFT level, among all native defects in silicon. Inspection of the relevant ''defective'' MLWFs reveals that their spreads actually remain very close to those typical of crystalline silicon, and that the WFCs remain equally shared between the atoms in a typical covalent arrangement. These considerations suggest that the electronic configuration is locally almost indistinguishable from that of the perfect lattice, making this defect difficult to detect with standard electronic probes. Moreover, a low activation energy is required for the self-annihilation of this defect; this consideration, in combination with the ''stealth'' electronic signature, hints at the reason why such a defect could have eluded experimental discovery despite the fact that Si is one of the best studied materials in the history of technology.
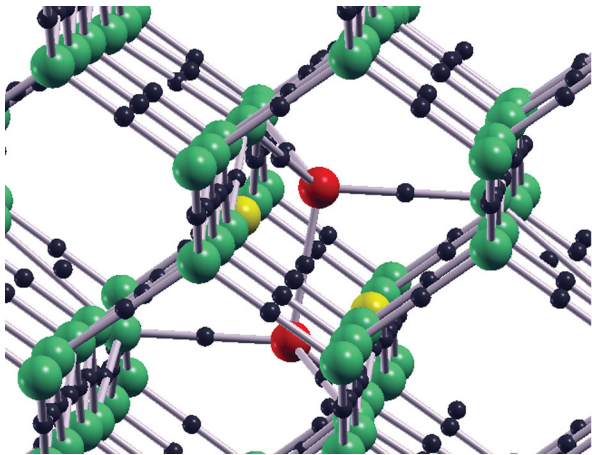
FIG. 18 (color online). The fourfold-coordinated defect in Si. Dark and intermediate spheres denote Si atoms (the former being the two displaced ones), light spheres are vacancies, and the small spheres indicate the centers of the MLWFs. Adapted from Goedecker, Deutsch, and Billard, 2002.

For the case of the silicon vacancy, MLWFs were studied for all the charge states by Corsetti and Mostofi (2011), validating the canonical Watkins model (Watkins and Messmer, 1974). This work also demonstrated the importance of including the occupied defect levels in the gap when constructing the relevant WFs, which are shown in the first two panels of Fig. 19. For the doubly charged split-vacancy configuration, the ionic relaxation is such that one of the nearest neighbors of the vacancy site moves halfway toward the vacancy, relocating to the center of an octahedral cage of silicon atoms. This gives rise to six defect WFs, each corresponding to a bond between sp^3d^2 hybrids on the central atom and dangling sp^3 orbitals on the neighbors, as shown in the last panel of Fig. 19.

D. Chemical interpretation

It should be stressed that a "chemical" interpretation of the MLWFs is most appropriate when they are formed from a unitary transformation of the occupied subspace. Whenever unoccupied states are included, MLWFs are more properly understood as forming a minimal tight-binding basis, and not necessarily as descriptors of the bonding. Nevertheless, these tight-binding states sometimes conform to our chemical intuition. For example, referring back to Fig. 6 we recall
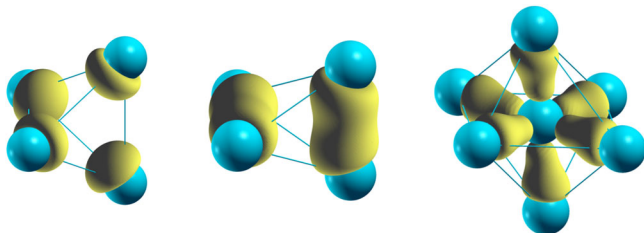

FIG. 19 (color online). Contour-surface plots of the MLWFs most strongly associated with a silicon vacancy in bulk silicon, for different charge states of the vacancy (from left to right: neutral unrelaxed, neutral relaxed, and doubly negative relaxed). Adapted from Corsetti and Mostofi, 2011.

that the band structure of graphene can be described accurately by disentangling the partially occupied π manifold from the higher free-electron parabolic bands and the antibonding sp^2 bands. One can then construct either a minimal basis of one p_z MLWF per carbon, if interested only in the $\pi/\pi^\star$ manifold around the Fermi energy, or a slightly larger set with an additional MLWF per covalent bond, if interested in describing both the partially occupied $\pi/\pi^\star$ and the fully occupied σ manifolds. In this latter case, the bond-centered MLWFs come from the constructive superposition of two sp^2 orbitals pointing toward each other from adjacent carbons (Lee, Nardelli, and Marzari, 2005).

On the contrary, as discussed in Sec. II.I.2 and shown in Fig. 8, a very good tight-binding basis for $3d$ metals such as Cu can be constructed (Souza, Marzari, and Vanderbilt, 2001) with five atom-centered d-like orbitals and two s-like orbitals in the interstitial positions. Rather than reflecting a "true" chemical entity, these represent linear combinations of sp^3 orbitals that interfere constructively at the interstitial sites, thus providing the additional variational freedom needed to describe the entire occupied space. Somewhere in between, it is worth pointing out that the atom-centered sp^3 orbitals typical of group-IV or III-V semiconductors, that can be obtained in the diamond and zinc blende structure by disentangling the lowest four conduction bands, can have a major lobe pointing either to the center of the bond or in the opposite direction (Lee, 2006; Wahn and Neugebauer, 2006). For a given spatial cutoff on the tight-binding Hamiltonian constructed from these MLWFs, it is found that the former give a qualitatively much better description of the DFT band structure than the latter, despite the counterintuitive result that the "off-bond" MLWFs are slightly more localized. The reason is that the "on-bond" MLWFs have a single dominant nearest-neighbor interaction along a bond, whereas for the off-bond MLWFs there are a larger number of weaker nearest-neighbor interactions that are not directed along the bonds (Corsetti, 2012).

E. MLWFs in first-principles molecular dynamics

The use of MLWFs to characterize electronic bonding in a complex system has been greatly aided by the implementation of efficient and robust algorithms for maximal localization of the orbitals in the case of large, and often disordered, supercells in which the Brillouin zone can be sampled at a single point, usually the zone-center Γ point (Silvestrelli *et al.*, 1998; Silvestrelli, 1999; Berghold *et al.*, 2000; Bernasconi and Madden, 2001). Such efforts and the implementation in widely available computer codes have given rise to an extensive literature dedicated to understanding and monitoring the nature of bonding in complex and realistic systems under varying thermodynamic conditions or during a chemical reaction. Such approaches are particularly useful when combined with molecular-dynamics simulations, and most applications have taken place within the framework first proposed by Car and Parrinello (1985). In fact, specialized algorithms have been developed to perform on-the-fly Car-Parrinello molecular dynamics in a Wannier representation (Sharma, Wu, and Car, 2003; Iftimie, Thomas, and Tuckerman, 2004; Wu, Selloni, and Car, 2009).

First applications were to systems as diverse as high-pressure ice (Bernasconi, Silvestrelli, and Parrinello, 1998), doped fullerenes (Billas *et al.*, 1999), adsorbed organic molecules (Silvestrelli, Ancilotto, and Toigo, 2000), ionic solids (Bernasconi, Madden, and Wilson, 2002; Posternak *et al.*, 2002), and the Ziegler-Natta polymerization (Boero, Parrinello *et al.*, 2000). This latter case is a paradigmatic example of the chemical insight that can be gleaned by following the WFCs in the course of a first-principles simulation. In the Ziegler-Natta reaction we have an interconversion of a double carbon bond into a single bond, and a characteristic agostic interaction between the C-H bond and the activated metal center. Both become immediately visible once the WFCs are monitored, greatly aiding the interpretation of the complex chemical pathways.

Car-Parrinello molecular dynamics is particularly suited to the study of liquid systems, and applications have been numerous in all areas of physical chemistry. Examples include the work of Raugei, Cardini, and Schettino (1999), Sullivan *et al.* (1999), Boero, Morikawa *et al.* (2000), Boero, Parrinello *et al.* (2000), Lightstone *et al.* (2001, 2005), Schwegler, Galli, and Gygi (2001), Tobias, Jungwirth, and Parrinello (2001), Vuilleumier and Sprik (2001), Bako, Hutter, and Palinkas (2002), Jungwirth and Tobias (2002), Raugei and Klein (2002), Kreitmeir *et al.* (2003), van Erp and Meijer (2003), Bernasconi *et al.* (2004), Blumberger *et al.* (2004), Kirchner and Hutter (2004), Leung and Rempe (2004), Odelius, Kirchner, and Hutter (2004), Saharay and Balasubramanian (2004), Heuft and Meijer (2005), Ikeda, Hirata, and Kimura (2005), Faralli *et al.* (2006), Krekeler, Hess, and Delle Site (2006), Bucher and Kuyucak (2008), Costanzo and Della Valle (2008), D'Auria, Kuo, and Tobias (2008), Salanne *et al.* (2008), Suzuki (2008), and Todorova, Hunenberger, and Hutter (2008).

Water, in particular, has been studied extensively, both at normal conditions (Grossman *et al.*, 2004; Sit *et al.*, 2007) and in high- and low-pressure phases at high temperature (Silvestrelli and Parrinello, 1999a, 1999b; Boero *et al.*, 2000a, 2000b, 2001; Romero, Silvestrelli, and Parrinello, 2001; Schwegler *et al.*, 2001) (a fast dissociation event from one of these simulations is shown in Fig. 20). Behavior in the presence of solvated ions (Lightstone *et al.*, 2001; Schwegler, Galli, and Gygi, 2001; Tobias, Jungwirth, and Parrinello, 2001; Bako, Hutter, and Palinkas, 2002; Raugei and Klein, 2002) or a hydrated electron (Boero *et al.*, 2003; Boero, 2007), or at surfaces and interfaces
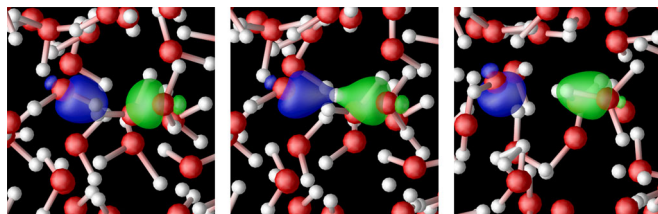

FIG. 20 (color online). Snapshots of a rapid water-molecule dissociation under high-temperature (1390 K) and high-pressure (27 GPa) conditions. Two of the MLWFs are highlighted, the darker and lighter ones being located on proton donor and acceptor molecules, respectively. From Schwegler *et al.*, 2001.

(Salvador *et al.*, 2003; Kuo and Mundy, 2004; Kuo *et al.*, 2006, 2008; Mundy and Kuo, 2006; Kudin and Car, 2008), has also been studied. Moreover, MLWFs have been used to calculate the electronic momentum density that can be measured in Compton scattering (Romero, Silvestrelli, and Parrinello, 2000). This work elucidated the relation between the anisotropy of the Compton profiles for water and the nature of hydrogen bonding (Romero, Silvestrelli, and Parrinello, 2001), and led to the suggestion that the number of hydrogen bonds present can be directly extracted from the Compton profiles (Sit *et al.*, 2007). The population of covalent bond pairs in liquid silicon and the Compton signature of covalent bonding has also recently been studied using MLWFs (Okada *et al.*, 2012).

Even more complex biochemical systems have been investigated, including wet DNA (Gervasio, Carloni, and Parrinello, 2002), HIV-1 protease (Piana *et al.*, 2001), reverse transcriptase (Sulpizi and Carloni, 2000), phosphate groups (ATP, GTP, and ribosomal units) in different environments (Alber, Folkers, and Carloni, 1999; Minehardt *et al.*, 2002; Spiegel and Carloni, 2003), drug-DNA complexes (Spiegel and Magistrato, 2006), and caspases and kinases (Sulpizi *et al.*, 2001, 2003). Extensive reviews of first-principles quantum simulations and molecular dynamics, with discussions of MLWFs in these contexts, have appeared in papers by Tuckerman and Martyna (2000), Tse (2002), Tuckerman (2002), Dovesi *et al.* (2005), Vuilleumier (2006), and Kirchner (2007), with Marx and Hutter (2009) providing a comprehensive methodological overview.

Further applications of first-principles molecular dynamics oriented specifically to extracting information about dipolar properties and dielectric responses are discussed later in Sec. V.B.3.

V. ELECTRIC POLARIZATION AND ORBITAL MAGNETIZATION

First-principles calculations of electric dipoles and orbital magnetic moments of molecular systems are straightforward. The electric dipole is

$$\mathbf{d} = -e\sum_j \langle \psi_j | \mathbf{r} | \psi_j \rangle \tag{84}$$

and the orbital moment is

$$\mathbf{m} = -\frac{e}{2c}\sum_j \langle \psi_j | \mathbf{r} \times \mathbf{v} | \psi_j \rangle, \tag{85}$$

where the sum is over occupied Hamiltonian eigenstates $|\psi_j\rangle$, $\mathbf{r}$ is the position operator, $\mathbf{v} = (i/\hbar)[H, \mathbf{r}]$ is the velocity operator, and Gaussian units are used. However, these formulas cannot easily be generalized to the case of crystalline systems, because the Hamiltonian eigenstates take the form of Bloch functions $|\psi_{n\mathbf{k}}\rangle$ that extend over all space. The problem is that matrix elements such as $\langle \psi_{n\mathbf{k}} | \mathbf{r} | \psi_{n\mathbf{k}} \rangle$ and $\langle \psi_{n\mathbf{k}} | \mathbf{r} \times \mathbf{v} | \psi_{n\mathbf{k}} \rangle$ are ill defined for such extended states (Nenciu, 1991).

To deal with this problem, the so-called ''modern theory of polarization'' (Resta, 1992, 1994; King-Smith and Vanderbilt, 1993; Vanderbilt and King-Smith, 1993) was developed in the 1990s, and a corresponding ''modern theory

of magnetization'' in the 2000s (Thonhauser *et al.*, 2005; Xiao, Shi, and Niu, 2005; Ceresoli *et al.*, 2006; Shi *et al.*, 2007; Souza and Vanderbilt, 2008). Useful reviews of these topics have appeared (Resta, 2000, 2010; Vanderbilt and Resta, 2006; Resta and Vanderbilt, 2007).

These theories can be formulated either in terms of Berry phases and curvatures or, equivalently, by working in the Wannier representation. The basic idea of the latter is to consider a large but finite sample surrounded by vacuum and carry out a unitary transformation from the set of delocalized Hamiltonian eigenstates ψ_j to a set of Wannier-like localized molecular orbitals ϕ_j. Then one can use Eq. (84) or Eq. (85), with ψ_j replaced by ϕ_j, to evaluate the electric or orbital magnetic dipole moment per unit volume in the thermodynamic limit. In doing so, care must be taken to consider whether any surface contributions survive in this limit.

In this section, we briefly review the modern theories of electric polarization and orbital magnetization and related topics. The results given in this section are valid for any set of localized WFs; maximally localized ones do not play any special role. Nevertheless, the close connection to the theory of polarization has been one of the major factors behind the resurgence of interest in WFs. Furthermore, we see that the use of MLWFs can provide a very useful, if heuristic, local decomposition of polar properties in an extended system. For these reasons, it is appropriate to review the subject here.

A. Wannier functions, electric polarization, and localization

1. Relation to Berry-phase theory of polarization

Here we briefly review the connection between the Wannier representation and the Berry-phase theory of polarization (King-Smith and Vanderbilt, 1993; Vanderbilt and King-Smith, 1993; Resta, 1994). Suppose that we have constructed via Eq. (8) a set of Bloch-like functions $|\tilde{\psi}_{n\mathbf{k}}\rangle$ that are smooth functions of $\mathbf{k}$. Inserting these in place of $|\psi_{n\mathbf{k}}\rangle$ on the right side of Eq. (3), the WFs in the home unit cell $\mathbf{R} = \mathbf{0}$ are simply

$$|\mathbf{0}n\rangle = \frac{V}{(2\pi)^3} \int_{\text{BZ}} d\mathbf{k} |\tilde{\psi}_{n\mathbf{k}}\rangle. \tag{86}$$

To find their centers of charge, we note that

$$\mathbf{r}|\mathbf{0}n\rangle = \frac{V}{(2\pi)^3} \int_{\text{BZ}} d\mathbf{k}(-i\nabla_{\mathbf{k}} e^{i\mathbf{k}\cdot\mathbf{r}})|\tilde{u}_{n\mathbf{k}}\rangle. \tag{87}$$

Performing an integration by parts and applying $\langle \mathbf{0}n|$ on the left, the center of charge is given by

$$\mathbf{r}_n = \langle \mathbf{0}n|\mathbf{r}|\mathbf{0}n\rangle = \frac{V}{(2\pi)^3} \int_{\text{BZ}} d\mathbf{k}\langle \tilde{u}_{n\mathbf{k}}|i\nabla_{\mathbf{k}}|\tilde{u}_{n\mathbf{k}}\rangle, \tag{88}$$

which is a special case of Eq. (23). Then, in the home unit cell, in addition to the ionic charges $+eZ_\tau$ located at positions $\mathbf{r}_\tau$, we can imagine electronic charges $-e$ located at positions $\mathbf{r}_n$.[13] Taking the dipole moment of this imaginary cell and dividing by the cell volume, we obtain, heuristically

---

[13]In these formulas, the sum over n includes a sum over spin. Alternatively a factor of 2 can be inserted to account explicitly for spin.

$$\mathbf{P} = \frac{e}{V}\left(\sum_\tau Z_\tau \mathbf{r}_\tau - \sum_n \mathbf{r}_n\right) \tag{89}$$

for the polarization.

This argument can be put on somewhat firmer ground by imagining a large but finite crystallite cut from the insulator of interest, surrounded by vacuum. The crystallite is divided into an ''interior'' bulklike region and a ''skin'' whose volume fraction vanishes in the thermodynamic limit. The dipole moment is computed from Eq. (84), by using LMOs ϕ_j in place of the Hamiltonian eigenfunctions ψ_j on the right-hand side. Arguing that the contribution of the skin to $\mathbf{d}$ is negligible in the thermodynamic limit and that the interior LMOs become bulk WFs, one can construct an argument that arrives again at Eq. (89).

If these arguments still seem sketchy, Eq. (89) can be rigorously justified by noting that its second term,

$$\mathbf{P}_{\text{el}} = -\frac{e}{(2\pi)^3}\sum_n \int_{\text{BZ}} d\mathbf{k}\langle \tilde{u}_{n\mathbf{k}}|i\nabla_{\mathbf{k}}|\tilde{u}_{n\mathbf{k}}\rangle, \tag{90}$$

is precisely the expression for the electronic contribution to the polarization in the Berry-phase theory (King-Smith and Vanderbilt, 1993; Vanderbilt and King-Smith, 1993; Resta, 1994), which was derived by considering the flow of charge during an arbitrary adiabatic change of the crystalline Hamiltonian.

The Berry-phase theory can be regarded as providing a mapping of the distributed quantum-mechanical electronic charge density onto a lattice of negative point charges of charge $-e$, as illustrated in Fig. 21. Then the change of polarization resulting from any physical change, such as the displacement of one atomic sublattice or the application of an electric field, can be related in a simple way to the displacements of the Wannier centers $\mathbf{r}_n$ occurring as a result of this change.

A well-known feature of the Berry-phase theory is that the polarization is only well defined modulo a quantum $e\mathbf{R}/V$, where $\mathbf{R}$ is a real-space lattice vector. Such an indeterminacy is immediately obvious from Eq. (89), since the choice of which WFs are assigned to the home unit cell ($\mathbf{R} = \mathbf{0}$), or, for that matter, which ions are assigned to it, is arbitrary. Shifting one of these objects by a lattice vector $\mathbf{R}$ merely changes $\mathbf{P}$ by the quantum. Correspondingly, it can be shown that an
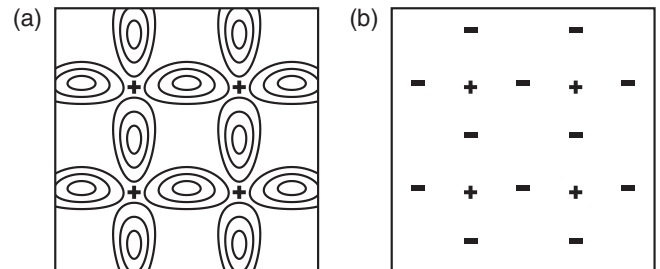

FIG. 21. Illustration of mapping from physical crystal onto equivalent point-charge system with correct dipolar properties. (a) True system composed of point ions ($+$) and charge cloud (contours). (b) Mapped system in which the charge cloud is replaced by quantized electronic charges ($-$). In the illustrated model there are two occupied bands, i.e., two Wannier functions per cell.

arbitrary change of gauge can shift individual Wannier centers $\mathbf{r}_n$ in arbitrary ways, except that the sum $\sum_n \mathbf{r}_n$ is guaranteed to remain invariant (modulo a lattice vector). The same $e\mathbf{R}/V$ describes the quantization of charge transport under an adiabatic cycle (Thouless, 1983), and indeed the shifts of Wannier charge centers under such a cycle were recently proposed as a signature of formal oxidation state in crystalline solids (Jiang, Levchenko, and Rappe, 2012).

2. Insulators in finite electric field

The theory of crystalline insulators in finite electric field $\mathcal{E}$ is a subtle one; the electric potential $-\mathcal{E} \cdot \mathbf{r}$ does not obey the conditions of Bloch's theorem, and moreover is unbounded from below, so that there is no well-defined ground state. In practice one wants to solve for a long-lived resonance in which the charge density and other properties of the insulator remain periodic, corresponding to what is meant experimentally by an insulator in a finite field. This is done by searching for local minima of the electric enthalpy per cell

$$F = E_{\mathrm{KS}} - V\mathcal{E} \cdot \mathbf{P} \qquad (91)$$

with respect to both the electronic and the ionic degrees of freedom. E_{KS} is the ordinary Kohn-Sham energy as it would be calculated at zero field, and the second term is the coupling of the field to the polarization as given in Eq. (89) (Nunes and Vanderbilt, 1994) or via the equivalent Berry-phase expression (Nunes and Gonze, 2001; Souza, Íñiguez, and Vanderbilt, 2002; Umari and Pasquarello, 2002). This approach is now standard for treating periodic insulators in finite electric fields in DFT.

3. Wannier spread and localization in insulators

We briefly touch here on another interesting connection to the theory of polarization. Resta and co-workers defined a measure of localization (Resta and Sorella, 1999; Sgiarovello, Peressi, and Resta, 2001; Resta, 2002, 2006) that distinguishes insulators from metals quite generally and showed that this localization measure reduces, in the absence of two-particle interactions or disorder, to the invariant part of the spread functional Ω_I given in Eq. (20). Moreover, Souza, Wilkens, and Martin (2000) showed that this same quantity characterizes the root-mean-square quantum fluctuations of the macroscopic polarization. Thus, while the Wannier charge centers are related to the *mean* value of $\mathbf{P}$ under quantum fluctuations, their invariant quadratic spread Ω_I is related to the corresponding *variance* of $\mathbf{P}$.

4. Many-body generalizations

In the same spirit as for the many-body WFs discussed at the end of Sec. II.J, it is possible to generalize the formulation of electric polarization and electron localization to the many-body context. One again considers N electrons in a supercell; for the present discussion we work in 1D and let the supercell have size L. The many-body theory of electric polarization was formulated in this context by Ortiz and Martin (1994), and later reformulated by Resta (1998), who introduced a "many-body position operator" $\hat{X} = \exp(i2\pi\hat{x}/L)$ defined in terms of the ordinary position operator $\hat{x} = \sum_{i=1}^{N} \hat{x}_i$. While $\langle\Psi|\hat{x}|\Psi\rangle$ is ill defined in the extended many-body ground state $|\Psi\rangle$, the matrix element $\langle\Psi|\hat{X}|\Psi\rangle$ is well defined and can be used to obtain the electric polarization, up to the usual quantum. These considerations were extended to the localization functional, and the relation between localization and polarization fluctuations, by Souza, Wilkens, and Martin (2000). The variation of the many-body localization length near an insulator-to-metal transition in 1D and 2D model systems was studied using quantum Monte Carlo (QMC) methods by Hine and Foulkes (2007). Finally, the concept of electric enthalpy was generalized to the many-body case by Umari *et al.* (2005), allowing one to calculate for the first time dielectric properties with quantum Monte Carlo methods, and applied to the case of the polarizabilities (Umari *et al.*, 2005) and hyperpolarizabilities (Umari and Marzari, 2009) of periodic hydrogen chains.

B. Local polar properties and dielectric response

Is Sec. V.A.1 we emphasized the equivalence of the $\mathbf{k}$-space Berry-phase expression for the electric polarization, Eq. (90), and the expression written in terms of the locations of the Wannier centers $\mathbf{r}_n$, Eq. (89). The latter has the advantage of being a real-space expression, thereby opening up opportunities for localized descriptions and decompositions of polar properties and dielectric responses. We emphasize again that MLWFs have no privileged role in Eq. (89); the expression remains correct for any WFs that are sufficiently well localized that the centers $\mathbf{r}_n$ are well defined. Nevertheless, one may argue heuristically that MLWFs provide the most natural local real-space description of dipolar properties in crystals and other condensed phases.

1. Polar properties and dynamical charges of crystals

Many dielectric properties of crystalline solids are most easily computed directly in the $\mathbf{k}$-space Bloch representation. Even before it was understood how to compute the polarization $\mathbf{P}$ via the Berry-phase theory of Eq. (90), it was well known how to compute derivatives of $\mathbf{P}$ using linear-response methods (de Gironcoli, Baroni, and Resta, 1989; Resta, 1992; Baroni *et al.*, 2001). Useful derivatives include the electric susceptibility $\chi_{ij} = dP_i/d\mathcal{E}_j$ and the Born (or dynamical) effective charges $Z^*_{i,\tau j} = V dP_i/dR_{\tau j}$, where i and j are Cartesian labels and $R_{\tau j}$ is the displacement of sublattice τ in direction j. With the development of the Berry-phase theory, it also became possible to compute effective charges by finite differences. Similarly, with the electric-enthalpy approach of Eq. (91) it became possible to compute electric susceptibilities by finite differences as well (Souza, Íñiguez, and Vanderbilt, 2002; Umari and Pasquarello, 2002).

The Wannier representation provides an alternative method for computing such dielectric quantities by finite differences. One computes the derivatives $dr_{n,i}/d\mathcal{E}_j$ or $dr_{n,i}/dR_{\tau j}$ of the Wannier centers by finite differences, then sums these to get the desired χ_{ij} or $Z^*_{i,\tau j}$. An example of such a calculation for Z^* in GaAs was presented already in Sec. 7 of Marzari and Vanderbilt (1997), and an application of the Wannier approach of Nunes and Vanderbilt (1994) in the density-functional context was used to compute χ by finite differences for Si and GaAs (Fernandez, Dal Corso, and

Baldereschi, 1998). Dynamical charges were computed for several TiO$_2$ phases by Cangiani *et al.* (2004) and Posternak *et al.* (2006), and, as mentioned in Sec. IV.A, observed differences between polymorphs were correlated with changes in the chemical nature of the WFs associated with OTi$_3$ structural units. Piezoelectric coefficients, which are derivatives of **P** with respect to strain, have also been carried out in the Wannier representation for ZnO and BeO by Noel *et al.* (2002).

Some of the most extensive applications of this kind have been to ferroelectric perovskites, for which the dynamical charges have been computed in density-functional and/or Hartree-Fock contexts for BaTiO$_3$, KNbO$_3$, SrTiO$_3$, and PbTiO$_3$ (Marzari and Vanderbilt, 1998; Baranek *et al.*, 2001; Evarestov, Smirnov, and Usvyat, 2003; Usvyat, Evarestov, and Smirnov, 2004). In these materials, partially covalent bonding associated with hybridization between O 2p and Ti 3d states plays a crucial role in stabilizing the ferroelectric state and generating anomalous dynamical effective charges (Posternak, Resta, and Baldereschi, 1994; Zhong, Vanderbilt, and Rabe, 1994). Recall that the dynamical, or Born, effective charge Z^* is defined as $Z^*_{i,\tau j} = V dP_i / dR_{\tau j}$ and carries units of charge. Naively, one might expect values around $+4e$ for Ti ions and $-2e$ for oxygen ions in BaTiO$_3$ based on nominal oxidation states, but instead one finds "anomalous" values that are much larger. For example, Zhong, Vanderbilt, and Rabe (1994)reported values of $+7.2e$ for Ti displacements, and $-5.7e$ for O displacements along the Ti-O-Ti chains.

This behavior can be understood (Posternak, Resta, and Baldereschi, 1994; Zhong, Vanderbilt, and Rabe, 1994) as arising from hybridization between neighboring O 2p and Ti 3d orbitals that dominate the valence and conduction bands, respectively. This hybridization, and the manner in which it contributes to an anomalous Z^*, can be visualized by inspecting the changes in the MLWFs induced by the atomic displacements. Figure 22(a) shows an O[2p_z] $-$ Ti[3d_{z^2}] MLWF

in centrosymmetric BaTiO$_3$ (Marzari and Vanderbilt, 1998). The hybridization to Ti 3d_{z^2} states appears in the form of the "donuts" surrounding the neighboring Ti atoms. When the O atom moves upward relative to the geometric center of the two neighboring Ti atoms as shown in Fig. 22(b), as it does in ferroelectrically distorted BaTiO$_3$, the hybridization strengthens for the upper O-Ti bond and weakens for the lower one, endowing the WF with more Ti 3d character on the top than on the bottom. As a result, the center of charge of the WF shifts upward, and since electrons carry negative charge, this results in a negative anomalous contribution to the Z^* of the oxygen atom. The figure illustrates this process for σ-oriented oxygen WFs, but a similar effect occurs for the π-oriented oxygen WFs, and the total anomalous dynamical charge can be accounted for quantitatively on the basis of the distortion-induced changes of each kind of WF in the crystal (Marzari and Vanderbilt, 1998).

The above illustrates the utility of the MLWFs in providing a *local* description of dielectric and polar responses in crystals. This strategy can be carried further in many ways. For example, it is possible to decompose the Z^* value for a given atom in a crystal into contributions coming from various different neighboring WFs, as was done for GaAs in Sec. 7 of Marzari and Vanderbilt (1997) and for BaTiO$_3$ by Marzari and Vanderbilt (1998). Some chemical intuition is already gained by carrying out a band-by-band decomposition of the Z^* contributions (Ghosez *et al.*, 1995; Ghosez and Gonze, 2000), but the WF analysis allows a further spatial decomposition into individual WF contributions within a band. A deeper analysis that also involves the decomposition of the WFs into atomic orbitals has been shown to provide further insight into the anomalous Z^* values in perovskites (Bhattacharjee and Waghmare, 2010).

Some insightful studies of the polar properties of polymer systems in terms of MLWFs have also been carried out. Figure 23, for example, shows the WF centers and characters for the β conformation of polyvinylidene fluoride (β-PVDF) (Nakhmanson, Nardelli, and Bernholc, 2005), one of the more promising ferroelectric polymer systems. An inspection of WF centers has also been invoked to explain the polar properties of the so-called "push-pull" polymers by Kudin, Car, and Resta (2007) and of H$_2$O ice by Lu, Gygi, and Galli (2008). Finally, we note an interesting recent study in which
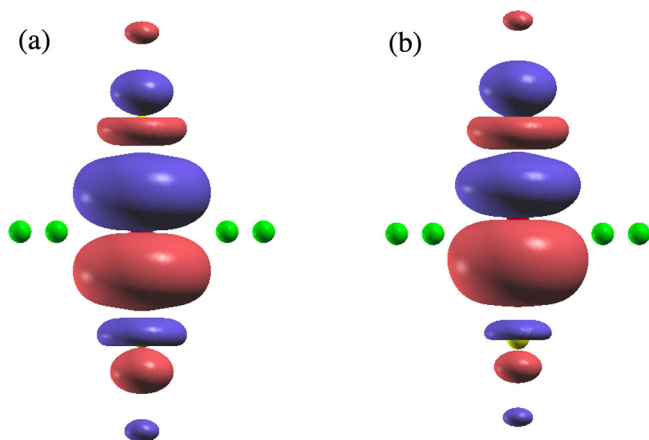
FIG. 22 (color online). Amplitude isosurface plots of the maximally localized O[2p_z] $-$ Ti[3d_{z^2}] Wannier functions in BaTiO$_3$. O is at the center, surrounded by a plaquette of four light Ba atoms; above and below are Ti atoms, almost hidden. (a) Centrosymmetric structure. (b) Ferroelectric structure in which the central O is displaced upward relative to the neighboring Ti atoms. Adapted from Marzari and Vanderbilt, 1998.
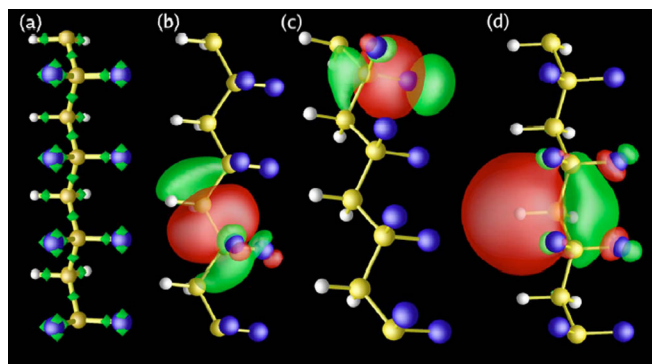
FIG. 23 (color online). MLWFs for a β-PVDF polymer chain. (a) MLWF charge centers, indicated by diamonds. (b)–(d) MLWFs localized on C-C, C-F, and C-H bonds, respectively. From Nakhmanson, Nardelli, and Bernholc, 2005.

changes in polarization induced by corrugations in BN sheets were analyzed in terms of WFs (Naumov, Bratkovsky, and Ranjan, 2009).

2. Local dielectric response in layered systems

In a similar way, the theoretical study of dielectric properties of ultrathin films and superlattices can also be enriched by a local analysis. Two approaches have been introduced in the literature. In one, the local *x*-*y*-averaged electric field $\bar{\mathcal{E}}_z(z)$ is calculated along the stacking direction z, and then the local dielectric permittivity profile $\varepsilon(z) = \bar{\mathcal{E}}_z(z)/\bar{D}_z$ or inverse permittivity profile $\varepsilon^{-1}(z) = \bar{D}_z/\bar{\mathcal{E}}_z(z)$ is plotted, where $\bar{D}_z$ is the *x*-*y*-averaged electric displacement field (constant along z in the absence of free charge) determined via a Berry-phase calculation of P_z or by inspection of $\bar{\mathcal{E}}_z$ in a vacuum region. Such an approach has been applied to study dielectric materials such as SiO_2 and HfO_2 interfaced to Si (Giustino, Umari, and Pasquarello, 2003; Giustino and Pasquarello, 2005; Shi and Ramprasad, 2006, 2007) and perovskite films and superlattices (Stengel and Spaldin, 2006a, 2006b).

The second approach is to use a Wannier analysis to assign a dipole moment to each layer. This approach, based on the concept of hybrid WFs discussed in Sec. II.H, was pioneered by Giustino, Umari, and Pasquarello (2003) and Giustino and Pasquarello (2005) and used by them to study Si/SiO_2 interfaces and related systems. Later applications to perovskite oxide films and superlattices have been fairly extensive. The essential observation is that, when studying a system that is layered or stacked along the z direction, one can still work with Bloch functions labeled by k_x and k_y while carrying out a Wannier construction or analysis only along z. Since the extraction of Wannier centers in 1D is rather trivial, even in the multiband case (Marzari and Vanderbilt, 1997; Sgiarovello, Peressi, and Resta, 2001; Bhattacharjee and Waghmare, 2005), it is not difficult to construct a ''Wannier center band structure'' $\bar{z}(k_x, k_y)$, and use the planar-averaged values to assign dipole moments to layers. This approach was demonstrated by Wu *et al.* (2006), as shown in Fig. 24, and has since been used to study perovskite superlattices and artificial nanostructures (Wu *et al.*, 2008; Murray and

FIG. 24 (color online). Dispersion of hybrid WF-center positions along z as a function of (k_x, k_y) for a superlattice composed of alternating layers of $SrTiO_3$ (sublayers 1A and 1B) and $BaTiO_3$ (sublayers 2A and 2B). From Wu *et al.*, 2006.

Vanderbilt, 2009). In a related development, Stengel and Spaldin (2006a) introduced a Wannier-based method for computing polarizations along z and studying electric fields along z that work even in the case in which the stacking includes metallic layers, as long as the system is effectively insulating along z (Stengel and Spaldin, 2007). This allows for first-principles calculations of the nonlinear dielectric response of ultrathin capacitors and related structures under finite bias, providing an insightful avenue to the study of finite-size and dead-layer effects in such systems (Stengel, Spaldin, and Vanderbilt, 2009a, 2009b; Stengel, Vanderbilt, and Spaldin, 2009).

3. Condensed molecular phases and solvation

Wannier-function methods have also played a prominent role in the analysis of polar and dielectric properties of dipolar liquids, mainly H_2O and other H-bonded liquids. While the dipole moment of an isolated H_2O molecule is obviously well defined, a corresponding definition is not easy to arrive at in the liquid phase where molecules are in close contact with each other. An influential development was the proposal made by Silvestrelli and Parrinello (1999a, 1999b) that the dipole moment of a solvated molecule could be defined in terms of positive charges on ionic cores and negative charges located at the centers of the MLWFs. Using this definition, they found that the water-molecule dipole is somewhat broadly distributed, but has an average value of about 3.0 D, about 60% higher than in the gas phase. These features were shown to be in conflict with the behavior of widely used empirical models.

Of course, such a definition in terms of the dipole of the molecular WF-center configuration remains heuristic at some level. For example, this local measure of the dipole does not appear to be experimentally measurable even in principle, and clearly the use of one of the alternative measures of maximal localization discussed in Sec. III.A would give rise to slightly different values. Nevertheless, the approach has been widely adopted. For example, subsequent work elaborated (Sagui *et al.*, 2004; Dyer and Cummings, 2006) and extended this analysis to water in supercritical conditions (Boero *et al.*, 2000a, 2000b), confined geometries (Dellago and Naor, 2005; Coudert, Vuilleumier, and Boutin, 2006), and with solvated ions present (Scipioni, Schmidt, and Boero, 2009), and compared the results obtained with different exchange-correlation functionals (Todorova *et al.*, 2006).

It should be noted that the decomposition into Wannier dipoles is closer to the decomposition of the charge density into static (Szigeti) charges than to a decomposition into dynamical (Born) charges. The first one corresponds to a spatial decomposition of the total electronic charge density, while the second is connected to the force that appears on an atom in response to an applied electric field. As a counterpoint to the WF-based definition, therefore, Pasquarello and Resta (2003) argued that a definition based on these forces provides a more fundamental basis for inspecting molecular dipoles in liquids. In particular, they define a second-rank tensor as the derivative of the torque on the molecule with respect to an applied electric field, and finding that this is typically dominated by its antisymmetric part, they identify the latter (rewritten as an axial vector) as the molecular
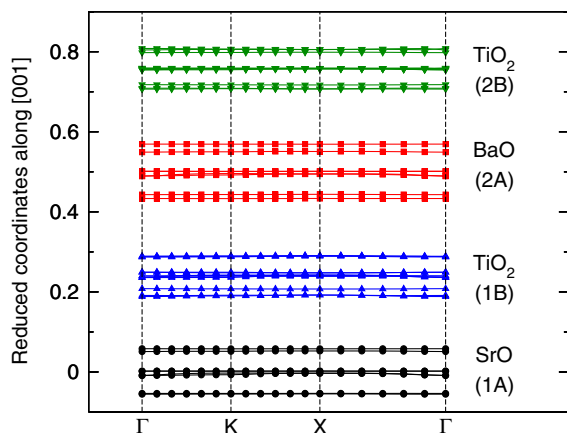
dipole. Surprisingly, they find that the magnitude of this dipole vector is typically only about 2.1 D in liquid water, much less than the value obtained from the WF analysis.

Clearly the WF-based and force-based approaches to defining molecular dipoles provide complementary perspectives, and a more complete reconciliation of these viewpoints is the subject of ongoing work.

Finally, we note that there is extensive literature in which Car-Parrinello molecular-dynamics simulations are carried out for H_2O and other liquids, as mentioned in Sec. IV.E and surveyed in several reviews (Tuckerman and Martyna, 2000; Tse, 2002; Tuckerman, 2002; Kirchner, 2007). Using such approaches, it is possible to compute the dynamical dipole-dipole correlations of polar liquids and compare the results with experimental infrared absorption spectra. While it is possible to extract the needed information from the time-time correlation function of the total polarization $\mathbf{P}(t)$ of the entire supercell as calculated using the Berry-phase approach, methods which follow the time evolution of local dipoles, as defined via WF-based methods, provide additional insight and efficiency (Bernasconi, Silvestrelli, and Parrinello, 1998; Pasquarello and Resta, 2003; Sharma, Resta, and Car, 2005, 2007; McGrath *et al.*, 2007; Chen *et al.*, 2008) and can easily be extended to other kinds of molecular systems (Gaigeot and Sprik, 2003; Gaigeot *et al.*, 2005; Gaigeot, Martinez, and Vuilleumier, 2007; Pagliai *et al.*, 2008). The applicability of this kind of approach has benefited greatly from the development of methods for computing WFs and their centers ''on the fly'' during Car-Parrinello molecular-dynamics simulations (Sharma, Wu, and Car, 2003; Iftimie, Thomas, and Tuckerman, 2004; Wu, Selloni, and Car, 2009).

C. Magnetism and orbital currents

1. Magnetic insulators

Just as an analysis in terms of WFs can help clarify the chemical nature of the occupied states in an ordinary insulator, they can also help describe the orbital and magnetic ordering in a magnetic insulator.

In the magnetic case, the maximal localization proceeds in the same way as outlined in Sec. II, with trivial extensions needed to handle the magnetic degrees of freedom. In the case of the local (or gradient-corrected) spin-density approximation, in which spin-up and spin-down electrons are treated independently, one simply carries out the maximal-localization procedure independently for each manifold. In the case of a spinor calculation in the presence of spin-orbit interaction, one instead implements the formalism of Sec. II treating all wave functions as spinors. For example, each matrix element on the right-hand side of Eq. (27) is computed as an inner product between spinors, and the dimension of the resulting matrix is the number of occupied spin bands in the insulator.

Several examples of such an analysis have appeared in the literature. For example, applications to simple antiferromagnets such as MnO (Posternak *et al.*, 2002), novel insulating ferromagnets and antiferromagnets (Ku *et al.*, 2002, 2003), and complex magnetic ordering in rare-earth manganates

(Picozzi *et al.*, 2008; Yamauchi *et al.*, 2008) have proven to be illuminating.

2. Orbital magnetization and NMR

In a ferromagnetic (or ferrimagnetic) material, the total magnetization has two components. One arises from electron spin and is proportional to the excess population of spin-up over spin-down electrons; a second corresponds to circulating orbital currents. The spin contribution is typically dominant over the orbital one [e.g., by a factor of 10 or more in simple ferromagnets such as Fe, Ni, and Co (Ceresoli, Gerstmann *et al.*, 2010)], but the orbital component is also of interest, especially in unusual cases in which it can dominate, or in the context of experimental probes, such as the anomalous Hall conductivity (AHC), that depend on orbital effects. Note that inclusion of the spin-orbit interaction is essential for any description of orbital magnetic effects.

Naively one might imagine computing the orbital magnetization $\mathbf{M}_{\mathrm{orb}}$ as the thermodynamic limit of Eq. (85) per unit volume for a large crystallite. However, as discussed at the beginning of Sec. V, Bloch matrix elements of the position operator $\mathbf{r}$ and the circulation operator $\mathbf{r} \times \mathbf{v}$ are ill defined. Therefore, such an approach is not suitable. Unlike for the case of electric polarization, however, there is a simple and fairly accurate approximation that has long been used to compute $\mathbf{M}_{\mathrm{orb}}$: one divides space into muffin-tin spheres and interstitial regions, computes the orbital circulation inside each sphere as a spatial integral of $\mathbf{r} \times \mathbf{J}$, and sums these contributions. Since most magnetic moments are fairly local, such an approach is generally expected to be reasonably accurate.

Nevertheless, it is clearly of interest to have available an exact expression for $\mathbf{M}_{\mathrm{orb}}$ that can be used to test the approximate muffin-tin approach and to treat cases in which itinerant contributions are not small. The solution to this problem has been developed recently, leading to a closed-form expression for $\mathbf{M}_{\mathrm{orb}}$ as a bulk Brillouin-zone integral. Derivations of this formula via a semiclassical (Xiao, Shi, and Niu, 2005) or long-wave quantum (Shi *et al.*, 2007) approach are possible, but here we emphasize the derivation carried out in the Wannier representation (Thonhauser *et al.*, 2005; Ceresoli *et al.*, 2006; Souza and Vanderbilt, 2008). For this purpose, we restrict our interest to insulating ferromagnets. For the case of electric polarization, the solution to the problem of $\mathbf{r}$ matrix elements was sketched in Sec. V.A.1, and a heuristic derivation of Eq. (89) was given in the paragraph following that equation. A similar analysis was given in the above references for the case of orbital magnetization, as follows.

Briefly, one again considers a large but finite crystallite cut from the insulator of interest, divides it into interior and skin regions, and transforms from extended eigenstates to LMOs ϕ_j. For simplicity, we consider the case of a two-dimensional insulator with a single occupied band. The interior gives a rather intuitive local circulation (LC) contribution to the orbital magnetization of the form

$$M_{\mathrm{LC}} = -\frac{e}{2A_0 c} \langle \mathbf{0} | \mathbf{r} \times \mathbf{v} | \mathbf{0} \rangle, \tag{92}$$

where A_0 is the unit cell area, since in the interior the LMOs ϕ_j are really just bulk WFs. This time, however, the skin

contribution does not vanish. The problem is that $\langle\phi_j|\mathbf{v}|\phi_j\rangle$ is nonzero for LMOs in the skin region, and the pattern of these velocity vectors is such as to describe a current circulating around the boundary of the sample, giving a second "itinerant circulation" (IC) contribution that can, after some manipulations, be written in terms of bulk WFs as

$$M_{\mathrm{IC}} = -\frac{e}{2A_0 c\hbar}\sum_{\mathbf{R}}[R_x\langle\mathbf{R}|y|\mathbf{0}\rangle - R_y\langle\mathbf{R}|x|\mathbf{0}\rangle]. \quad (93)$$

When these contributions are converted back to the Bloch representation and added together, one finally obtains

$$\mathbf{M}_{\mathrm{orb}} = \frac{e}{2\hbar c}\,\mathrm{Im}\int\frac{d^2k}{(2\pi)^2}\langle\partial_{\mathbf{k}}u_{\mathbf{k}}|\times(H_{\mathbf{k}}+E_{\mathbf{k}})|\partial_{\mathbf{k}}u_{\mathbf{k}}\rangle, \quad (94)$$

which is the desired $\mathbf{k}$-space bulk expression for the orbital magnetization (Thonhauser *et al.*, 2005).[14] The corresponding argument for multiple occupied bands in three dimensions follows similar lines (Ceresoli *et al.*, 2006; Souza and Vanderbilt, 2008), and the resulting formula has recently been implemented in the context of pseudopotential plane-wave calculations (Ceresoli, Gerstmann *et al.*, 2010). Interestingly, it was found that the interstitial contribution, defined as the difference between the total orbital magnetization, Eq. (94), and the muffin-tin result, is not always negligible. In bcc Fe, for example, it amounts to more than 30% of the spontaneous orbital magnetization, and its inclusion improves the agreement with gyromagnetic measurements.

The ability to compute the orbital magnetization is also of use in obtaining the magnetic shielding of nuclei. This is responsible for the chemical shift effect observed in nuclear magnetic resonance (NMR) experiments. A first-principles theory for magnetic shielding in solids was established by examining the perturbative response to a periodic magnetic field in the long wavelength limit (Mauri, Pfrommer, and Louie, 1996; Pickard and Mauri, 2001). An alternative perturbative approach used a WF representation of the electronic structure together with a periodic position operator (Sebastiani and Parrinello, 2001; Sebastiani *et al.*, 2002; Sebastiani, 2003). However, magnetic shieldings can also be computed using a "converse" approach in which one uses Eq. (94) to compute the orbital magnetization induced by a fictitious point magnetic dipole on the nucleus of interest (Thonhauser *et al.*, 2009; Ceresoli, Marzari *et al.*, 2010). The advantage of such approach is that it does not require linear-response theory, and so it is amenable to large-scale calculations or complex exchange-correlation functionals (e.g., including Hubbard U corrections, or Hartree-Fock exchange), albeit at the cost of typically one self-consistent iteration for every nucleus considered. Such converse approach has then been extended also to the calculation of the EPR g tensor by Ceresoli, Gerstmann *et al.* (2010).

---

[14]In the case of metals Eq. (94) must be modified by adding a -2μ term inside the parenthesis, with μ the chemical potential (Xiao, Shi, and Niu, 2005; Ceresoli *et al.*, 2006). Furthermore, the integration is now restricted to the *occupied* portions of the Brillouin zone.

3. Berry connection and curvature

Some of the concepts touched on in the previous section can be expressed in terms of the $\mathbf{k}$-space Berry connection

$$\mathbf{A}_{n\mathbf{k}} = \langle u_{n\mathbf{k}}|i\nabla_{\mathbf{k}}|u_{n\mathbf{k}}\rangle \quad (95)$$

and Berry curvature

$$\mathcal{F}_{n\mathbf{k}} = \nabla_{\mathbf{k}}\times\mathbf{A}_{n\mathbf{k}} \quad (96)$$

of band n. In particular, the contributions of this band to the electric polarization of Eq. (90), and to the second term in the orbital magnetization expression of Eq. (94), are proportional to the Brillouin-zone integrals of $\mathbf{A}_{n\mathbf{k}}$ and $E_{n\mathbf{k}}\mathcal{F}_{n\mathbf{k}}$, respectively. These quantities also play a role in Sec. V.C.4 and in the discussion of the anomalous Hall conductivity and related issues in Sec. VI.C.

4. Topological insulators and orbital magnetoelectric response

There has recently been a blossoming of interest in so-called topological insulators, i.e., insulators that cannot be adiabatically connected to ordinary insulators without a gap closure. Hasan and Kane (2010) and Hasan and Moore (2011) provided excellent reviews of the background, current status of this field, and references into the literature.

One can distinguish two kinds of topological insulators. First, insulators having broken time-reversal (T) symmetry (e.g., insulating ferromagnets and ferrimagnets) can be classified by an integer Chern invariant that is proportional to the Brillouin-zone integral of the Berry curvature $\mathcal{F}_{n\mathbf{k}}$ summed over occupied bands n. Ordinary insulators are characterized by a zero value of the invariant. An insulator with a nonzero value would behave like an integer quantum Hall system, but without the need for an external magnetic field; such systems are usually denoted as "quantum anomalous Hall" (QAH) insulators. While no examples are known to occur in nature, tight-binding models exhibiting such a behavior are not hard to construct (Haldane, 1988). It can be shown that a Wannier representation is not possible for a QAH insulator, and Thonhauser and Vanderbilt (2006) explored the way in which the usual Wannier construction breaks down for model systems.

Second, depending on how their Bloch functions wrap the Brillouin zone, nonmagnetic (T-invariant) insulators can be sorted into two classes denoted as "$\mathcal{Z}_2$ even" and "$\mathcal{Z}_2$ odd" (after the name $\mathcal{Z}_2$ of the group $\{0,1\}$ under addition modulo 2). Most (i.e., "normal") insulators are $\mathcal{Z}_2$ even, but strong spin-orbit effects can lead to the $\mathcal{Z}_2$-odd state, for which the surface-state dispersions are topologically required to display characteristic features that are amenable to experimental verification. Several material realizations of $\mathcal{Z}_2$-odd insulators have now been confirmed both theoretically and experimentally (Hasan and Kane, 2010; Hasan and Moore, 2011).

In a related development, the orbital magnetoelectric coefficient $\alpha_{ij} = \partial M_{\mathrm{orb},j}/\partial\mathcal{E}_i$ was found to contain an isotropic contribution having a topological character (the "axion" contribution, corresponding to an $\mathcal{E}\cdot\mathbf{B}$ term in the effective Lagrangian). This term can be written as a Brillouin-zone integral of the Chern-Simons three-form, defined in terms of multiband generalizations of the Berry connection $\mathbf{A}_{\mathbf{k}}$ and
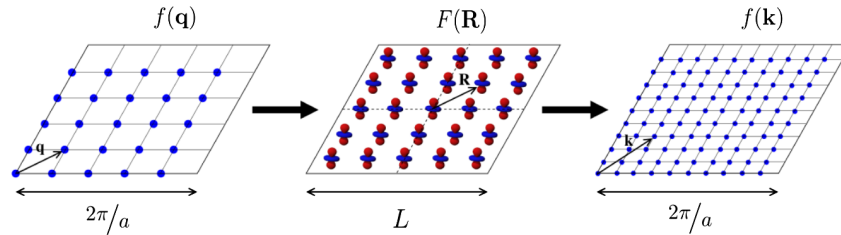
FIG. 25 (color online). Schematic overview of the Wannier interpolation procedure. The left panel shows the BZ mesh **q** used in the first-principles calculation, where the quantity of interest $f(\mathbf{q})$ is explicitly calculated. The Wannier-transformed quantity $F(\mathbf{R})$ is strongly localized near the origin of the equivalent supercell, shown in the middle panel with WFs at the lattice points. The right panel shows a dense mesh of interpolation points **k** in the BZ, where the quantity $f(\mathbf{k})$ is evaluated at low cost starting from $F(\mathbf{R})$.

curvature $\mathcal{F}_{\mathbf{k}}$ introduced in Sec. V.C.3 (Qi, Hughes, and Zhang, 2008; Essin, Moore, and Vanderbilt, 2009). The Chern-Simons magnetoelectric coupling has been evaluated from first principles with the help of WFs for both topological and ordinary insulators (Coh *et al.*, 2011).

A careful generalization of Eq. (94) to the case in which a finite electric field is present has been carried out by Malashevich *et al.* (2010) in the Wannier representation using arguments similar to those in Secs. V.A.1 and V.A.2 and used to derive a complete expression for the orbital magnetoelectric response, of which the topological Chern-Simons term is only one contribution (Essin *et al.*, 2010; Malashevich *et al.*, 2010).

VI. WANNIER INTERPOLATION

Localized Wannier functions are often introduced in textbooks as a formally exact localized basis spanning a band, or a group of bands, and their existence provides a rigorous justification for the TB interpolation method (Ashcroft and Mermin, 1976; Harrison, 1980).

In this section we explore the ways in which WFs can be used as an exact or very accurate TB basis, allowing one to perform, very efficiently and accurately, a number of operations on top of a conventional first-principles calculation. The applications of this "Wannier interpolation" technique range from simple band-structure plots to the evaluation of various physical quantities as BZ integrals. The method is particularly useful in situations where a fine sampling of the BZ is required to converge the quantity of interest. This is often the case for metals, as the presence of a Fermi surface introduces sharp discontinuities in **k** space.

The Wannier interpolation procedure is depicted schematically in Fig. 25. The actual first-principles calculation is carried out on a relatively coarse uniform reciprocal-space mesh **q** (left panel), where the quantity of interest $f(\mathbf{q})$ is calculated from the Bloch eigenstates. The states in the selected bands are then transformed into WFs, and $f(\mathbf{q})$ is transformed accordingly into $F(\mathbf{R})$ in the Wannier representation (middle panel). By virtue of the spatial localization of the WFs, $F(\mathbf{R})$ decays rapidly with $|\mathbf{R}|$. Starting from this short-range real-space representation, the quantity f can now be accurately interpolated onto an arbitrary point **k** in reciprocal space by carrying out an inverse transformation (right panel). This procedure will succeed in capturing variations in $f(\mathbf{k})$ over reciprocal lengths smaller than the first-principles mesh spacing Δq, provided that the linear dimensions

$L = 2\pi/\Delta q$ of the equivalent supercell are large compared to the decay length of the WFs.

A. Band-structure interpolation

The simplest application of Wannier interpolation is to generate band-structure plots. We describe the procedure in some detail, as the same concepts and notations reappear in the more advanced applications to follow.

From the WFs spanning a group of J bands, a set of Bloch-like states can be constructed using Eq. (4), repeated here with a slightly different notation,

$$|\psi_{n\mathbf{k}}^{\mathrm{W}}\rangle = \sum_{\mathbf{R}} e^{i\mathbf{k}\cdot\mathbf{R}} |\mathbf{R}n\rangle \quad (n = 1, \dots, J), \qquad (97)$$

where the conventions of Eqs. (12) and (13) have been adopted. This has the same form as the Bloch-sum formula in tight-binding theory, with the WFs playing the role of the atomic orbitals. The superscript W serves as a reminder that the states $|\psi_{n\mathbf{k}}^{\mathrm{W}}\rangle$ are generally not eigenstates of the Hamiltonian.[15] We say that they belong to the *Wannier gauge*.

At a given **k**, the Hamiltonian matrix elements in the space of the J bands is represented in the Wannier gauge by the matrix

$$H_{\mathbf{k},nm}^{\mathrm{W}} = \langle\psi_{\mathbf{k}n}^{\mathrm{W}}|H|\psi_{\mathbf{k}m}^{\mathrm{W}}\rangle = \sum_{\mathbf{R}} e^{i\mathbf{k}\cdot\mathbf{R}} \langle\mathbf{0}n|H|\mathbf{R}m\rangle. \qquad (98)$$

In general this is a nondiagonal matrix in the bandlike indices, and the interpolated eigenenergies are obtained by diagonalization,

$$H_{\mathbf{k},nm}^{\mathrm{H}} = [U_{\mathbf{k}}^{\dagger} H_{\mathbf{k}}^{\mathrm{W}} U_{\mathbf{k}}]_{nm} = \delta_{nm} \bar{\epsilon}_{n\mathbf{k}}. \qquad (99)$$

In the following, it is useful to view the unitary matrices $U_{\mathbf{k}}$ as transforming between the Wannier gauge on the one hand, and the Hamiltonian (H) gauge (in which the projected Hamiltonian is diagonal), on the other hand.[16] From this point

---

[15]In Sec. II the rotated Bloch states $|\psi_{n\mathbf{k}}^{\mathrm{W}}\rangle$ were denoted by $|\tilde{\psi}_{n\mathbf{k}}\rangle$; see Eq. (8).

[16]The unitary matrices $U_{\mathbf{k}}$ are related to, but not the same as, the matrices $U^{(\mathbf{k})}$ introduced in Eq. (8). The latter are obtained as described in Secs. II.B and II.C. In the present terminology, they transform from the Hamiltonian to the Wannier gauge on the mesh used in the first-principles calculation. Instead, $U_{\mathbf{k}}$ transforms from the Wannier to the Hamiltonian gauge on the interpolation mesh. That is, the matrix $U_{\mathbf{k}}$ is essentially an interpolation of the matrix $[U^{(\mathbf{k})}]^{\dagger}$.

forward we adopt a condensed notation in which band indices are no longer written explicitly, so that, for example, $H^{\mathrm{H}}_{\mathbf{k},nm} = \langle \psi^{\mathrm{H}}_{\mathbf{k}n} | H | \psi^{\mathrm{H}}_{\mathbf{k}m} \rangle$ is now written as $H^{\mathrm{H}}_{\mathbf{k}} = \langle \psi^{\mathrm{H}}_{\mathbf{k}} | H | \psi^{\mathrm{H}}_{\mathbf{k}} \rangle$, and matrix multiplications are implicit. Then Eq. (99) implies that the transformation law for the Bloch states is

$$|\psi^{\mathrm{H}}_{\mathbf{k}}\rangle = |\psi^{\mathrm{W}}_{\mathbf{k}}\rangle U_{\mathbf{k}}. \tag{100}$$

If we insert into Eqs. (98) and (99) a wave vector belonging to the first-principles grid, we simply recover the first-principles eigenvalues $\epsilon_{n\mathbf{k}}$, while for arbitrary $\mathbf{k}$ the resulting $\bar{\epsilon}_{n\mathbf{k}}$ interpolate smoothly between the values on the grid. (This is strictly true only for an isolated group of bands. When using disentanglement, the interpolated bands can deviate from the first-principles ones outside the frozen energy window, as discussed in Sec. II.I in connection with Fig. 5.)

Once the matrices $\langle \mathbf{0} | H | \mathbf{R} \rangle$ have been tabulated, the band structure can be calculated very inexpensively by Fourier transforming [Eq. (98)] and diagonalizing [Eq. (99)] matrices of rank J. Note that J, the number of WFs per cell, is typically much smaller than the number of basis functions (e.g., plane waves) used in the first-principles calculation.

In practice the required matrix elements are obtained by inverting Eq. (98) over the first-principles grid,

$$\langle \mathbf{0} | H | \mathbf{R} \rangle = \frac{1}{N} \sum_{\mathbf{q}} e^{-i\mathbf{q}\cdot\mathbf{R}} \langle \psi^{\mathrm{W}}_{\mathbf{q}} | H | \psi^{\mathrm{W}}_{\mathbf{q}} \rangle$$
$$= \frac{1}{N} \sum_{\mathbf{q}} e^{-i\mathbf{q}\cdot\mathbf{R}} V^{\dagger}_{\mathbf{q}} E_{\mathbf{q}} V_{\mathbf{q}}. \tag{101}$$

Here N is the number of grid points, $E_{\mathbf{q}}$ is the diagonal matrix of first-principles eigenenergies, and $V_{\mathbf{q}}$ is the matrix defined in Eq. (50), which converts the $\mathcal{J}_{\mathbf{q}}$ *ab initio* eigenstates into the $J \leq \mathcal{J}_{\mathbf{q}}$ Wannier-gauge Bloch states,

$$|\psi^{\mathrm{W}}_{\mathbf{q}}\rangle = |\psi_{\mathbf{q}}\rangle V_{\mathbf{q}}. \tag{102}$$

The strategy outlined above (Souza, Marzari, and Vanderbilt, 2001) is essentially the Slater-Koster interpolation method. However, while the Hamiltonian matrix elements in the localized basis are treated as adjustable parameters in empirical TB, they are calculated from first principles here. A similar interpolation strategy is widely used to obtain phonon dispersions starting from the interatomic force constants calculated with density-functional perturbation theory (Baroni *et al.*, 2001). We return to this analogy between phonons and tight-binding electrons (Martin, 2004) when describing the interpolation of the electron-phonon matrix elements in Sec. VI.D.

Wannier band-structure interpolation is extremely accurate. By virtue of the exponential localization of the WFs within the periodic supercell (see footnote 2), the magnitude of the matrix elements $\langle \mathbf{0} | H | \mathbf{R} \rangle$ decreases rapidly with $|\mathbf{R}|$, and this exponential localization is preserved even in the case of metals, provided a smooth subspace has been disentangled. As the number of lattice vectors included in the summation in Eq. (98) equals the number of first-principles mesh points, beyond a certain mesh density the error incurred decreases exponentially (Yates *et al.*, 2007). In the following we illustrate the method with a few representative examples selected from the literature.
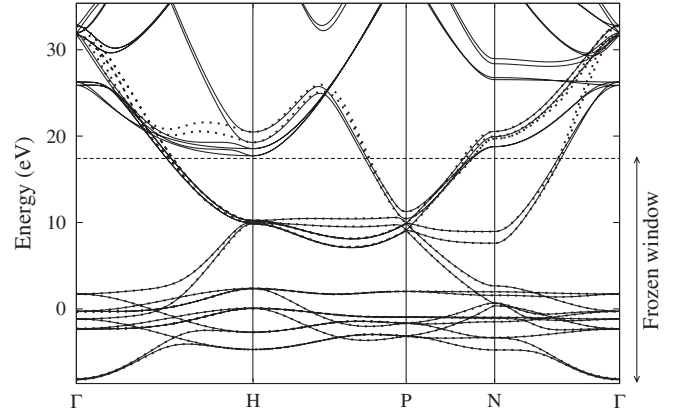
FIG. 26. Band structure of ferromagnetic bcc Fe with spin-orbit coupling included. Solid lines: Original band structure from a conventional first-principles calculation. Dotted lines: Wannier-interpolated band structure. The zero of energy is the Fermi level. From Wang *et al.*, 2006.

1. Spin-orbit-coupled bands of bcc Fe

As a first application, we consider the relativistic band structure of bcc Fe. Because of the spin-orbit interaction, the spin density is not perfectly collinear, and the Bloch eigenstates are spinors. As mentioned in Sec. V.C.1, spinor WFs can be constructed via a trivial extension of the procedure described in Sec. II for the nonmagnetic (spinless) case. It is also possible to further modify the Wannierization procedure so as to produce two separate subsets of spinor WFs: one with a predominantly spin-up character, and the other with a predominantly spin-down character (Wang *et al.*, 2006).

Using this modified procedure, a set of nine disentangled WFs per spin channel was obtained for bcc Fe by Wang *et al.* (2006), consisting of three t_{2g} d-like atom-centered WFs and six sp^3d^2-like hybrids pointing along the cubic directions. A frozen energy window was chosen as indicated in Fig. 26, so that these 18 WFs describe exactly all the occupied valence states, as well as the empty states up to approximately 18 eV above the Fermi level.

The interpolated bands obtained using an $8 \times 8 \times 8$ $\mathbf{q}$ grid in the full BZ are shown as dashed lines in Fig. 26. The comparison with the first-principles bands (solid lines) reveals essentially perfect agreement within the frozen energy window. This is even more evident in Fig. 27, where we zoom in on the interpolated band structure near the Fermi level along Γ-H, and color code it according to the spin projection along the quantization axis. The vertical dotted lines indicate points on the $\mathbf{q}$ mesh. For comparison, we show as open circles the eigenvalues calculated directly from first principles around a weak spin-orbit-induced avoided crossing between two bands of opposite spin. It is apparent that the interpolation procedure succeeds in resolving details of the true band structure on a scale much smaller than the spacing between $\mathbf{q}$ points.

2. Band structure of a metallic carbon nanotube

As a second example, we consider Wannier interpolation in large systems (such as nanostructures) that are often sampled only at the zone center. We consider here a (5,5) carbon
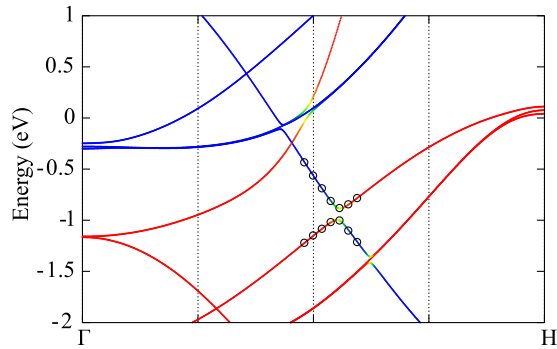
FIG. 27 (color online). Detail of the Wannier-interpolated relativistic band structure of ferromagnetic bcc Fe along Γ-H. The bands are color coded according to the expectation value of S_z: lighter for spin up and darker for spin down. The energies in eV are referred to the Fermi level. The vertical dashed lines indicate **k** points on the mesh used in the first-principles calculation for constructing the WFs. For comparison, points from a full *ab initio* calculation are shown as open circles. From Yates *et al.*, 2007.

nanotube, studied in a 100-atom supercell (i.e., 5 times the primitive unit cell) and with Γ-point sampling (Lee, Nardelli, and Marzari, 2005). The system is metallic, and the disentanglement procedure is used to generate well-localized WFs, resulting in either bond-centered combinations of sp^2 atomic orbitals or atom-centered p_z orbitals. The energy bands at any other **k** points are calculated by diagonalizing Eq. (98), noting that the size of the supercell has been chosen so that the Hamiltonian matrix elements on the right-hand side of this equation are non-negligible only for WFs up to neighboring supercells $\mathbf{R}^{(\pm)}$ on either side of $\mathbf{R} = \mathbf{0}$. Figure 28 shows as solid lines the interpolated bands, unfolded onto the 20-atom primitive cell. Even if with this sampling the system has a pseudogap of 2 eV, the metallic character of the bands is perfectly reproduced, and these are in excellent agreement
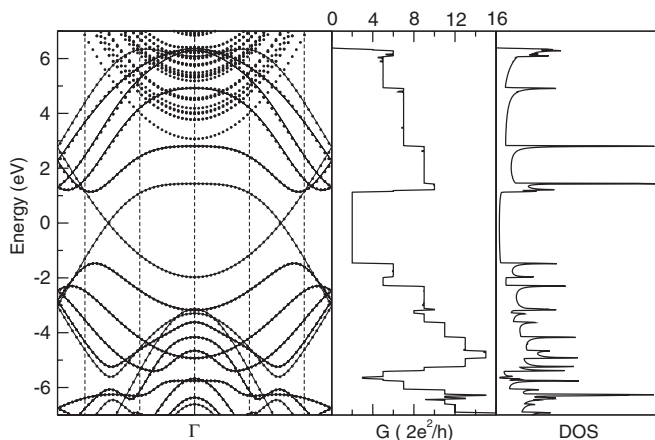

FIG. 28. Electronic properties of a (5,5) carbon nanotube calculated using WFs. Left panel: Band structure by Wannier interpolation (solid lines), or from a full diagonalization in a plane-wave basis set (circles). The vertical dashed lines indicate the five **k** points corresponding to the Γ point in a 100-atom supercell. The middle and right panels show the Wannier-based calculation of the quantum conductance and the density of states, with a perfect match of steps and peaks with respect to the exact band structure. From Lee, Nardelli, and Marzari, 2005.

with the bands calculated directly on the primitive cell by direct diagonalization of the Kohn-Sham Hamiltonian in the full plane-wave basis set (open circles). The vertical dashed lines indicate the equivalent first-principles mesh obtained by unfolding the Γ point.[17]

3. *GW* quasiparticle bands

In the two examples above the WFs were generated from Kohn-Sham Bloch functions, and the eigenvalues used in Eq. (101) were the corresponding Kohn-Sham eigenvalues. Many of the deficiencies of the Kohn-Sham energy bands, such as the underestimation of the energy gaps of insulators and semiconductors, can be corrected using many-body perturbation theory in the form of the *GW* approximation [for a review, see Aryasetiawan and Gunnarsson (1998)].

One practical difficulty in generating *GW* band-structure plots is that the evaluation of the QP corrections to the eigenenergies along different symmetry lines in the BZ is computationally very demanding. At variance with the DFT formalism, where the eigenenergies at an arbitrary **k** can be found starting from the self-consistent charge density, the evaluation of the QP corrections at a given **k** requires a knowledge of the Kohn-Sham eigenenergies and wave functions on a homogeneous grid of points containing the wave vector of interest. What is often done instead is to perform the *GW* calculation at selected **k** points only, and then deduce a "scissors correction," i.e., a constant shift to be applied to the conduction-band Kohn-Sham eigenvalues elsewhere in the Brillouin zone.

As mentioned in Sec. II.J, Hamann and Vanderbilt (2009) proposed using Wannier interpolation to determine the *GW* QP bands very efficiently and accurately at arbitrary points in the BZ. The Wannierization and interpolation procedures are identical to the DFT case. The only difference is that the starting eigenenergies and overlap matrices over the uniform first-principles mesh are now calculated at the *GW* level. (In the simplest G_0W_0 approximation, where only the eigenenergies, not the eigenfunctions, are corrected, the Wannierization is done at the DFT level, and the resulting transformation matrices are then applied to the corrected QP eigenenergies.)

Figure 29 shows a comparison between the interpolated *GW* (dashed lines) and DFT-LDA (solid lines) bands of $SrTiO_3$ (Hamann and Vanderbilt, 2009). Note that the dashed lines pass through the open circles at the symmetry points, which denote exact (noninterpolated) *GW* results.

Among the recent applications of the *GW* + Wannier method, we mention the study of the energy bands of zircon and hafnon (Shaltaf *et al.*, 2009), and a detailed comparative study between the DFT-LDA, scissors-shifted, and QP G_0W_0 bands of Si and Ge nanowires (Peelaers *et al.*, 2011). In the latter study they found that the simple scissors correction to the DFT-LDA bands is accurate near the Γ point only, and only for bands close to the highest valence and lowest

---

[17]When Γ sampling is used, special care should be used in calculating matrix elements between WFs, since the center of a periodic image of, e.g., the ket could be closer to the bra that the actual state considered. Similar considerations apply for transport calculations and might require calculation of the matrix elements in real space (Lee, 2006).
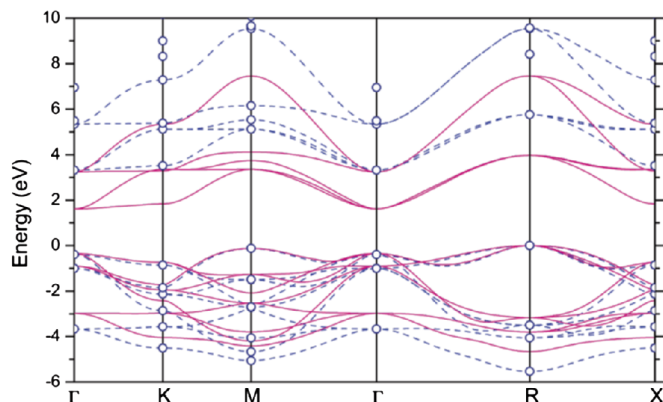
FIG. 29 (color online). Wannier-interpolated upper valence and lower conduction bands of $SrTiO_3$ from local-density approximation (solid lines) and *GW* (dashed line) calculations. The open circles at the symmetry points denote the exact *GW* results taken directly from the first-principles calculation. From Hamann and Vanderbilt, 2009.

conduction band. Kioupakis *et al.* (2010) used the method to elucidate the mechanisms responsible for free-carrier absorption in GaN and in the $In_{0.25}Ga_{0.75}N$ alloy. Yazyev *et al.* (2012) investigated the quasiparticle effects on the band structure of the topological insulators Bi_2Se_3 and Bi_2Te_3, and Åberg, Sadigh, and Erhart (2012) studied in detail the electronic structure of $LaBr_3$.

4. Surface bands of topological insulators

TIs were briefly discussed in Sec. V.C.4 [see Hasan and Kane (2010) and Hasan and Moore (2011) for useful reviews]. Here we focus on the nonmagnetic variety, the Z_2-odd TIs. The recent flurry of activity on this class of materials has been sustained in part by the experimental confirmation of the Z_2-odd character of certain quantum-well structures and of a rapidly increasing number of bulk crystals.

In the case of 3D TIs, the clearest experimental signature of the Z_2-odd character is at present provided by ARPES measurements of the surface electron bands. If time-reversal symmetry is preserved at the surface, Z_2-odd materials possess topologically protected surface states which straddle the bulk gap, crossing the Fermi level an odd number of times. These surface states are doubly degenerate at the time-reversal-invariant momenta of the surface BZ, and in the vicinity thereof they disperse linearly, forming Dirac cones.

First-principles calculations of the surface states for known and candidate TI materials are obviously of great interest for comparing with ARPES measurements. While it is possible to carry out a direct first-principles calculation for a thick slab in order to study the topologically protected surface states, as done by Yazyev, Moore, and Louie (2010), such an approach is computationally expensive. Zhang *et al.* (2010) used a simplified Wannier-based approach which succeeds in capturing the essential features of the topological surface states at a greatly reduced computational cost. Their procedure is as follows. First, an inexpensive calculation is done for the bulk crystal without spin-orbit interaction. Next, disentangled WFs spanning the upper valence and low-lying conduction bands are generated, and the corresponding TB Hamiltonian

matrix is constructed. The TB Hamiltonian is then augmented with spin-orbit couplings $\lambda \mathbf{L} \cdot \mathbf{S}$, where λ is taken from atomic data; this is possible because the WFs have been constructed so as to have specified *p*-like characters. The augmented TB parameters are then used to construct sufficiently thick freestanding "tight-binding slabs" by a simple truncation of the effective TB model, and the dispersion relation is efficiently calculated by interpolation as a function of the wave vector $\mathbf{k}_\parallel$ in the surface BZ.

It should be noted that this approach contains no surface-specific information, being based exclusively on the bulk WFs. Even if its accuracy is questionable, however, this method is useful for illustrating the "topologically protected" surface states that arise as a manifestation of the bulk electronic structure (Hasan and Kane, 2010).

Instead of applying the naive truncation, it is possible to refine the procedure so as to incorporate the changes to the TB parameters near the surface. To do so, the bulk calculation must now be complemented by a calculation on a thin slab, again followed by Wannierization. Upon aligning the on-site energies in the interior of this slab to the bulk values, the changes to the TB parameters near the surface can be inferred. However, H.-J. Zhang *et al.* (2011) found that the topological surface states are essentially the same with and without this surface correction.

The truncated-slab approach was applied by Zhang *et al.* (2010) to the stoichiometric three-dimensional TIs Sb_2Te_3, Bi_2Se_3, and Bi_2Te_3. The calculations on Bi_2Se_3 revealed the existence of a single Dirac cone at the $\bar{\Gamma}$ point as shown in Fig. 30, in agreement with ARPES measurements (Xia *et al.*, 2009).

An alternative strategy for calculating the surface bands was used earlier also by Zhang, Liu, Qi, Dai *et al.*, (2009). Instead of explicitly diagonalizing the Wannier-based Hamiltonian $H(\mathbf{k}_\parallel)$ of a thick slab, the Green's function for the semi-infinite crystal as a function of the atomic plane is obtained via iterative methods (López Sancho, López Sancho, and Rubio, 1984; López Sancho *et al.*, 1985), using the approach of Lee, Nardelli, and Marzari (2005). Here the
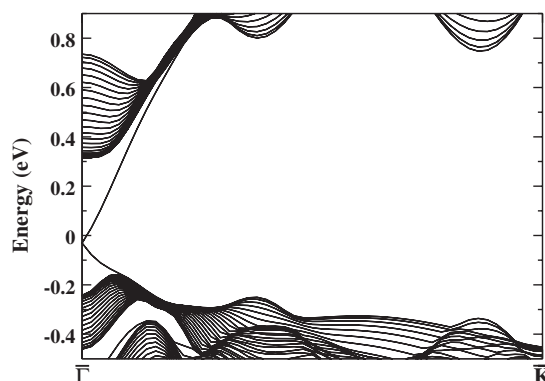
FIG. 30. Wannier-interpolated energy bands of a freestanding (111)-oriented slab containing 25 quintuple layers of Bi_2Se_3 plotted along the $\bar{\Gamma}$-$\bar{K}$ line in the surface Brillouin zone. A pair of topologically protected surface bands can be seen emerging from the dense set of projected valence and conduction bulklike bands and crossing at the time-reversal-invariant point $\bar{\Gamma}$. Adapted from Zhang *et al.*, 2010.

localized Wannier representation is used to break down the semi-infinite crystal into a stack of "principal layers" consisting of a number of atomic planes, such that only nearest-neighbor interactions between principal layers exist (see Sec. VII for more details).

Within each principal layer one forms, starting from the fully localized WFs, a set of hybrid WFs which are extended (Bloch-like) along the surface but remain localized (Wannier-like) in the surface-normal direction (see Secs. II.H and V.B.2). This is achieved by carrying out a partial Bloch sum over the in-plane lattice vectors,

$$|l, n\mathbf{k}_\parallel\rangle = \sum_{\mathbf{R}_\parallel} e^{i\mathbf{k}_\parallel \cdot \mathbf{R}_\parallel} |\mathbf{R}n\rangle, \qquad (103)$$

where l labels the principal layer, $\mathbf{k}_\parallel$ is the in-plane wave vector, and $\mathbf{R}_\parallel$ is the in-plane component of $\mathbf{R}$. The matrix elements of the Green's function in this basis are

$$G_{ll'}^{nn'}(\mathbf{k}_\parallel, \epsilon) = \langle \mathbf{k}_\parallel ln|(\epsilon - H)^{-1}|\mathbf{k}_\parallel l'n'\rangle. \qquad (104)$$

The nearest-neighbor coupling between principal layers means that for each $\mathbf{k}_\parallel$ the Hamiltonian has a block tridiagonal form (the dependence of the Hamiltonian matrix on $\mathbf{k}_\parallel$ is given by the usual Fourier sum expression). This feature can be exploited to calculate the diagonal elements of the Green's function matrix very efficiently using iterative schemes (López Sancho, López Sancho, and Rubio, 1984; López Sancho *et al.*, 1985).[18] From these, the density of states (DOS) projected onto a given atomic plane $\mathcal{P}$ can be obtained (Grosso and Parravicini, 2000) as

$$N_l^{\mathcal{P}}(\mathbf{k}_\parallel, \epsilon) = -\frac{1}{\pi} \mathrm{Im} \sum_{n \in \mathcal{P}} G_{ll}^{nn}(\mathbf{k}_\parallel, \epsilon + i\eta), \qquad (105)$$

where the sum over n is restricted to the orbitals ascribed to the chosen plane and η is a positive infinitesimal.

The projection of the DOS onto the outermost atomic plane is shown in Fig. 31 as a function of energy ϵ and momentum $\mathbf{k}_\parallel$ for the (111) surface of Sb_2Te_3. The same method has been used to find the dispersion of the surface bands in the TI alloy $Bi_{1-x}Sb_x$ (Zhang, Liu, Qi, Deng *et al.*, 2009) and in ternary compounds with a honeycomb lattice (H.-J. Zhang *et al.*, 2011).

B. Band derivatives

The first and second derivatives of the energy eigenvalues with respect to $\mathbf{k}$ (band velocities and inverse effective masses) appear in a variety of contexts, such as the calculation of transport coefficients (Ashcroft and Mermin, 1976; Grosso and Parravicini, 2000). There is therefore considerable interest in developing simple and accurate procedures for extracting these parameters from a first-principles band-structure calculation.

A direct numerical differentiation of the eigenenergies calculated on a grid is cumbersome and becomes unreliable

[18]A pedagogical discussion, where a continued-fractions expansion is used to evaluate the Green's function of a semi-infinite linear chain with nearest-neighbor interactions, is given by Grosso and Parravicini (2000).
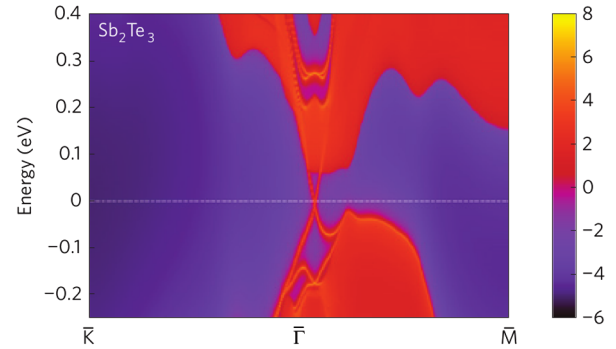
FIG. 31 (color online). Surface density of states (DOS) of a semi-infinite crystal of Sb_2Te_3 terminated with a (111) surface. Lighter (warmer) colors represent a higher SDOS. The surface states can be seen around $\bar{\Gamma}$ as lines crossing at $E = 0$. From Zhang, Liu, Qi, Dai *et al.*, 2009.

near band crossings. It is also very expensive if a Brillouin-zone integration is to be carried out, as in transport calculations. A number of efficient interpolation schemes, such as the method implemented in the BOLTZTRAP package (Madsen and Singh, 2006), have been developed for this purpose, but they are still prone to numerical instabilities near band degeneracies (Uehara and Tse, 2000). Such instabilities can be avoided by using a tight-binding parametrization to fit the first-principles band structure (Schulz, Allen, and Trivedi, 1992; Mazin, Papaconstantopoulos, and Singh, 2000). As shown by Graf and Vogl (1992) and Boykin (1995), both the first and second derivatives are easily computed within tight-binding methods, even in the presence of band degeneracies, and the same can be done in a first-principles context using WFs.

We illustrate the procedure by calculating the band gradient away from points of degeneracy; the treatment of degeneracies and second derivatives is given by Yates *et al.* (2007). The first step is to analytically take the derivative $\partial_\alpha = \partial/\partial k_\alpha$ of Eq. (98),

$$H_{\mathbf{k},\alpha}^{\mathrm{W}} \equiv \partial_\alpha H_{\mathbf{k}}^{\mathrm{W}} = \sum_{\mathbf{R}} e^{i\mathbf{k} \cdot \mathbf{R}} iR_\alpha \langle \mathbf{0}|H|\mathbf{R}\rangle. \qquad (106)$$

The actual band gradients are given by the diagonal elements of the rotated matrix,

$$\partial_\alpha \bar{\epsilon}_{n\mathbf{k}} = [U_{\mathbf{k}}^\dagger H_{\mathbf{k},\alpha}^{\mathrm{W}} U_{\mathbf{k}}]_{nn}, \qquad (107)$$

where $U_{\mathbf{k}}$ is the same unitary matrix as in Eq. (99).

It is instructive to view the columns of $U_{\mathbf{k}}$ as orthonormal state vectors in the J-dimensional tight-binding space defined by the WFs. According to Eq. (99) the nth column vector, which we denote by $\|\phi_{n\mathbf{k}}\rangle\rangle$, satisfies the eigenvalue equation $H_{\mathbf{k}}^{\mathrm{W}} \|\phi_{n\mathbf{k}}\rangle\rangle = \bar{\epsilon}_{n\mathbf{k}} \|\phi_{n\mathbf{k}}\rangle\rangle$. Armed with this insight, we now recognize in Eq. (107) the Hellmann-Feynman result $\partial_\alpha \bar{\epsilon}_{n\mathbf{k}} = \langle\langle \phi_{n\mathbf{k}} \| \partial_\alpha H_{\mathbf{k}}^{\mathrm{W}} \| \phi_{n\mathbf{k}}\rangle\rangle$.

Within the semiclassical theory of transport, the electrical and thermal conductivities of metals and doped semiconductors can be calculated from a knowledge of the band derivatives and relaxation times $\tau_{n\mathbf{k}}$ on the Fermi surface. An example is the low-field Hall conductivity σ_{xy} of nonmagnetic cubic metals, which in the constant relaxation-time approximation is independent of τ and takes the form of a

Fermi surface integral containing the first and second band derivatives (Hurd, 1972).

Previous first-principles calculations of σ_{xy} using various interpolation schemes encountered difficulties for materials such as Pd, where band crossings occur at the Fermi level (Uehara and Tse, 2000). A Wannier-based calculation free from such numerical instabilities was carried out by Yates *et al.* (2007), who obtained carefully converged values for σ_{xy} in Pd and other cubic metals.

A more general formalism to calculate the electrical conductivity tensor in the presence of a uniform magnetic field involves integrating the equations of motion of a wave packet under the field to find its trajectory on the Fermi surface (Ashcroft and Mermin, 1976). A numerical implementation of this approach starting from the Wannier-interpolated first-principles bands was carried out by Liu, Zhang, and Yao (2009). This formalism is not restricted to cubic crystals, and they used it to calculate the Hall conductivity of hcp Mg (Liu, Zhang, and Yao, 2009) and the magnetoconductivity of MgB_2 (Yang *et al.*, 2008).

Wannier interpolation has also been used to determine the Seebeck coefficient in hole-doped $LaRhO_3$ and $CuRhO_2$ (Usui, Arita, and Kuroki, 2009), in electron-doped $SrTiO_3$ (Usui, Shibata, and Kuroki, 2010), in SiGe nanowires (Shelley and Mostofi, 2011), and in ternary skutterudites (Volja *et al.*, 2012).

C. Berry curvature and anomalous Hall conductivity

The velocity matrix elements between Bloch eigenstates take the form (Blount, 1962)

$$\langle \psi_{n\mathbf{k}}|\hbar v_\alpha|\psi_{m\mathbf{k}}\rangle = \delta_{nm}\partial_\alpha \epsilon_{n\mathbf{k}} - i(\epsilon_{m\mathbf{k}} - \epsilon_{n\mathbf{k}})[A_{\mathbf{k},\alpha}]_{nm}, \quad (108)$$

where

$$[A_{\mathbf{k},\alpha}]_{nm} = i\langle u_{n\mathbf{k}}|\partial_\alpha u_{m\mathbf{k}}\rangle \quad (109)$$

is the matrix generalization of the Berry connection of Eq. (95).

In the examples discussed in Sec. VI.B the static transport coefficients could be calculated from the first term in Eq. (108), the intraband velocity. The second term describes vertical interband transitions, which dominate the optical spectrum of crystals over a wide frequency range. Interestingly, under certain conditions, *virtual* interband transitions also contribute to the dc Hall conductivity. This so-called *anomalous Hall effect* occurs in ferromagnets from the combination of exchange splitting and spin-orbit interaction. For a recent review, see Nagaosa *et al.* (2010).

In the same way that WFs proved helpful for evaluating $\partial_{\mathbf{k}}\epsilon_{n\mathbf{k}}$, they can be useful for calculating quantities containing $\mathbf{k}$ derivatives of the cell-periodic Bloch states, such as the Berry connection of Eq. (109). A number of properties are naturally expressed in this form. In addition to the interband optical conductivity and the AHC, other examples include the electric polarization (see Sec. V.A) as well as the orbital magnetization and magnetoelectric coupling (see Sec. V.C).

We focus now on the Berry curvature $\mathcal{F}_{n\mathbf{k}}$ [Eq. (96)], a quantity with profound effects on the dynamics of electrons in crystals (Xiao, Chang, and Niu, 2010). $\mathcal{F}_{n\mathbf{k}}$ can be nonzero if

either spatial inversion or time-reversal symmetries are broken in the crystal, and when present acts as a kind of "magnetic field" in $\mathbf{k}$ space, with the Berry connection $\mathbf{A}_{n\mathbf{k}}$ playing the role of the vector potential. This effective field gives rise to a Hall effect in ferromagnets even in the absence of an actual applied $\mathbf{B}$ field (hence the name anomalous). The AHC is given by[19]

$$\sigma_{\alpha\beta}^{\text{AH}} = -\frac{e^2}{\hbar}\int_{\text{BZ}}\frac{d\mathbf{k}}{(2\pi)^3}\mathcal{F}_{\mathbf{k},\alpha\beta}^{\text{tot}}, \quad (110)$$

where $\mathcal{F}_{\mathbf{k},\alpha\beta}^{\text{tot}} = \sum_n f_{n\mathbf{k}}\mathcal{F}_{n\mathbf{k},\alpha\beta}$ ($f_{n\mathbf{k}}$ is the Fermi-Dirac distribution function), and we have rewritten the pseudovector $\mathcal{F}_{n\mathbf{k}}$ as an antisymmetric tensor.

The interband character of the intrinsic AHC can be seen by using $\mathbf{k}\cdot\mathbf{p}$ perturbation theory to write the $\mathbf{k}$ derivatives in Eq. (96), leading to the "sum-over-states" formula

$$\mathcal{F}_{\alpha\beta}^{\text{tot}} = i\sum_{n,m}(f_n - f_m)\frac{\langle\psi_n|\hbar v_\alpha|\psi_m\rangle\langle\psi_m|\hbar v_\beta|\psi_n\rangle}{(\epsilon_m - \epsilon_n)^2}. \quad (111)$$

The AHC of bcc Fe and $SrRuO_3$ was evaluated from the previous two equations by Fang *et al.* (2003) and Yao *et al.* (2004), respectively. These pioneering first-principles calculations revealed that in ferromagnetic metals the Berry curvature displays strong and rapid variations in $\mathbf{k}$ space (see Fig. 32). As a result, an ultradense BZ mesh containing millions of $\mathbf{k}$ points is often needed in order to converge the calculation. This is the kind of situation where the use of Wannier interpolation can be most beneficial.

The strategy for interpolating the Berry curvature is similar to that used in Sec. VI.B for the band gradient. One first evaluates certain objects in the Wannier gauge using Bloch sums and then transforms to the Hamiltonian gauge. Because the gauge transformation mixes the bands, it is convenient to introduce a generalization of Eq. (96) having two band indices instead of one. To this end we start from Eq. (109) and define the matrices

$$\mathcal{F}_{\alpha\beta} = \partial_\alpha A_\beta - \partial_\beta A_\alpha = i\langle\partial_\alpha u|\partial_\beta u\rangle - i\langle\partial_\beta u|\partial_\alpha u\rangle, \quad (112)$$

where every object in this expression should consistently carry either an H or W label. Provided that the chosen WFs correctly span all occupied states, the integrand of Eq. (110) can now be expressed as $\mathcal{F}_{\alpha\beta}^{\text{tot}} = \sum_{n=1}^{J} f_n \mathcal{F}_{\alpha\beta,nn}^{\text{H}}$.

A useful expression for $\mathcal{F}_{\alpha\beta}^{\text{H}}$ can be obtained with the help of the gauge-transformation law for the Bloch states, $|u_{\mathbf{k}}^{\text{H}}\rangle = |u_{\mathbf{k}}^{\text{W}}\rangle U_{\mathbf{k}}$ [Eq. (100)]. Differentiating both sides with respect to k_α and then inserting into Eq. (112) yields, after a few manipulations,

$$\mathcal{F}_{\alpha\beta}^{\text{H}} = \bar{\mathcal{F}}_{\alpha\beta} - [D_\alpha, \bar{A}_\beta] + [D_\beta, \bar{A}_\alpha] - i[D_\alpha, D_\beta], \quad (113)$$

where $D_\alpha = U^\dagger\partial_\alpha U$, and $\bar{A}_\alpha$, $\bar{\mathcal{F}}_{\alpha\beta}$ are related to the connection and curvature matrices in the Wannier gauge through

---

[19]Equation (110) gives the so-called "intrinsic" contribution to the AHC, while the measured effect also contains "extrinsic" contributions associated with scattering from impurities (Nagaosa *et al.*, 2010).
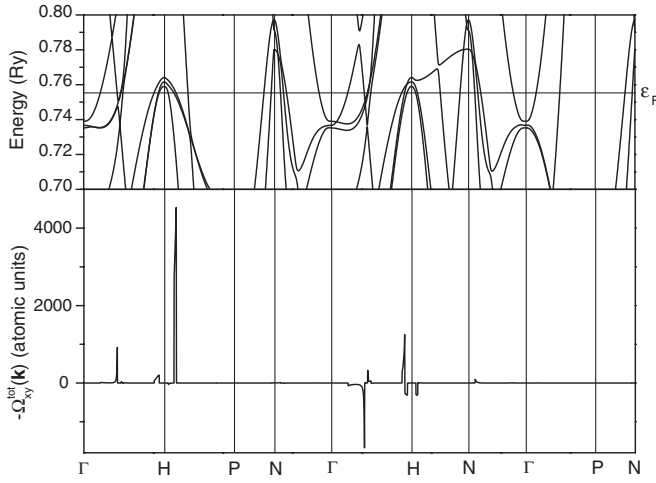
FIG. 32.   Energy bands and **k**-space Berry curvature in bcc Fe, with the ferromagnetic moment along $\hat{\mathbf{z}}$. Upper panel: Band structure near the Fermi level. Lower panel: Berry curvature summed over the occupied bands [Eq. (111)]. The sharp spikes occur when two spin-orbit-coupled bands are separated by a small energy across the Fermi level, producing a resonance enhancement. The symbol Ω here corresponds to $\mathcal{F}$ in the main text. Adapted from Yao *et al.*, 2004.

the definition $\bar{O}_{\mathbf{k}} = U_{\mathbf{k}}^{\dagger} O_{\mathbf{k}}^{\mathrm{W}} U_{\mathbf{k}}$. Using the band-diagonal elements of Eq. (113) in the expression for $\mathcal{F}_{\alpha\beta}^{\mathrm{tot}}$ eventually leads to

$$\mathcal{F}_{\alpha\beta}^{\mathrm{tot}} = \sum_n^J f_n \bar{\mathcal{F}}_{\alpha\beta,nn} + \sum_{mn}^J (f_m - f_n)(D_{\alpha,nm}\bar{A}_{\beta,mn}$$
$$- D_{\beta,nm}\bar{A}_{\alpha,mn} + iD_{\alpha,nm}D_{\beta,mn}). \quad (114)$$

This is the desired expression, which in the Wannier interpolation scheme takes the place of the sum-over-states formula. In contrast to Eq. (111), note that the summations over bands now run over the small set of Wannier-projected bands. [Alternatively, it is possible to recast Eq. (114) in a manifestly gauge-invariant form such that the trace can be carried out directly in the Wannier gauge; this formulation was used by Lopez *et al.* (2012) to compute both the AHC and the orbital magnetization of ferromagnets.]

The basic ingredients going into Eq. (114) are the Wannier matrix elements of the Hamiltonian and of the position operator. From a knowledge of $\langle \mathbf{0}|H|\mathbf{R}\rangle$ the energy eigenvalues and occupation factors, as well as the matrices U and D_α, can be found using band-structure interpolation (see Sec. VI.A). The information about A_α^{W} and $\mathcal{F}_{\alpha\beta}^{\mathrm{W}}$ is instead encoded in the matrix elements $\langle \mathbf{0}|\mathbf{r}|\mathbf{R}\rangle$, as can be seen by inverting Eq. (23),

$$A_\alpha^{\mathrm{W}} = \sum_{\mathbf{R}} e^{i\mathbf{k}\cdot\mathbf{R}} \langle \mathbf{0}|r_\alpha|\mathbf{R}\rangle. \quad (115)$$

As for $\mathcal{F}_{\alpha\beta}^{\mathrm{W}}$, according to Eq. (112) it is given by the curl of this expression, which can be taken analytically.

The strategy outlined above was demonstrated by Wang *et al.* (2006) in calculating the AHC of bcc Fe, using the spinor WFs of Sec. VI.A.1. Both the **k**-space distribution of

the Berry curvature and the integrated AHC were found to be in excellent agreement with the sum-over-states calculation of Yao *et al.* (2004).

Table I lists the AHC of the ferromagnetic transition-metal elements, calculated with the magnetization along the respective easy axes. The magnetic anisotropy of the AHC was investigated by Roman, Mokrousov, and Souza (2009). While the AHC of the cubic metals Fe and Ni is fairly isotropic, that of hcp Co was found to decrease by a factor of 4 as the magnetization is rotated from the c axis to the basal plane. The Wannier method has also been used to calculate the AHC in FePt and FePd ordered alloys (Seeman *et al.*, 2009; H. Zhang *et al.*, 2011), and the spin-Hall conductivity in a number of metals (Freimuth, Blügel, and Mokrousov, 2010).

As mentioned, for certain applications the Berry connection matrix [Eq. (109)] is the object of direct interest. The interpolation procedure described above can be directly applied to the off-diagonal elements describing vertical interband transitions, and the magnetic circular dichroism spectrum of bcc Fe has been determined in this way (Yates *et al.*, 2007).

The treatment of the diagonal elements of the Berry connection matrix is more subtle, as they are locally gauge dependent. Nevertheless, the Berry phase obtained by integrating over a closed loop in **k** space, $\varphi_n = \oint \mathbf{A}_{n\mathbf{k}} \cdot d\mathbf{l}$, is gauge invariant (Xiao, Chang, and Niu, 2010). Recalling that $\mathcal{F}_{n\mathbf{k}} = \nabla_{\mathbf{k}} \times \mathbf{A}_{n\mathbf{k}}$ [Eq. (96)] and using Stokes' theorem, Eq. (110) for the AHC can be recast in terms of the Berry phases of Fermi loops on planar slices of the Fermi surface. This approach was implemented by Wang *et al.* (2007), using Wannier interpolation to sample efficiently the orbits with the very high density required near band crossings. Table I lists values for the AHC calculated using both the Berry curvature ("Fermi sea") and Berry-phase ("Fermi surface") approaches.

It should be possible to devise similar Wannier interpolation strategies for other properties requiring dense BZ sampling, such as the magnetic shielding tensors of metals (d'Avezac, Marzari, and Mauri, 2007). In the following we discuss electron-phonon coupling, for which Wannier-based methods have already proven to be of great utility.

TABLE I.   Anomalous Hall conductivity in S/cm of the ferromagnetic transition metals, calculated from first principles with the magnetization along the respective easy axes. The first two rows show values obtained using the Wannier interpolation scheme either to integrate the Berry curvature over the Fermi sea or to evaluate the Berry phases of planar loops around the Fermi surface (see main text). Results obtained using the sum-over-states formula, Eq. (111), are included for comparison, as well as representative experimental values. Adapted from Wang *et al.* (2007).

	bcc Fe	fcc Ni	hcp Co
Berry curvature	753	−2203	477
Berry phase	750	−2275	478
Sum over states	751[a]	−2073[b]	492[b]
Experiment	1032	−646	480

[a]Yao *et al.* (2004).
[b]Y. Yao (private communication).

D. Electron-phonon coupling

The electron-phonon interaction (Grimvall, 1981) plays a key role in a number of phenomena, from superconductivity to the resistivity of metals and the temperature dependence of the optical spectra of semiconductors. The matrix element for scattering an electron from state $\psi_{n\mathbf{k}}$ to state $\psi_{m,\mathbf{k}+\mathbf{q}}$ while absorbing a phonon $\mathbf{q}\nu$ is proportional to the electron-phonon vertex

$$g_{\nu,mn}(\mathbf{k},\mathbf{q}) = \langle \psi_{m,\mathbf{k}+\mathbf{q}} | \partial_{\mathbf{q}\nu} V | \psi_{n\mathbf{k}} \rangle. \tag{116}$$

Here $\partial_{\mathbf{q}\nu} V$ is the derivative of the self-consistent potential with respect to the amplitude of the phonon with branch index ν and momentum $\mathbf{q}$. Evaluating this vertex is a key task for a first-principles treatment of electron-phonon couplings.

State-of-the-art calculations using first-principles linear-response techniques (Baroni *et al.*, 2001) have been successfully applied to a number of problems, starting with the works of Savrasov, Savrasov, and Andersen (1994) and Mauri *et al.* (1996), who used, respectively, the LMTO and plane-wave pseudopotential methods. The cost of evaluating Eq. (116) from first principles over a large number of $(\mathbf{k},\mathbf{q})$ points is quite high, however, and this has placed a serious limitation on the scope and accuracy of first-principles techniques for electron-phonon problems.

The similarity between the Wannier interpolation of energy bands and the Fourier interpolation of phonon dispersions was already noted. It suggests the possibility of interpolating the electron-phonon vertex in both the electron and the phonon momenta, once Eq. (116) has been calculated on a relatively coarse uniform $(\mathbf{k},\mathbf{q})$ mesh. Different electron-phonon interpolation schemes have been put forth in the literature (Giustino *et al.*, 2007; Eiguren and Ambrosch-Draxl, 2008; Calandra, Profeta, and Mauri, 2010). In the following we describe the approach first developed by Giustino, Cohen, and Louie (2007) and implemented in the software package EPW (Noffsinger *et al.*, 2010). To begin, we set the notation for lattice dynamics (Maradudin and Vosko, 1968). We write the instantaneous nuclear positions as $\mathbf{R} + \boldsymbol{\tau}_s + \mathbf{u}_{\mathbf{R}s}(t)$, where $\mathbf{R}$ is the lattice vector, $\boldsymbol{\tau}_s$ is the equilibrium intracell coordinate of ion $s = 1, \ldots, S$, and $\mathbf{u}_{\mathbf{R}s}(t)$ denotes the instantaneous displacement. The normal modes of vibration take the form

$$\mathbf{u}_{\mathbf{R}s}^{\mathbf{q}\nu}(t) = \mathbf{u}_s^{\mathbf{q}\nu} e^{i(\mathbf{q}\cdot\mathbf{R} - \omega_{\mathbf{q}\nu}t)}. \tag{117}$$

The eigenfrequencies $\omega_{\mathbf{q}\nu}$ and mode amplitudes $\mathbf{u}_s^{\mathbf{q}\nu}$ are obtained by diagonalizing the dynamical matrix $[D_{\mathbf{q}}^{\mathrm{ph}}]_{st}^{\alpha\beta}$, where α and β denote spatial directions. It is expedient to introduce composite indices $\mu = (s,\alpha)$ and $\nu = (t,\beta)$, and write $D_{\mathbf{q},\mu\nu}^{\mathrm{ph}}$ for the dynamical matrix. With this notation, the eigenvalue equation becomes

$$[e_{\mathbf{q}}^{\dagger} D_{\mathbf{q}}^{\mathrm{ph}} e_{\mathbf{q}}]_{\mu\nu} = \delta_{\mu\nu} \omega_{\mathbf{q}\nu}^2, \tag{118}$$

where $e_{\mathbf{q}}$ is a $3S \times 3S$ unitary matrix. In analogy with the tight-binding eigenvectors $\| \phi_{n\mathbf{k}} \rangle\!\rangle$ of Sec. VI.B, we can view the columns of $e_{\mathbf{q},\mu\nu}$ as orthonormal phonon eigenvectors $\mathbf{e}_s^{\mathbf{q}\nu}$. They are related to the complex phonon amplitudes by $\mathbf{u}_s^{\mathbf{q}\nu} = (m_0/m_s)^{1/2} \mathbf{e}_s^{\mathbf{q}\nu}$ (m_0 is a reference mass), which we write in matrix form as $U_{\mathbf{q},\mu\nu}^{\mathrm{ph}}$.

Returning to the electron-phonon vertex, Eq. (116), we can now write explicitly the quantity $\partial_{\mathbf{q}\nu} V$ therein as

$$\partial_{\mathbf{q}\nu} V(\mathbf{r}) = \frac{\partial}{\partial\eta} V(\mathbf{r}; \{\mathbf{R} + \boldsymbol{\tau}_s + \eta \mathbf{u}_{\mathbf{R}s}^{\mathbf{q}\nu}\})$$
$$= \sum_{\mathbf{R},\mu} e^{i\mathbf{q}\cdot\mathbf{R}} \partial_{\mathbf{R}\mu} V(\mathbf{r}) U_{\mathbf{q},\mu\nu}^{\mathrm{ph}}, \tag{119}$$

where $\partial_{\mathbf{R}\mu} V(\mathbf{r})$ is the derivative of the self-consistent potential with respect to $u_{\mathbf{R}s,\alpha}$. As discussed in Sec. VIII, it is possible to view these single-atom displacements as maximally localized "lattice Wannier functions" (LWFs). With this interpretation in mind we define the Wannier-gauge counterpart of $\partial_{\mathbf{q}\nu} V(\mathbf{r})$ as

$$\partial_{\mathbf{q}\mu}^{\mathrm{W}} V(\mathbf{r}) = \sum_{\mathbf{R}} e^{i\mathbf{q}\cdot\mathbf{R}} \partial_{\mathbf{R}\mu} V(\mathbf{r}), \tag{120}$$

related to the "eigenmode-gauge" quantity $\partial_{\mathbf{q}\nu} V(\mathbf{r})$ by

$$\partial_{\mathbf{q}\nu} V(\mathbf{r}) = \sum_{\mu} \partial_{\mathbf{q}\mu}^{\mathrm{W}} V(\mathbf{r}) U_{\mathbf{q},\mu\nu}^{\mathrm{ph}}. \tag{121}$$

Next we introduce the Wannier-gauge vertex $g_{\mu}^{\mathrm{W}}(\mathbf{k},\mathbf{q}) = \langle \psi_{\mathbf{k}+\mathbf{q}}^{\mathrm{W}} | \partial_{\mathbf{q}\mu}^{\mathrm{W}} V | \psi_{\mathbf{k}}^{\mathrm{W}} \rangle$, which can be readily interpolated onto an arbitrary point $(\mathbf{k}',\mathbf{q}')$ using Eqs. (97) and (120),

$$g_{\mu}^{\mathrm{W}}(\mathbf{k}',\mathbf{q}') = \sum_{\mathbf{R}_e,\mathbf{R}_p} e^{i(\mathbf{k}'\cdot\mathbf{R}_e + \mathbf{q}'\cdot\mathbf{R}_p)} \langle \mathbf{0}_e | \partial_{\mathbf{R}_p\mu} V | \mathbf{R}_e \rangle, \tag{122}$$

where the subscripts e and p denote electron and phonon, respectively. The object $\langle \mathbf{0}_e | \partial_{\mathbf{R}_p\mu} V | \mathbf{R}_e \rangle$, the electron-phonon vertex in the Wannier representation, is depicted schematically in Fig. 33. Its localization in real space ensures that Eq. (122) smoothly interpolates g^{W} in the electron and phonon momenta. Finally, we transform the interpolated vertex back to the Hamiltonian and eigenmode gauge,

$$g_{\nu}^{\mathrm{H}}(\mathbf{k}',\mathbf{q}') = \langle \psi_{\mathbf{k}'+\mathbf{q}'}^{\mathrm{H}} | \partial_{\mathbf{q}'\nu} V | \psi_{\mathbf{k}'}^{\mathrm{H}} \rangle$$
$$= U_{\mathbf{k}'+\mathbf{q}'}^{\dagger} \left[\sum_{\mu} g_{\mu}^{\mathrm{W}}(\mathbf{k}',\mathbf{q}') U_{\mathbf{q}',\mu\nu}^{\mathrm{ph}} \right] U_{\mathbf{k}'}, \tag{123}$$

where we used Eqs. (100) and (121).

Once the matrix elements $\langle \mathbf{0}_e | \partial_{\mathbf{R}_p\mu} V | \mathbf{R}_e \rangle$ are known, the electron-phonon vertex can be evaluated at arbitrary $(\mathbf{k}',\mathbf{q}')$ from the previous two equations. The procedure for evaluating those matrix elements is similar to that leading up to Eq. (101) for $\langle \mathbf{0} | H | \mathbf{R} \rangle$: invert Eq. (122) over the first-principles mesh and then use Eqs. (102) and (121).

The above interpolation scheme has been applied to a number of problems, including the estimation of T_c in superconductors (Giustino *et al.*, 2007; Noffsinger *et al.*, 2008, 2009), the phonon renormalization of energy bands near the Fermi level in graphene (Park *et al.*, 2007) and copper oxide superconductors (Giustino, Cohen, and Louie, 2008); the phonon renormalization of the band gap of diamond (Giustino, Louie, and Cohen, 2010), the vibrational lifetimes (Park *et al.*, 2008) and electron linewidths (Park *et al.*, 2009) arising from electron-phonon interactions in graphene, and the phonon-assisted optical absorption in silicon (Noffsinger *et al.*, 2012) (in this last application both the velocity and the electron-phonon matrix elements were treated by Wannier interpolation).
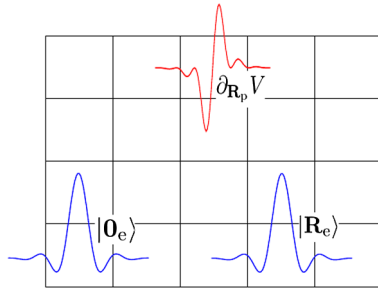
FIG. 33 (color online). Real-space representation of $\langle \mathbf{0}_e | \partial_{\mathbf{R}_p \mu} V | \mathbf{R}_e \rangle$, the electron-phonon vertex in the Wannier basis. The squares denote the crystal lattice, the bottom lines denote the electron Wannier functions $|\mathbf{0}_e\rangle$ and $|\mathbf{R}_e\rangle$, and the top line denotes the phonon perturbation in the lattice Wannier representation, $\partial_{\mathbf{R}_p \mu} V(\mathbf{r})$. Whenever two of these functions are centered on distant unit cells, the vertex becomes vanishingly small. From Giustino, Cohen, and Louie, 2007.

We mention in closing the work of Calandra, Profeta, and Mauri (2010), where the linear-response calculation of the deformation potential $\partial_{\mathbf{q}\nu} V$ is carried out taking into account nonadiabatic effects (that is, going beyond the usual approximation of static ionic displacements). Using the electron-phonon interpolation scheme of Giustino, Cohen, and Louie (2007) to perform the BZ integrations, and a Wannier interpolation of the dynamical matrix to capture Kohn anomalies, they found significant nonadiabatic corrections to the phonon frequencies and electron-phonon coupling matrix elements in MgB_2 and CaC_6.

VII. WANNIER FUNCTIONS AS BASIS FUNCTIONS

In Sec. VI, we described the use of Wannier functions as a compact tight-binding basis that represents a given set of energy bands exactly, and that can be used to calculate a variety of properties efficiently, and with very high accuracy. This is possible because (a) WFs and bands are related by unitary transformations, and (b) WFs are sufficiently localized that any resulting tight-binding representation may be truncated with little loss of accuracy. In this section, we review two further general approaches to the use of WFs as optimal and compact basis functions for electronic-structure calculations that exploit their localization and transferability.

The first category includes methods in which WFs are used to go up in the length scale of the simulations, using the results of electronic-structure calculations on small systems in order to construct accurate models of larger, often mesoscale, systems. Examples include using WFs to construct tight-binding Hamiltonians for large, structurally complex nanostructures (in particular, for studying quantum-transport properties), to parametrize semiempirical force fields, and to improve the system-size scaling of QMC and *GW* calculations, and the evaluation of exact-exchange integrals.

The second category includes methods in which WFs are used to identify and focus on a desired, physically relevant subspace of the electronic degrees of freedom that is singled out (downfolded) for further detailed analysis or special treatment with a more accurate level of electronic-structure theory, an approach that is particularly suited to the study of strongly correlated electron systems, such as materials containing transition metal, lanthanoid, or even actinoid ions.

A. WFs as a basis for large-scale calculations

Some of the first works on linear-scaling electronic-structure algorithms (Yang, 1991; Baroni and Giannozzi, 1992; Galli and Parrinello, 1992; Hierse and Stechel, 1994) highlighted the connection between locality in electronic structure, which underpins linear-scaling algorithms (see Sec. III.D), and the transferability of information across length scales. In particular, Hierse and Stechel (1994) considered explicitly two large systems A and B, different globally but which have a certain similar local feature, such as a particular chemical functionalization and its associated local environment, which we call C. They argued that the local electronic-structure information associated with C should be similar whether calculated from system A or system B and, therefore, that it should be possible to transfer this information from a calculation on A in order to construct a very good approximation to the electronic structure in the locality of feature C in system B. In this way, large computational savings could be made on the self-consistency cycle, enabling larger-scale calculations.

The units of electronic-structure information that Hierse and Stechel (1994) used were localized nonorthogonal orbitals, optimized in order to variationally minimize the total energy of the system. These orbitals are also referred to in the literature as support functions (Hernández and Gillan, 1995) or nonorthogonal generalized Wannier functions (Skylaris *et al.*, 2002).

1. WFs as electronic-structure building blocks

Since WFs encode chemically accurate, local (and thus transferable) information, they can act as building blocks to construct the electronic structure of very large-scale systems (Lee, Nardelli, and Marzari, 2005). In this approach the Hamiltonian matrix of a large nanostructure, for which a full, conventional DFT calculation would be intractable, is built using first-principles calculations performed on smaller, typically periodic fragments. The matrix elements in the basis of WFs that are obtained from the calculations on the fragments can be used to construct the entire Hamiltonian matrix of the desired system, with the size of the fragments a systematically controllable determinant of the accuracy of the method (Shelley *et al.*, 2011). Such an approach has been applied to complex systems containing tens of thousands of atoms (Lee and Marzari, 2006; Cantele *et al.*, 2009; Li and Marzari, 2011; Li, Poilvert, and Marzari, 2011; Shelley and Mostofi, 2011; Shelley *et al.*, 2011). In a similar vein, Berlijn, Volja, and Ku (2011) developed a method for building low-energy disordered Hamiltonians for crystals with point defects. The influence of a single impurity is extracted in the Wannier basis as the difference between two Hamiltonian matrices, with and without one impurity added to the crystal. This information is then used to assemble the Hamiltonian for a given distribution of point defects over a large supercell.

An issue that arises when combining matrix elements from more than one DFT calculation into a single tight-binding Hamiltonian is that a common reference potential must be

defined. For example, consider combining the results of a calculation on a perfect bulk material and one on the same material with an isolated structural defect. In the latter case, the diagonal (on-site) matrix elements $\langle w_n|H|w_n\rangle$ in the system with the defect should converge to the same value as those in the pristine system as one goes farther away from the location of the defect. With periodic boundary conditions, however, this is not guaranteed: the difference between the matrix elements in the respective calculations will, in general, tend to a nonzero constant, this being the difference in reference potential between the two calculations. In other words, the difference in value between the on-site matrix elements from the bulk calculation and those from the calculation with the defect, but far away from the location of the defect, give a direct measure of the potential offset between the two calculations. This offset can then be used to align all of the diagonal matrix elements from one calculation with those of the other, prior to them being combined in a tight-binding Hamiltonian for a larger nanostructure. The potential alignment approach described above has been used for transport calculations (see Sec. VII.A.2), and for the determination of band offsets and Schottky barriers (Singh-Miller, 2009), for calculating formation energies of point defects (Corsetti and Mostofi, 2011), and for developing tight-binding models of the surfaces of topological insulators (Zhang *et al.*, 2010) (see Sec. VI.A.4).

It should be noted that charge self-consistency could play an important role when trying to build the electronic structure of large or complex nanostructures, and one might have to resort to more sophisticated approaches. As a suggestion, electrostatic consistency could be attained solving the Poisson equation for the entire system (Léonard and Tersoff, 1999), then using the updated electrostatic potential to shift appropriately the diagonal elements of the Hamiltonian. In a more general fashion, the electronic charge density and the Hartree and exchange-correlation potentials could be updated and optimized self-consistently in a basis of disentangled, frozen WFs, using a generalized occupation matrix (Marzari, Vanderbilt, and Payne, 1997).

2. Quantum transport

A local representation of electronic structure is particularly suited to the study of quantum transport, as illustrated here in the case of quasi-one-dimensional systems. We consider a system composed of a conductor C connected to two semi-infinite leads R and L as shown in Fig. 34. The conductance $\mathcal{G}$ through a region of interacting electrons is related to the scattering properties of the region itself via the Landauer formula (Landauer, 1970)

$$\mathcal{G}(E) = \frac{2e^2}{h}\mathcal{T}(E),\tag{124}$$

where the transmission function $\mathcal{T}(E)$ is the probability that an electron with energy E injected at one end of the conductor will transmit to the other end. This transmission function can be expressed in terms of the Green's functions of the conductors and the coupling of the conductor to the leads (Fisher and Lee, 1981; Datta, 1995),

$$\mathcal{T}(E) = \mathrm{Tr}(\Gamma_L G_C^r \Gamma_R G_C^a),\tag{125}$$

where $G_C^{\{r,a\}}$ are the retarded (r) and advanced (a) Green's functions of the conductor, and $\Gamma_{\{L,R\}}$ are functions that describe the coupling of the conductor to the left (L) and right (R) leads. Since $G^a = (G^r)^\dagger$, we consider G^r only and drop the superscript.

Expressing the Hamiltonian H of the system in terms of a localized, real-space basis set enables it to be partitioned without ambiguity into submatrices that correspond to the individual subsystems. A concept that is particularly useful is that of a *principal layer* (PL) (Lee and Joannopoulos, 1981), which is a section of lead that is sufficiently long such that $\langle \chi_i^n|H|\chi_j^m\rangle \simeq 0$ if $|m - n| \geq 2$, where H is the Hamiltonian operator of the entire system and $|\chi_i^n\rangle$ is the ith basis function in the nth PL. Truncating the matrix elements of the Hamiltonian in this way incurs a small error which is systematically controlled by increasing the size of the PL. The Hamiltonian matrix in this basis then takes the block diagonal form (see also Fig. 34)

$$H = \begin{pmatrix} \ddots & \vdots & \vdots & \vdots & \vdots & \vdots & \iddots \\ \cdots & H_L^{\bar{0}\bar{0}} & H_L^{\bar{1}\bar{0}} & 0 & 0 & 0 & \cdots \\ \cdots & H_L^{\bar{1}\bar{0}\dagger} & H_L^{\bar{0}\bar{0}} & h_{LC} & 0 & 0 & \cdots \\ \cdots & 0 & h_{LC}^\dagger & H_C & h_{CR} & 0 & \cdots \\ \cdots & 0 & 0 & h_{CR}^\dagger & H_R^{00} & H_R^{01} & \cdots \\ \cdots & 0 & 0 & 0 & H_R^{01\dagger} & H_R^{00} & \cdots \\ \iddots & \vdots & \vdots & \vdots & \vdots & \vdots & \ddots \end{pmatrix},\tag{126}$$

where H_C represents the Hamiltonian matrix of the conductor region, $H_L^{\bar{0}\bar{0}}$ and H_R^{00} are those of each PL of the left and right
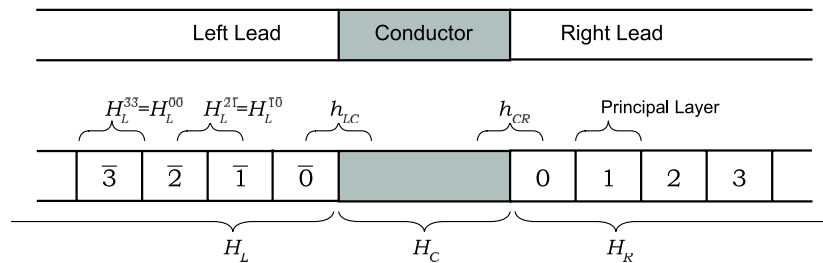
FIG. 34 (color online). Illustration of the lead-conductor-lead geometry used in quantum-transport calculations. The conductor (C), left lead (L), and right lead (R) are described by Hamiltonians H_C, H_L, and H_R, respectively. The coupling between adjacent regions is described by matrices h_{LC} and h_{CR}. The leads are split into principal layers corresponding to the submatrices in Eq. (126). From Shelley *et al.*, 2011.

leads, respectively, $H_L^{\bar{1}\bar{0}}$ and H_R^{01} are couplings between adjacent PLs of lead, and h_{LC} and h_{CR} give the coupling between the conductor and the leads.

In order to compute the Green's function of the conductor one starts from the equation satisfied by the Green's function G of the whole system,

$$(\epsilon - H)G = \mathbb{1}, \tag{127}$$

where $\mathbb{1}$ is the identity matrix, and $\epsilon = E + i\eta$, where η is an arbitrarily small, real constant.

From Eqs. (126) and (127), it can be shown that the Green's function of the conductor is then given by (Datta, 1995)

$$G_C = (\epsilon - H_C - \Sigma_L - \Sigma_R)^{-1}, \tag{128}$$

where we define $\Sigma_L = h_{LC}^\dagger g_L h_{LC}$ and $\Sigma_R = h_{RC} g_R h_{RC}^\dagger$, the self-energy terms due to the semi-infinite leads, and $g_{\{L,R\}} = (\epsilon - H_{\{L,R\}})^{-1}$, the surface Green's functions of the leads.

The self-energy terms can be viewed as effective Hamiltonians that arise from the coupling of the conductor with the leads. Once the Green's functions of the leads are known, the coupling functions $\Gamma_{\{L,R\}}$ can be easily obtained as (Datta, 1995)

$$\Gamma_{\{L,R\}} = i[\Sigma_{\{L,R\}}^r - \Sigma_{\{L,R\}}^a], \tag{129}$$

where $\Sigma_{\{L,R\}}^a = (\Sigma_{\{L,R\}}^r)^\dagger$.

As for the surface Green's functions $g_{\{L,R\}}$ of the semi-infinite leads, it is well known that any solid (or surface) can be viewed as an infinite (semi-infinite in the case of surfaces) stack of principal layers with nearest-neighbor interactions (Lee and Joannopoulos, 1981). This corresponds to transforming the original system into a linear chain of PLs. Within this approach, the matrix elements of Eq. (127) between layer orbitals yield a set of coupled equations for the Green's functions which can be solved using an efficient iterative scheme due to López Sancho, López Sancho, and Rubio (1984) and López Sancho *et al.* (1985). Knowledge of the finite Hamiltonian submatrices in Eq. (126), therefore, is sufficient to calculate the conductance of the open lead-conductor-lead system given by Eq. (124).

There are a number of possibilities for the choice of localized basis $|\chi\rangle$. Early work used model tight-binding Hamiltonians (Chico *et al.*, 1996; Saito, Dresselhaus, and Dresselhaus, 1996; Anantram and Govindan, 1998; Nardelli, 1999), but the increasing sophistication of computational methods meant that more realistic first-principles approaches could be adopted (Buongiorno Nardelli, Fattebert, and Bernholc, 2001; Fattebert and Buongiorno Nardelli, 2003). Maximally localized Wannier functions were first used in this context by Calzolari *et al.* (2004), who studied Al and C chains and a (5,0) carbon nanotube with a single Si substitutional defect, and by Lee, Nardelli, and Marzari (2005), who studied covalent functionalizations of metallic nanotubes, capabilities now encoded in the open-source packages WANNIER90 (Mostofi *et al.*, 2008) and WanT (Ferretti, Bonferroni, Calzolari, and Nardelli, 2005). This was quickly followed by a number of applications to ever more realistic systems, studying transport through molecular junctions (Thygesen and Jacobsen, 2005; Strange *et al.*, 2008), decorated carbon nanotubes and nanoribbons (Lee and Marzari,

2006; Cantele *et al.*, 2009; Rasuli, Rafii-Tabar, and Zad, 2010; Li, Poilvert, and Marzari, 2011), organic monolayers (Bonferroni *et al.*, 2008), and silicon nanowires (Shelley and Mostofi, 2011), as well as more methodological work on improving the description of electron correlations within this formalism (Ferretti, Calzolari, Di Felice, and Manghi, 2005; Ferretti, Calzolari, Di Felice, Manghi, Caldas *et al.*, 2005; Calzolari, Ferretti, and Nardelli, 2007; Bonferroni *et al.*, 2008).

The formulation described above relies on a localized description of the electronic-structure problem, and it should be noted that several approaches for calculating electronic transport properties have been developed using localized basis sets rather than MLWFs, ranging from Gaussians (Hod, Peralta, and Scuseria, 2006) to numerical atomic orbitals (Brandbyge *et al.*, 2002; Markussen *et al.*, 2006; Rocha *et al.*, 2008).

In addition, in the Keldysh formalism one can add more complex interaction terms to the self-energies, such as electron-phonon or (for molecular conductors) electron-vibration interactions (Frederiksen *et al.*, 2007). These latter can also be conveniently expressed in a MLWFs representation, and a natural extension of the previous quantum-transport formalism to the case of inelastic scattering channels due to electron-vibration interactions has recently been developed in a MLWFs basis (Kim and Marzari, 2012).

3. Semiempirical potentials

First-principles molecular-dynamics simulations of large-scale (thousands of atoms) systems for long (nanoseconds) time scales are computationally costly, if not intractable. Molecular-dynamics simulations with empirical interatomic potentials are a feasible alternative and there is an ongoing effort in developing potentials that are more accurate, more transferable, and, therefore, more predictive. One approach in this direction is to fit the parameters that appear within empirical potentials so that they reproduce target properties, such as forces and stresses, obtained from accurate DFT calculations on a large number of atomic configurations (Ercolessi and Adams, 1994). In the particular class of ionic condensed-matter systems, e.g., first and second row metal oxides, it is well known that the electronic properties of an ion can be significantly affected by its coordination environment and, therefore, that it is also important to include an accurate description of polarization effects in any interatomic potential. While simple potentials may attempt to account for these many-body effects in an average manner, the result is that the potential loses transferability and, hence, predictive power. As a result, there has been some effort in developing potentials such that they are also fitted to information from DFT calculations regarding the electron distribution around each ion, in particular, dipoles and quadrupoles.

In this vein, Aguado *et al.* (2003) introduced the use of MLWFs in order to calculate dipole and quadrupole moments in MgO and used these to construct an interatomic potential based on the aspherical ion method potential (Rowley *et al.*, 1998). In an ionic system such as this, MLWFs are found to be well localized close to the ions and each can therefore be associated unambiguously with a particular ion. The dipole moment $\boldsymbol{\mu}^I$ of each ion I is then calculated as

$$\mu_\alpha^I = -2 \sum_{n \in I} \bar{r}_{n\alpha} + Z_I R_\alpha^I, \tag{130}$$

where α is a Cartesian component, Z_I is the charge of ion I at position $\mathbf{R}_I$, $\bar{r}_{n\alpha}$ is the center of the nth MLWF and is given by Eq. (28) or Eq. (43), and the factor of 2 accounts for spin degeneracy.

For the quadrupole moments $\theta_{\alpha\beta}^I$, the fact that the MLWFs are localized within the simulation cell is exploited in order to explicitly compute the real-space integral

$$\theta_{\alpha\beta}^I = -2 \sum_{n \in I} \int_{V_c^I} d\mathbf{r} |w_n(\mathbf{r})|^2 [3r_\alpha^I r_\beta^I - (r^I)^2 \delta_{\alpha\beta}]/2, \tag{131}$$

where $\mathbf{r}^I = \mathbf{r} - \mathbf{R}^I$, and the integral is performed over a sphere V_c^I, centered on R^I, such that the integral of the electron density associated with the MLWF within this sphere is greater than some threshold. The potential obtained exhibits good transferability and the method has been used to parametrize similar potentials for other alkaline earth oxides (Aguado, Bernasconi, and Madden, 2003), Al_2O_3 (Jahn, Madden, and Wilson, 2006), and the CaO-MgO-Al_2O_3-SiO_2 (CMAS) mineral system (Jahn and Madden, 2007).

The use of MLWFs for attempting to obtain better interatomic potentials has not been limited to the solid state. In biomolecular simulations, an important factor in developing accurate force fields is having an accurate description of the electrostatic potential. Starting from DFT calculations on isolated molecules, Sagui *et al.* (2004) partition the electronic charge density into contributions from individual MLWFs and calculate the multipoles of each using an order-by-order expansion of gauge-invariant cumulants (Resta, 1998; Souza, Wilkens, and Martin, 2000) [see Sagui *et al.* (2004) for full details]. Using fast particle mesh Ewald and multigrid methods, these multipoles can then be used to generate the electrostatic potential. Sagui *et al.* (2004) showed that higher order multipoles, e.g., up to hexadecapole, may be incorporated without computational or numerical difficulty and that agreement with the "exact" potential obtained from DFT is very good. The idea of partitioning the charge density according to individual MLWFs was also employed by Kirchner and Hutter (2004) in order to determine atomic charges in dimethyl sulfoxide, showing that there can be significant deviations between the gaseous and aqueous forms and, therefore, underlining the importance of using polarizable force fields for describing solvated systems.

Finally, we note that recently Rotenberg *et al.* (2010) proposed force fields whose parametrization is based entirely on a partitioning of the electronic density in terms of MLWFs. Their method was applied successfully to water and molten salts. It remains to be seen whether the approach is extensible to more complex or anisotropic systems.

4. Improving system-size scaling

The localized nature of MLWFs in real space makes them a natural and appealing choice of basis for electronic-structure calculations as the sparsity exhibited by operators that are represented in a localized basis may be exploited in order to achieve computational efficiencies and improved scaling of numerical algorithms with respect to system size. Recently,

therefore, MLWFs have been used for this very purpose in a number of contexts and we mention, in brief, some of them here.

In QMC calculations (Foulkes *et al.*, 2001), a significant computational effort is expended in evaluating the Slater determinant for a given electronic configuration of N electrons. These Slater determinants are usually constructed from a set of extended single-particle states, obtained from, e.g., a DFT or Hartree-Fock calculation, represented in a basis set of, e.g., extended plane waves. This gives rise to $\mathcal{O}(N^3)$ scaling of the computational cost of evaluating such a determinant. Williamson, Hood, and Grossman (2001) suggested, instead, to use MLWFs that were smoothly truncated to zero beyond a certain cutoff radius that is independent of system size. This ensures that each electron falls only within the localization region of a fixed number of MLWFs, thus reducing the asymptotic scaling by one factor of N. Furthermore, by representing the MLWFs in a basis of localized spline functions, rather than plane waves or even Gaussian functions, the evaluation of each orbital is rendered independent of system size, thereby reducing the overall cost of computing the determinant of the given configuration to $\mathcal{O}(N)$. More recently, rather than truncated MLWFs, the use of nonorthogonal orbitals obtained by projection (Reboredo and Williamson, 2005) or other localization criteria (Alfè and Gillan, 2004) has also been suggested.

In another development, Wu, Selloni, and Car (2009) used MLWFs in order to compute efficiently Hartree-Fock exact-exchange integrals in extended systems. Hybrid exchange-and-correlation functionals (Becke, 1993) for DFT calculations, in which some proportion of Hartree-Fock exchange is included in order to alleviate the well-known problem of self-interaction that exists in local and semilocal functionals such as the local-density approximation and its generalized gradient-dependent variants, have been used relatively little in extended systems. This is predominantly due to the computational cost associated with evaluating the exchange integrals between extended eigenstates that are represented in a plane-wave basis set. Wu, Selloni, and Car (2009) showed that by performing a unitary transformation of the eigenstates to a basis of MLWFs, and working in real space in order to exploit the fact that spatially distant MLWFs have exponentially vanishing overlap, the number of such overlaps that needs to be calculated scales linearly, in the limit of large system size, with the number of orbitals (as opposed to quadratically), which is a sufficient improvement to enable Car-Parrinello molecular-dynamics simulations with hybrid functionals.

Similar ideas that exploit the locality of MLWFs have been applied to many-body perturbation theory approaches for going beyond DFT and Hartree-Fock calculations, for example, in the contexts of the GW approximation (Umari, Stenuit, and Baroni, 2009), the evaluation of local correlation in extended systems (Buth *et al.*, 2005; Pisani *et al.*, 2005), and the Bethe-Salpeter equation (Sasioglu *et al.*, 2010). The improved scaling and efficiency of these approaches open the possibility of such calculations on larger systems than previously accessible.

Finally, we note that MLWFs have been used recently to compute van der Waals (vdW) interactions in an approximate but efficient manner (Silvestrelli, 2008, 2009b;

Andrinopoulos, Hine, and Mostofi, 2011). The method is based on an expression due to Andersson, Langreth, and Lundqvist (1996) for the vdW energy in terms of pairwise interactions between fragments of charge density. MLWFs provide a localized decomposition of the electronic charge density of a system and can be used as the basis for computing the vdW contribution to the total energy in a postprocessing (i.e., non-self-consistent) fashion. In order to render tractable the necessary multidimensional integrals, the true MLWFs of the system are substituted by analytic hydrogenic orbitals that have the same centers and spreads as the true MLWFs. The approach has been applied to a variety of systems, including molecular dimers, molecules physisorbed on surfaces, water clusters, and weakly bound solids (Silvestrelli, 2008, 2009a, 2009b; Silvestrelli *et al.*, 2009; Andrinopoulos, Hine, and Mostofi, 2011; Espejo *et al.*, 2012). Recently, Ambrosetti and Silvestrelli (2012) suggested an alternative, simpler formulation that is based on London's expression for the van der Waals energy of two interacting atoms (Eisenschitz and London, 1930).

B. WFs as a basis for strongly correlated systems

For many strongly correlated electron problems, the essential physics of the system can be explained by considering only a subset of the electronic states. A recent example is understanding the behavior of unconventional (high-T_c) superconductors, in which a great deal of insight can be gained by considering only the MLWFs of p and d character on Cu and O, respectively, for cuprates (Sakakibara *et al.*, 2010), and those on As and Fe, respectively, for the iron pnictides (Cao, Hirschfeld, and Cheng, 2008; Kuroki *et al.*, 2008; Hu and Hu, 2010; Suzuki, Usui, and Kuroki, 2011). Other strongly correlated materials for which MLWFs have been used to construct minimal models to help understand the physics include manganites (Kovacik and Ederer, 2010), topological insulators (Zhang, Liu, Qi, Dai *et al.*, 2009; Zhang, liu, Qi, Deng *et al.*, 2009) (see also Sec. VI.A.4), and polyphenylene vinylene, in particular, relating to electron-hole excitations (Karabunarliev and Bittner, 2003a, 2003b).

Below we outline some of the general principles behind the construction and solution of such minimal models.

1. First-principles model Hamiltonians

Consider a strongly correlated electron system described by a Hamiltonian of the form

$$\hat{H} = \hat{H}_0 + \hat{H}_{\text{int}}, \tag{132}$$

where $\hat{H}_0$ contains the one-particle terms and $\hat{H}_{\text{int}}$ the interaction (e.g., Coulomb repulsion) terms. In second-quantized notation and expressed in terms of a complete tight-binding basis, this can be expressed as

$$\hat{H} = \sum_{ij} \sum_{\mathbf{R},\mathbf{R}'} h_{ij}^{\mathbf{R}\mathbf{R}'}(\hat{c}_{i\mathbf{R}}^{\dagger}\hat{c}_{j\mathbf{R}'} + \text{H.c.})$$
$$+ \frac{1}{2}\sum_{ijkl} \sum_{\mathbf{R}\mathbf{R}'\mathbf{R}''\mathbf{R}'''} U_{ijkl}^{\mathbf{R}\mathbf{R}'\mathbf{R}''\mathbf{R}'''} \hat{c}_{i\mathbf{R}}^{\dagger}\hat{c}_{j\mathbf{R}'}^{\dagger}\hat{c}_{k\mathbf{R}''}\hat{c}_{l\mathbf{R}'''},$$

$$\tag{133}$$

where $\mathbf{R}$ labels the correlated site, lowercase indices (such as i and j) refer to the orbital and spin degrees of freedom, $\hat{c}_{i\mathbf{R}}^{\dagger}$ ($\hat{c}_{i\mathbf{R}}$) creates (annihilates) an electron in the orbital $w_{i\mathbf{R}}(\mathbf{r})$, and $\mathbf{h}$ and $\mathbf{U}$ contain the matrix elements of the single-particle and (screened) interaction parts of the Hamiltonian, respectively.

Usually, a complete tight-binding representation of all the states of the system is not required, and the essential physics can be described by a smaller set of physically relevant orbitals. For example, those states close to the Fermi level, or those of a particularly symmetry, or those localized on specific sites, may be sufficient. In this way, the size of the basis used to represent the many-body Hamiltonian is greatly reduced, rendering Eq. (133) more amenable to solution [see, e.g., Solovyev (2008)].

In this spirit, MLWFs obtained from DFT calculations have been used as the orbital basis for these minimal models.[20] Advantages of using MLWFs include the fact that they can be chosen to span precisely the required energy range (using the disentanglement procedure outlined in Sec. II.I.2), and that they naturally incorporate hybridization and bonding appropriate to their local environment.

The single-particle hopping parameters of the model Hamiltonian are easily obtained from the matrix elements of the DFT Hamiltonian represented in the basis of MLWFs, using Eq. (101). The interaction parameters of the model Hamiltonian can be calculated, for example, from either constrained DFT (Dederichs *et al.*, 1984; McMahan, Annett, and Martin, 1990; Anisimov, Zaanen, and Andersen, 1991; Nakamura *et al.*, 2006), within the random phase approximation (Springer and Aryasetiawan, 1998; Aryasetiawan *et al.*, 2004; Solovyev and Imada, 2005; Miyake, Aryasetiawan, and Imada, 2009), or by direct calculation of the matrix elements of a suitable screened Coulomb interaction between, for example, MLWFs (Miyake *et al.*, 2006; Nakamura *et al.*, 2006). It is interesting to note that numerical evidence suggests that on-site Coulomb interactions (both screened and bare) are maximized when calculated with a basis of MLWFs (Miyake and Aryasetiawan, 2008) and, therefore, that MLWFs may be an optimally localized basis for this purpose. This is perhaps not surprising given the broad similarities between MLWFs and WFs obtained via the Edmiston-Ruedenberg localization scheme (Edmiston and Ruedenberg, 1963), discussed in Sec. III.A, which maximizes the electronic Coulomb self-interaction of each orbital.

Once the parameters of the model have been determined, the model Hamiltonian is then said to be "from first principles," in the sense that the parameters of the model are determined from DFT rather than by fitting to experiments. The many-body Hamiltonian in the minimal basis of MLWFs may then be solved by direct diagonalization or by one of a number of other approaches that are too numerous to review here but which include, for example, the dynamical mean-field theory approach. DMFT maps the many-body problem on to an Anderson impurity model (Anderson, 1961) in which on-site correlation is treated nonperturbatively and

---

[20]An alternative approach is to obtain the orbitals via the downfolding method, discussed in Sec. III.

the correlated sites are coupled to a self-consistent energy bath that represents the rest of the system. The impurity sites, also known as the correlated subspaces, are defined by localized projector functions and MLWFs are a common choice (Lechermann *et al.*, 2006; Trimarchi *et al.*, 2008; Weber, Haule, and Kotliar, 2010). In particular, one would typically choose orbitals of d or f character associated with transition metal, lanthanoid, or actinoid ions. The Green's function for the impurity site is calculated self-consistently, for example, by a numerical functional integration (which constitutes the bulk of the computation). Further self-consistency with the DFT ground state may also be attained by using the solution to the impurity problem to update the electronic density that is then used to construct an updated Kohn-Sham potential, which determines a new set of eigenstates, MLWFs and, hence, model Hamiltonian parameters that can then be fed back in to the DMFT cycle. See Kotliar *et al.* (2006) and Held (2007) for further details; other examples that use localized Wannier functions or generalized tight-binding models to address correlated electrons problems can be found in Ku *et al.* (2002), Anisimov *et al.* (2005), Korshunov *et al.* (2005), Amadon *et al.* (2008), Held *et al.* (2008), and Korotin *et al.* (2008).

2. Self-interaction and DFT + Hubbard U

In the approaches just described, the results of a DFT calculation are used to parametrize the model Hamiltonian of a strongly correlated electron system. In contrast, in a DFT + U formulation (Anisimov, Zaanen, and Andersen, 1991; Anisimov *et al.*, 1993) the energy functional is explicitly augmented with a Hubbard term U (Hubbard, 1963) aimed at improving the description of strong interactions, such as those associated with localized d and f electronic states, and at repairing the mean-field underestimation of on-site Coulomb repulsions.

In DFT + U the Hubbard manifold is defined by a set of projectors that are typically atomic-like orbitals of d or f character. Localization of this manifold plays a key role, since DFT + U effectively corrects for the lack of piecewise linearity in approximate energy functionals (Perdew *et al.*, 1982; Cococcioni and de Gironcoli, 2005) and thus greatly reduces self-interaction errors (Perdew and Zunger, 1981; Kulik *et al.*, 2006; Mori-Sánchez, Cohen, and Yang, 2008). Since strongly localized orbitals are those that suffer most from self-interaction, MLWFs can become an appealing choice to define Hubbard manifolds adapted to the chemistry of the local environment. In fact, MLWFs have been successfully used as Hubbard projectors (Fabris *et al.*, 2005; Anisimov *et al.*, 2007; Miyake and Aryasetiawan, 2008), and it has been argued that their shape can constitute an additional degree of freedom in the calculations (O'Regan *et al.*, 2010), provided their localized, atomic character is maintained. It should also be pointed out that the value of U entering the calculations should not be considered universal, as it depends strongly on the manifold chosen [(e.g., for pseudopotential calculations on the oxidation state of the reference atomic calculation (Kulik and Marzari, 2008), or on the structure or electronic structure of the problem studied].

It should be pointed out that functionals that aim to correct directly for some effects of self-interaction, such as the Perdew-Zunger correction (Perdew and Zunger, 1981) or Koopmans-compliant functionals (Dabo *et al.*, 2010), can

lead naturally in a periodic system to Wannier-like localized orbitals that minimize the total energy (Stengel and Spaldin, 2008; Park *et al.*, 2011), while the canonical orbitals that diagonalize the Hamiltonian still preserve Bloch periodicity.

VIII. WANNIER FUNCTIONS IN OTHER CONTEXTS

As described in Sec. II.A, Wannier functions provide an alternative, localized, description of a manifold of states spanned by the eigenstates (energy bands) of a single-particle Hamiltonian that describes electrons in a periodic potential. The equivalence of the Wannier representation and the eigenstate representation may be expressed in terms of the band projection operator $\hat{P}$; see Eq. (15). This operator satisfies the idempotency condition $P^2 = P$, which embodies simultaneously the requirements of orthogonality and Pauli exclusion.

From their conception, and until relatively recently, Wannier functions have been used almost exclusively in this context, namely, to represent a manifold of single-particle orbitals for electrons. Furthermore, as discussed in Sec. II, we need not restrict ourselves to an isolated group of states, such as the occupied manifold: the disentanglement procedure enables a subspace of a larger manifold, e.g., of occupied and unoccupied states, to be selected which may then be Wannierized. This has, for example, opened up areas of application in which Wannier functions are used as tight-binding basis functions for electronic structure and transport calculations, as described in Secs. VI and VII.

From a general mathematical point of view, however, the set of orthogonal eigenfunctions of any self-adjoint (Hermitian) operator may be "rotated" by unitary transformation to another orthogonal basis that spans the same space. As we have seen, the unitary transformation is arbitrary and may be chosen to render the new basis set maximally localized, which has computational advantages when it comes to representing physical quantities that are short ranged. When the operator in question has translational symmetry, the maximally localized functions thus obtained are reminiscent of the Wannier functions familiar from electronic-structure theory. Often, such a basis is also preferable to using another localized basis because information regarding the symmetries of the self-adjoint operator from which the basis is derived is encoded within it.

These ideas have led to the appropriation of the MLWF formalism described in Sec. II for contexts other than the description of electrons: the single-particle electronic Hamiltonian is replaced by another suitable periodic self-adjoint operator, and the Bloch eigenstates are replaced by the eigenfunctions of that operator, which may then be transformed to give a MLWF-like representation that may be used as an optimal and compact basis for the desired calculation, for example, to analyze the eigenmodes of the static dielectric matrix in ice and liquid water (Lu, Gygi, and Galli, 2008).

Next we review the three most prominent of these applications, namely, to the study of phonons, photonic crystals, and cold-atom lattices.

A. Phonons

Lattice vibrations in periodic crystals are usually described in terms of normal modes, which constitute a delocalized

orthonormal basis for the space of vibrations of the lattice such that an arbitrary displacement of the atoms in the crystal may be expressed in terms of a linear combination of its normal modes. By analogy with the electronic case, Kohn (1973) first showed (for isolated phonon branches in one dimension) that a similar approach could be used for constructing a localized orthonormal basis for lattice vibrations that span the same space as the delocalized normal modes. The approach was subsequently generalized to isolated manifolds in three dimensions by Tindemans-van Eijndhoven and Kroese (1975). The localized modes are now generally referred to as lattice Wannier functions (LWFs) (Rabe and Waghmare, 1995; Íñiguez, Garcia, and Pérez-Mato, 2000).

Following the notation of Sec. VI.D, we denote by $\mathbf{q}$ the phonon wave vector, and by $e_\mathbf{q}$ the matrix whose columns are the eigenvectors of the dynamical matrix. As in the case of electronic Wannier functions, the phases of these eigenvectors are undetermined. A unitary transformation of the form

$$[\tilde{e}_\mathbf{q}]_{\mu\nu} = [M_\mathbf{q} e_\mathbf{q}]_{\mu\nu}, \tag{134}$$

performed within a subspace of dispersion branches that is invariant with respect to the space group of the crystal, results in an equivalent representation of generalized extended modes $[\tilde{e}_\mathbf{q}]_{\mu\nu}$ that are also orthonormal. LWFs may then be defined by

$$[w_\mathbf{R}]_{\mu\nu} = \frac{1}{N_p} \sum_\mathbf{q} e^{-i\mathbf{q}\cdot\mathbf{R}} [\tilde{e}_\mathbf{q}]_{\mu\nu}, \tag{135}$$

with the associated inverse transform

$$[\tilde{e}_\mathbf{q}]_{\mu\nu} = \sum_\mathbf{R} e^{i\mathbf{q}\cdot\mathbf{R}} [w_\mathbf{R}]_{\mu\nu}. \tag{136}$$

By construction, the LWFs are periodic according to $w_{\mathbf{R}+\mathbf{t}} = w_\mathbf{R}$, where $\mathbf{t}$ is a translation vector of the Born–von Kármán supercell.

The freedom inherent in Eq. (134) allows very localized LWFs to be constructed, by suitable choice of the transformation matrix $M_\mathbf{q}$. As noted by Kohn (1973), the proof of exponential localization of LWFs follows the same reasoning as for electronic Wannier functions (see Sec. II.G).

The formal existence of LWFs was first invoked in order to justify the construction of approximate so-called *local modes* of vibration which were used in effective Hamiltonians for the study of systems exhibiting strong coupling between electronic states and lattice instabilities, such as perovskite ferroelectrics (Thomas and Muller, 1968; Pytte and Feder, 1969).

Zhong, Vanderbilt, and Rabe (1994) used first-principles methods in order to calculate the eigenvector associated with a soft mode at $\mathbf{q} = \mathbf{0}$ in BaTiO$_3$. A localized displacement pattern, or local mode, of the atoms in the cell was then parametrized, taking account of the symmetries associated with the soft mode, and the parameters were fitted to reproduce the calculated soft mode eigenvector at $\mathbf{q} = \mathbf{0}$. The degree of localization of the local mode was determined by setting all displacement parameters to zero beyond the second shell of atoms surrounding the central atom. Although this spatial truncation results in the local modes being nonorthogonal, it does not hamper the accuracy of practical calculations. As the local modes are constructed using information

only from the eigenvector at $\mathbf{q} = \mathbf{0}$, they do not correspond to a particular phonon branch in the Brillouin zone. Rabe and Waghmare (1995) generalized the approach to allow fitting to more than just $\mathbf{q} = \mathbf{0}$, but rather to a small set of, usually high-symmetry, $\mathbf{q}$ points. The phase indeterminacy of the eigenvectors is exploited in order to achieve optimally rapid decay of the local modes. Another approach, introduced by Íñiguez, Garcia, and Pérez-Mato (2000), constructs local modes via a projection method that preserves the correct symmetry. The procedure is initiated from simple atomic displacements as trial functions. The quality of the local modes thus obtained may be improved by systematically densifying the $\mathbf{q}$-point mesh that is used in Eq. (135). Although there is no formal criterion of maximal localization in the approach, it also results in nonorthogonal local modes that decay exponentially.

These ideas for generating local modes from first-principles calculations have been particularly successful for the study of structural phase transitions in ferroelectrics such as BaTiO$_3$ (Zhong, Vanderbilt, and Rabe, 1994, 1995), PbTiO$_3$ (Waghmare and Rabe, 1997), KbNiO$_3$ (Krakauer *et al.*, 1999), Pb$_3$GeTe$_4$ (Cockayne and Rabe, 1997), and perovskite superlattices (Lee, Waghmare, and Yu, 2008).

The use of maximal localization as an exclusive criterion for determining LWFs was first introduced by Giustino and Pasquarello (2006). In this work, a real-space periodic position operator for noninteracting phonons was defined by analogy with the periodic position operator for noninteracting electrons [Eq. (43)].

The problem of minimizing the total spread of a set of WFs in real space is equivalent to the problem of simultaneously diagonalizing the three noncommuting matrices corresponding to the three components of the position operator represented in the WF basis, and Giustino and Pasquarello (2006) used the method outlined by Gygi, Fattebert, and Schwegler (2003) to achieve this. It is worth noting that Giustino and Pasquarello (2006) furthermore defined a generalized spread functional that, with a single parameter, allows a trade-off between localization in energy (the eigenstate or Bloch limit) and localization in space (the Wannier limit), resulting in so-called *mixed Wannier-Bloch functions* which may be obtained for the electrons as well as the phonons.

Finally, as first pointed out by Kohn (1973), and subsequently by Giustino, Cohen, and Louie (2007), maximally localized lattice Wannier functions correspond to displacements of individual atoms. This may be seen by considering a vibrational eigenmode, $\hat{\mathbf{e}}_{\mathbf{q}s}^\nu \equiv \mathbf{e}_{\mathbf{q}s}^\nu e^{i\mathbf{q}\cdot\mathbf{R}}$, and noting that it may be expressed as

$$\hat{\mathbf{e}}_{\mathbf{q}s}^\nu = \sum_{s'\mathbf{R}'} e^{i\mathbf{q}\cdot\mathbf{R}'} \delta_{\mathbf{R}\mathbf{R}'} \delta_{ss'} \mathbf{e}_{\mathbf{q}s'}^\nu. \tag{137}$$

Equation (137) stands in direct correspondence to the electronic analog given by the inverse of Eq. (10), from which we conclude that the LWFs do indeed correspond to individual atomic displacements $\delta_{\mathbf{R}\mathbf{R}'}\delta_{ss'}$ and, furthermore, that the required unitary transformation is the matrix of eigenvectors $[e_\mathbf{q}]_{\mu\nu}$. As discussed in Sec. VI.D, Giustino, Cohen, and Louie (2007) exploited this property for the efficient interpolation of dynamical matrices and calculation of electron-phonon couplings.

B. Photonic crystals

Photonic crystals are periodic arrangements of dielectric materials that are designed and fabricated in order to control the flow of light (John, 1987; Yablonovitch, 1987). They are very much to light what semiconductors are to electrons and, similar to semiconductors that exhibit an electronic band gap in which an electron may not propagate, photonic crystals can be engineered to exhibit photonic band gaps: ranges of frequencies in which light is forbidden to propagate in the crystal. In the electronic case, a band gap results from scattering from the periodic potential due to the ions in the crystal; in the photonic case, it arises from scattering from the periodic dielectric interfaces of the crystal. Again by analogy with electronic materials, localized defect states can arise in the gap by the deliberate introduction of defects into a perfect photonic crystal structure. The ability to control the nature of these states promises to lead to entirely light-based integrated circuits, which would have a number of advantages over their electronic counterparts, including greater speeds of propagation, greater bandwidth, and smaller energy losses (Joannopoulos, Villeneuve, and Fan, 1997).

In SI units, Maxwell's equations in source-free regions of space are

$$\nabla \cdot \mathbf{E} = 0, \qquad \nabla \cdot \mathbf{B} = 0, \tag{138}$$

$$\nabla \times \mathbf{E} = -\frac{\partial \mathbf{B}}{\partial t}, \qquad \nabla \times \mathbf{H} = \frac{\partial \mathbf{D}}{\partial t}, \tag{139}$$

where the constitutive relations between the fields are

$$\mathbf{D} = \epsilon_r \epsilon_0 \mathbf{E}, \qquad \mathbf{B} = \mu_r \mu_0 \mathbf{H}. \tag{140}$$

Considering nonmagnetic materials ($\mu_r = 1$) with a position dependent dielectric constant $\epsilon_r(\mathbf{r})$, and fields that vary with a sinusoidal dependence $e^{-i\omega t}$, it is straightforward to derive electromagnetic wave equations in terms of either the electric field $\mathbf{E}$ or the magnetic field $\mathbf{H}$,

$$\nabla \times [\nabla \times \mathbf{E}(\mathbf{r})] = \frac{\omega^2}{c^2} \epsilon_r(\mathbf{r}) \mathbf{E}(\mathbf{r}), \tag{141}$$

$$\nabla \times [\epsilon_r^{-1}(\mathbf{r}) \nabla \times \mathbf{H}(\mathbf{r})] = \frac{\omega^2}{c^2} \mathbf{H}(\mathbf{r}), \tag{142}$$

where $c = (\mu_0 \epsilon_0)^{-1/2}$ is the speed of light.

For a perfect periodic dielectric structure, $\epsilon_r(\mathbf{r}) = \epsilon_r(\mathbf{r} + \mathbf{R})$, where $\mathbf{R}$ is a lattice vector. Application of Bloch's theorem leads to solutions that are indexed by wave vector $\mathbf{k}$, which may be chosen to lie in the first Brillouin zone, and a band index n. For example,

$$\mathbf{H}_{n\mathbf{k}}(\mathbf{r}) = e^{i\mathbf{k} \cdot \mathbf{r}} \mathbf{u}_{n\mathbf{k}}(\mathbf{r}),$$

where $\mathbf{u}_{n\mathbf{k}}(\mathbf{r}) = \mathbf{u}_{n\mathbf{k}}(\mathbf{r} + \mathbf{R})$ is the periodic part of the magnetic field Bloch function. The electromagnetic wave equations can be solved, and hence the Bloch functions obtained, by a number of methods including a finite-difference time domain (Yee, 1966; Taflove and Hagness, 2005), transfer matrix (Pendry and Mackinnon, 1992; Pendry, 1996), empirical tight-binding methods (Lidorikis *et al.*, 1998; Yariv *et al.*, 1999), and Galerkin techniques in which the field is expanded in a set of orthogonal basis functions (Mogilevtsev, Birks, and

Russell, 1999). Within the latter class, use of a plane-wave basis set is particularly common (Ho, Chan, and Soukoulis, 1990; Johnson and Joannopoulos, 2001).

The operators $\nabla \times \nabla$ and $\nabla \times \epsilon_r^{-1}(\mathbf{r})\nabla$ are self-adjoint and, therefore, the fields satisfy orthogonality relations given by[21]

$$\int d\mathbf{r} \mathbf{H}_{n\mathbf{k}}^*(\mathbf{r}) \cdot \mathbf{H}_{n'\mathbf{k}'}(\mathbf{r}) = \delta_{nn'}\delta(\mathbf{k} - \mathbf{k}'), \tag{143}$$

$$\int d\mathbf{r} \epsilon_r(\mathbf{r}) \mathbf{E}_{n\mathbf{k}}^*(\mathbf{r}) \cdot \mathbf{E}_{n'\mathbf{k}'}(\mathbf{r}) = \delta_{nn'}\delta(\mathbf{k} - \mathbf{k}'). \tag{144}$$

Leung (1993) first suggested that transforming to a basis of Wannier functions localized in real space would be advantageous for computational efficiency, especially when dealing with defects in photonic crystals which, using conventional methods, require very large supercells for convergence. Although of great formal importance for justifying the existence of a suitable localized basis, and hence the tight-binding approach, the nonuniqueness of the transformation between Bloch states and Wannier functions caused difficulties. As a result, early work was limited to the case of single, isolated bands (Leung, 1993; Konotop, 1997) or composite bands in which the matrix elements $U_{mn}^{(\mathbf{k})}$ were treated as parameters to fit the tight-binding band structure to the plane-wave result.

The formalism for obtaining maximally localized Wannier functions, however, removed this obstacle and several applications of MLWFs to calculating the properties of photonic crystals have been reported since, in both two-dimensional (Garcia-Martin *et al.*, 2003; Whittaker and Croucher, 2003; Jiao, Fan, and Miller, 2006) and three-dimensional (Takeda, Chutinan, and John, 2006) photonic crystal structures, as well as for the case of entangled bands (Hermann *et al.*, 2008) [see Busch *et al.* (2003) for an early review].

Typically one chooses to solve for either the electric field $\mathbf{E}_{n\mathbf{k}}$ or the magnetic field $\mathbf{H}_{n\mathbf{k}}$. Once the Bloch states for the periodic crystal are obtained, a basis of magnetic or electric field Wannier functions may be constructed using the usual definition, e.g., for the magnetic field

$$\mathbf{W}_{n\mathbf{R}}^{(\mathbf{H})}(\mathbf{r}) = \frac{V}{(2\pi)^3} \int_{\text{BZ}} d\mathbf{k} \, e^{-i\mathbf{k} \cdot \mathbf{R}} \sum_m U_{mn}^{(\mathbf{k})} \mathbf{H}_{m\mathbf{k}}(\mathbf{r}), \tag{145}$$

satisfying orthogonality relations

$$\int d\mathbf{r} \mathbf{W}_{n\mathbf{R}}^{(\mathbf{H})*} \cdot \mathbf{W}_{n'\mathbf{R}'}^{(\mathbf{H})} = \delta_{nn'}\delta_{\mathbf{R}\mathbf{R}'}, \tag{146}$$

where the unitary transformation $U_{mn}^{(\mathbf{k})}$ is chosen in the same way described in Sec. II such that the sum of the quadratic spreads of the Wannier functions is minimized, i.e., such that the Wannier functions are maximally localized.

Concentrating on the magnetic field, it can be expanded in the basis of Wannier functions with some expansion coefficients $c_{n\mathbf{R}}$,

$$\mathbf{H}(\mathbf{r}) = \sum_{n\mathbf{R}} c_{n\mathbf{R}} \mathbf{W}_{n\mathbf{R}}^{(\mathbf{H})}(\mathbf{r}), \tag{147}$$

---

[21]The notation $\mathbf{A} \cdot \mathbf{B} = \sum_{i=1}^3 A_i B_i$, and denotes the scalar product of the vectors $\mathbf{A}$ and $\mathbf{B}$, with Cartesian components $\{A_i\}$ and $\{B_i\}$, respectively.

which on substitution into Eq. (142) gives the tight-binding representation of the wave equation for the magnetic field in the Wannier-function basis.

The utility of the approach becomes evident when considering the presence of a defect in the dielectric lattice such that $\epsilon_r(\mathbf{r}) \to \epsilon_r(\mathbf{r}) + \delta\epsilon(\mathbf{r})$. The magnetic field wave equations become

$$\nabla \times ([\epsilon_r^{-1}(\mathbf{r}) + \Delta^{-1}(\mathbf{r})]\nabla \times \mathbf{H}(\mathbf{r})) = \frac{\omega^2}{c^2}\mathbf{H}(\mathbf{r}), \quad (148)$$

where

$$\Delta(\mathbf{r}) = \frac{-\delta\epsilon(\mathbf{r})}{\epsilon_r(\mathbf{r})[\epsilon_r(\mathbf{r}) + \delta\epsilon(\mathbf{r})]}. \quad (149)$$

Using the Wannier functions from the defect-free calculation as a basis in which to expand $\mathbf{H}(\mathbf{r})$, as in Eq. (147), the wave equations may be written in matrix form

$$\sum_{n'\mathbf{R}'}(A_{nn'}^{\mathbf{R}\mathbf{R}'} + B_{nn'}^{\mathbf{R}\mathbf{R}'})c_{n'\mathbf{R}'} = \frac{\omega^2}{c^2}c_{n\mathbf{R}}, \quad (150)$$

where

$$A_{nn'}^{\mathbf{R}\mathbf{R}'} = \frac{V}{(2\pi)^3}\int_{\text{BZ}} d\mathbf{k}\, e^{i\mathbf{k}\cdot(\mathbf{R}-\mathbf{R}')}\sum_m U_{nm}^{(\mathbf{k})\dagger}\left(\frac{\omega_{m\mathbf{k}}}{c}\right)^2 U_{mn'}^{(\mathbf{k})} \quad (151)$$

and

$$B_{nn'}^{\mathbf{R}\mathbf{R}'} = \int d\mathbf{r}\,\Delta(\mathbf{r})[\nabla \times \mathbf{W}_{n\mathbf{R}}(\mathbf{r})]^* \cdot [\nabla \times \mathbf{W}_{n'\mathbf{R}'}(\mathbf{r})]. \quad (152)$$

Because of the localization and compactness of the basis, these matrix equations may be solved efficiently to find frequencies of localized cavity modes, dispersion relations for waveguides, and the transmission and reflection properties of complex waveguide structures. Figure 35, for example, shows the photonic band structure for a three-dimensional photonic crystal structure with a two-dimensional defect.

C. Cold atoms in optical lattices

A good 70 years after Albert Einstein predicted that a system of noninteracting bosons would undergo a phase transition to a new state of matter in which there is macroscopic occupation of the lowest energy quantum state, major achievements in laser cooling and evaporative cooling of atoms enabled the first experimental realizations of Bose-Einstein condensation (BEC) (Anderson *et al.*, 1995; Bradley *et al.*, 1995; Davis *et al.*, 1995) and the award of Nobel prizes in 1997 and 2001. Since then, the study of cold atoms trapped in optical lattices has flourished. For reviews see Morsch and Oberthaler (2006) and Bloch, Dalibard, and Zwerger (2008).

Ultracold atoms trapped in optical lattices provide a versatile alternative to electrons in crystal lattices for the study of quantum phenomena. Indeed, they have a number of advantages over the solid state in this respect, such as the absence of lattice defects, the absence of a counterpart to the electron-phonon interaction, and the ability to control precisely both the nature of the interatomic interactions and the depth and periodicity of the optical lattice potential.
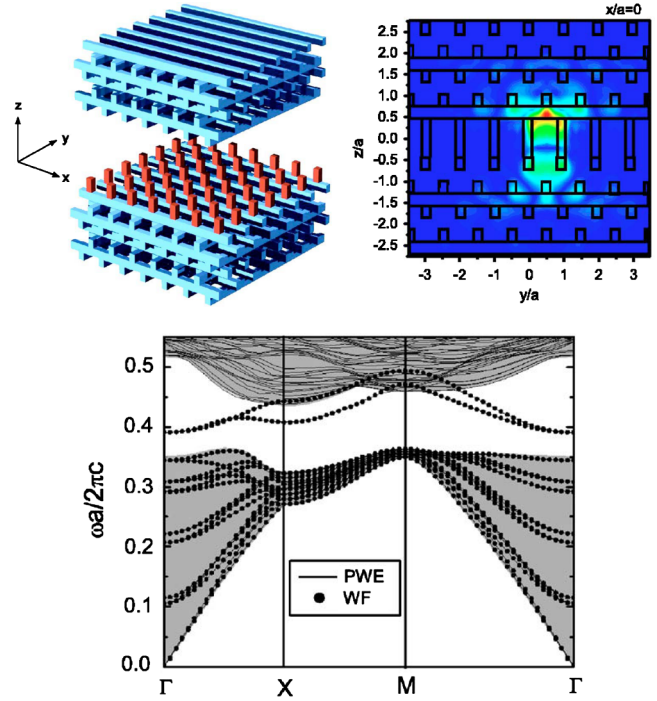

FIG. 35 (color online).   Photonic band structure (bottom) of the 3D Si woodpile structure intercalated with a 2D layer consisting of a square lattice of square rods (top left). Solid lines indicate the photonic band structure calculated by the plane-wave expansion method, and points indicate that reproduced by the MLWFs. Shaded regions indicate the photonic band structure of the woodpile projected onto the 2D $\mathbf{k}_\parallel$ space. The square rods in the 2D layer are chosen to structurally match the woodpile. The thickness of the layer is $0.8a$, where a is the lattice parameter of the woodpile structure. Top right: Absolute value of the 17th MLWF of the magnetic field in the y-z plane. Adapted from Takeda, Chutinan, and John, 2006.

The second-quantized Hamiltonian for a system of N weakly interacting bosons of zero spin and mass m in a (periodic) external potential $V_0(\mathbf{r}) = V_0(\mathbf{r} + \mathbf{R})$ is given by (Yukalov, 2009)

$$\hat{\mathcal{H}} = \int d\mathbf{r}\,\hat{\Psi}^\dagger(\mathbf{r})\left[-\frac{\hbar^2}{2m}\nabla^2 + V_0(\mathbf{r})\right]\hat{\Psi}(\mathbf{r})$$
$$+ \frac{g}{2}\int d\mathbf{r}\,\hat{\Psi}^\dagger(\mathbf{r})\hat{\Psi}^\dagger(\mathbf{r})\hat{\Psi}(\mathbf{r})\hat{\Psi}(\mathbf{r}), \quad (153)$$

where $g = 4\pi a_s \hbar^2/m$, it is assumed that the atoms interact via a short-range pseudopotential with a_s as the s-wave scattering length, and $\hat{\Psi}(\mathbf{r})$ and $\hat{\Psi}^\dagger(\mathbf{r})$ are bosonic field operators obeying canonical commutation relations (Fetter and Walecka, 2003).

In a Bose-Einstein condensate, wherein the condensate particle densities are typically of the order of 10^{14} cm^{-3} or more, the mean-field limit of this Hamiltonian is usually taken, which leads to the Gross-Pitaevskii equation, also known as the nonlinear Schrödinger equation (NLSE),

$$i\hbar\frac{\partial}{\partial t}\varphi(\mathbf{r}, t) = \left[-\frac{\hbar^2}{2m} + V_0(\mathbf{r}) + g|\varphi(\mathbf{r}, t)|^2\right]\varphi(\mathbf{r}, t). \quad (154)$$

$\varphi(\mathbf{r}, t)$ is the condensate wave function, the squared norm of which gives the condensate density. The Gross-Pitaevskii equation has been used with remarkable success in the study of BEC (Leggett, 2001).

As shown, for example, by Alfimov *et al.* (2002), a basis of Wannier functions, localized to each site α of the optical lattice, may be used to expand the condensate wave function,

$$\varphi(x, t) = \sum_{n, \alpha} c_{n\alpha}(t) w_{n\alpha}(x). \tag{155}$$

The Wannier functions are related to the Bloch eigenstates $\psi_{nk}(x)$ of the eigenvalue equation

$$\left[-\frac{d^2}{dx^2} + V_0(x) \right] \psi_{nk}(x) = \epsilon_{nk} \psi_{nk}(x) \tag{156}$$

by the usual Wannier transformation

$$w_{n\alpha}(x) = \frac{L}{2\pi} \int_{\text{BZ}} dk e^{i\phi_n(k)} e^{-ik\alpha L} \psi_{nk}(x). \tag{157}$$

Substituting Eq. (155) into Eq. (154) leads to a tight-binding formulation known as the discrete nonlinear Schrödinger equation (DNLSE),

$$i\frac{d}{dt} c_{n\alpha} = \sum_{\beta} c_{n\beta} \tilde{\epsilon}_{n, \alpha-\beta} + \sum_{\beta, \gamma, \eta} \sum_{i, j, k} c_{i\beta}^* c_{j\gamma} c_{k\eta} U_{nijk}^{\alpha\beta\gamma\eta}, \tag{158}$$

where

$$\tilde{\epsilon}_{n\alpha} = \frac{L}{2\pi} \int_{\text{BZ}} dk e^{-ik\alpha L} \epsilon_{nk}, \tag{159}$$

and the interaction matrix is given by

$$U_{nijk}^{\alpha\beta\gamma\eta} = g \int dx w_{n\alpha}(x) w_{i\beta}(x) w_{j\gamma}(x) w_{k\eta}(x). \tag{160}$$

Truncating the first term on the right-hand side of Eq. (158) to nearest neighbors only, and the second term to on-site ($\alpha = \beta = \gamma = \eta$) terms within a single band ($n = i = j = k$) results in the usual tight-binding description (Chiofalo, Polini, and Tosi, 2000; Trombettoni and Smerzi, 2001),

$$i\frac{d}{dt} c_{n\alpha} = c_{n\alpha} \tilde{\epsilon}_{n0} + \tilde{\epsilon}_{n1}(c_{n,\alpha-1} + c_{n,\alpha+1})$$
$$+ U_{nnnn}^{\alpha\alpha\alpha\alpha} |c_{n\alpha}|^2 c_{n\alpha}. \tag{161}$$

As pointed out by Alfimov *et al.* (2002), using a WF basis enables the range and type of interactions encapsulated in the DNLSE to be systematically controlled and improved. For the most part, however, WFs have been used in the context of the NLSE in order to carry out formal derivations and to justify the use of empirical or semiempirical tight-binding models.

An interesting analogy with electrons in atomic lattices manifests itself when the filling of sites in the optical lattice is low and hence particle correlations need to be accounted for more rigorously. This is done via the Bose-Hubbard model, developed by Fisher *et al.* (1989) in the context of ^{4}He, and first applied to cold atoms in optical lattices by Jaksch *et al.* (1998). The Bose-Hubbard Hamiltonian is derived from Eq. (153) by expanding the boson field operator in terms of WFs of a single band, localized at the lattice sites,

$$\hat{\Psi} = \sum_{\alpha} \hat{b}_\alpha w_\alpha(\mathbf{r}), \tag{162}$$

where the bosonic particle creation and annihilation operators $\hat{b}_\alpha$ and $\hat{b}_\alpha^\dagger$, respectively, satisfy the usual commutation rules. This, on approximation to nearest-neighbor coupling and on-site-only interactions, results in the standard Bose-Hubbard Hamiltonian (Jaksch *et al.*, 1998)

$$\hat{H}_{\text{BH}} = -J \sum_{\langle \alpha, \beta \rangle} \hat{b}_\alpha^\dagger \hat{b}_\beta + \frac{U}{2} \sum_\alpha \hat{n}_\alpha(\hat{n}_\alpha - 1), \tag{163}$$

where $\hat{n}_\alpha = \hat{b}_\alpha^\dagger \hat{b}_\alpha$ is the number operator for lattice site α, and the nearest-neighbor hopping and on-site repulsion parameters are given by

$$J = -\int d\mathbf{r} w_0(\mathbf{r}) \left[-\frac{\hbar^2}{2m} \nabla^2 + V_0(\mathbf{r}) \right] w_1(\mathbf{r}) \tag{164}$$

and

$$U = g \int d\mathbf{r} |w(\mathbf{r})|^4, \tag{165}$$

which may be calculated explicitly using WFs constructed from Bloch eigenstates (Vaucher *et al.*, 2007; Shotter, Trypogeorgos, and Foot, 2008). The Bose-Hubbard model is the bosonic analog to the Hubbard model for fermions. As in the latter case, the behavior of the model depends on the competition between hopping (J) and on-site (U) energies which determines whether the system is in a superfluid or a Mott insulator phase.

Finally, we note that in work that is closely related to, and combines elements from ideas developed in both photonic crystals and cold atoms, WFs have also been used to represent polaritons in coupled cavity arrays, a class of systems that serves as another experimental realization of the Bose-Hubbard model (Hartmann, Brandão, and Plenio, 2006, 2008).

IX. SUMMARY AND PROSPECTS

In this review, we summarized methods for constructing WFs to represent electrons in periodic solids or other extended systems. While several methods have been surveyed, our emphasis has been on the one of Marzari and Vanderbilt (1997), essentially the generalization of the approach of Foster and Boys (Boys, 1960, 1966; Foster and Boys, 1960a, 1960b) to periodic systems, in which the gauge freedom is resolved by minimizing the sum of the quadratic spreads of the WFs. The widespread adoption of this approach is reflected in the fact that it has been incorporated as a feature into a large number of modern first-principles electronic-structure code packages including QUANTUM ESPRESSO (Giannozzi *et al.*, 2009), ABINIT (Gonze *et al.*, 2009), FLEUR (Freimuth *et al.*, 2008), WIEN2K (Schwarz, Blaha, and Madsen, 2002; Kuneš *et al.*, 2010), SIESTA (Soler *et al.*, 2002; Korytár *et al.*, 2010), and VASP (Kresse and Furthmüller, 1996; Franchini *et al.*, 2012). In the above cases this has been done by providing an interface to the WANNIER90 package (Mostofi *et al.*, 2008), an open-source postprocessing code, offering most of the capabilities described in this review. Other efforts have also seen the implementation of MLWFs in CPMD (CPMD, 1990), GPAW

(Enkovaara *et al.*, 2010), OPENMX (OPENMX, 2011), and WANT (Calzolari *et al.*, 2004; Ferretti, Bonferroni, Calzolari, and Nardelli, 2005), this latter, and WANNIER90, also allowing for quantum-transport calculations.

After an initial wave of applications increased the visibility of WFs in the community and demonstrated their utility for a variety of applications, other methods for constructing WFs were also developed, as discussed in Secs. II and III. For some purposes, e.g., for many plane-wave based LDA + U and DMFT calculations, methods based on simple projection onto trial orbitals proved sufficient. Methods tuned specifically to Γ-point sampling of the BZ for supercell calculations also became popular. And, as surveyed briefly in Sec. VIII, the construction and application of WFs was also extended to periodic systems outside the electronic-structure context, e.g., to phonons, photonic crystals, and cold-atom optical lattices.

Still, the vast majority of applications of WF methods have been to electronic-structure problems. The breadth of such applications can be appreciated by reviewing the topics covered in Secs. IV, V, VI, and VII. Very broadly, these fall into three categories: investigations into the nature of chemical bonding (and, in complex systems such as liquids, the statistics of chemical bonding), as discussed in Sec. IV; applications that take advantage of the natural ability of WFs and WF charge centers to describe dipolar and orbital magnetization phenomena in dielectric, ferroelectric, magnetic, and magnetoelectric materials, as reviewed in Sec. V; and the use of WFs as basis functions, as surveyed in Secs. VI and VII.

Today these methods find applications in many topical areas including investigations into novel superconductors, multiferroics, and topological insulators. The importance of WFs is likely to grow in response to future trends in computing, which are clearly moving in the direction of more massive parallelization based on algorithms that can take advantage of real-space partitioning. This feature of WFs should also facilitate their adoption in formulating new beyond-DFT methods in which many-body interactions are included in a real-space framework. Thus, the growing pressures for increased efficiency and accuracy are likely to elevate the importance of WF-based methods in coming years. Overall, one can look forward to continued innovation in the development and application of WF-based methods to a wide variety of problems in modern condensed-matter theory.

REFERENCES

Åberg, D., B. Sadigh, and P. Erhart, 2012, Phys. Rev. B **85**, 125134.

Abu-Farsakh, H., and A. Qteish, 2007, Phys. Rev. B **75**, 085201.

Aguado, A., L. Bernasconi, S. Jahn, and P. A. Madden, 2003, Faraday Discuss. **124**, 171.

Aguado, A., L. Bernasconi, and P. A. Madden, 2003, J. Chem. Phys. **118**, 5704.

Alber, F., G. Folkers, and P. Carloni, 1999, J. Phys. Chem. B **103**, 6121.

Alfè, D., and M. J. Gillan, 2004, J. Phys. Condens. Matter **16**, L305.

Alfimov, G. L., P. G. Kevrekidis, V. V. Konotop, and M. Salerno, 2002, Phys. Rev. E **66**, 046608.

Amadon, B., F. Lechermann, A. Georges, F. Jollet, T. O. Wehling, and A. I. Lichtenstein, 2008, Phys. Rev. B **77**, 205112.

Ambrosetti, A., and P. L. Silvestrelli, 2012, Phys. Rev. B **85**, 073101.

Anantram, M. P., and T. R. Govindan, 1998, Phys. Rev. B **58**, 4882.

Andersen, O. K., and T. Saha-Dasgupta, 2000, Phys. Rev. B **62**, R16 219.

Anderson, M. H., J. R. Ensher, M. R. Matthews, C. E. Wieman, and E. A. Cornell, 1995, Science **269**, 198.

Anderson, P. W., 1961, Phys. Rev. **124**, 41.

Anderson, P. W., 1968, Phys. Rev. Lett. **21**, 13.

Andersson, Y., D. C. Langreth, and B. I. Lundqvist, 1996, Phys. Rev. Lett. **76**, 102.

Andrinopoulos, L., N. D. M. Hine, and A. A. Mostofi, 2011, J. Chem. Phys. **135**, 154105.

Anisimov, V. I., A. V. Kozhevnikov, M. A. Korotin, A. V. Lukoyanov, and D. A. Khafizullin, 2007, J. Phys. Condens. Matter **19**, 106206.

Anisimov, V. I., I. V. Solovyev, M. A. Korotin, M. T. Czyzyk, and G. A. Sawatzky, 1993, Phys. Rev. B **48**, 16929.

Anisimov, V. I., J. Zaanen, and O. K. Andersen, 1991, Phys. Rev. B **44**, 943.

Anisimov, V. I., *et al.*, 2005, Phys. Rev. B **71**, 125119.

Artacho, E., and L. Miláns del Bosch, 1991, Phys. Rev. A **43**, 5770.

Aryasetiawan, F., and O. Gunnarsson, 1998, Rep. Prog. Phys. **61**, 237.

Aryasetiawan, F., M. Imada, A. Georges, G. Kotliar, S. Biermann, and A. I. Lichtenstein, 2004, Phys. Rev. B **70**, 195104.

Ashcroft, N. W., and N. D. Mermin, 1976, *Solid State Physics* (Saunders, Philadelphia, PA).

Bader, R. F. W., 1991, Chem. Rev. **91**, 893.

Bako, I., J. Hutter, and G. Palinkas, 2002, J. Chem. Phys. **117**, 9838.

Baranek, P., C. M. Zicovich-Wilson, C. Roetti, R. Orlando, and R. Dovesi, 2001, Phys. Rev. B **64**, 125102.

Baroni, S., S. de Gironcoli, A. D. Corso, and P. Gianozzi, 2001, Rev. Mod. Phys. **73**, 515.

Baroni, S., and P. Giannozzi, 1992, Europhys. Lett. **17**, 547.

Becke, A., and K. Edgecombe, 1990, J. Chem. Phys. **92**, 5397.

Becke, A. D., 1993, J. Chem. Phys. **98**, 1372.

Benoit, D. M., D. Sebastiani, and M. Parrinello, 2001, Phys. Rev. Lett. **87**, 226401.

Berghold, G., C. J. Mundy, A. H. Romero, J. Hutter, and M. Parrinello, 2000, Phys. Rev. B **61**, 10 040.

Berlijn, T., D. Volja, and W. Ku, 2011, Phys. Rev. Lett. **106**, 077005.

Bernasconi, L., J. Blumberger, M. Sprik, and R. Vuilleumier, 2004, J. Chem. Phys. **121**, 11885.

Bernasconi, L., and P. A. Madden, 2001, J. Mol. Struct., Theochem **544**, 49.

Bernasconi, L., P. A. Madden, and M. Wilson, 2002, Phys. Chem. Comm. **5**, 1.

Bernasconi, M., P. L. Silvestrelli, and M. Parrinello, 1998, Phys. Rev. Lett. **81**, 1235.

Bhattacharjee, J., and U. V. Waghmare, 2005, Phys. Rev. B **71**, 045106.

Bhattacharjee, J., and U. V. Waghmare, 2010, Phys. Chem. Chem. Phys. **12**, 1564.

Billas, I. M. L., C. Massobrio, M. Boero, M. Parrinello, W. Branz, F. Tast, N. Malinowski, M. Heinebrodt, and T. P. Martin, 1999, J. Chem. Phys. **111**, 6787.

Bloch, I., J. Dalibard, and W. Zwerger, 2008, Rev. Mod. Phys. **80**, 885.

Blount, E. I., 1962, Solid State Phys. **13**, 305.

Blumberger, J., L. Bernasconi, I. Tavernelli, R. Vuilleumier, and M. Sprik, 2004, J. Am. Chem. Soc. **126**, 3928.

Boero, M., 2007, J. Phys. Chem. A **111**, 12 248.

Boero, M., Y. Morikawa, K. Terakura, and M. Ozeki, 2000, J. Chem. Phys. **112**, 9549.

Boero, M., M. Parrinello, S. Huffer, and H. Weiss, 2000, J. Am. Chem. Soc. **122**, 501.

Boero, M., M. Parrinello, K. Terakura, T. Ikeshoji, and C. C. Liew, 2003, Phys. Rev. Lett. **90**, 226403.

Boero, M., K. Terakura, T. Ikeshoji, C. C. Liew, and M. Parrinello, 2000a, Prog. Theor. Phys. Suppl. **138**, 259.

Boero, M., K. Terakura, T. Ikeshoji, C. C. Liew, and M. Parrinello, 2000b, Phys. Rev. Lett. **85**, 3245.

Boero, M., K. Terakura, T. Ikeshoji, C. C. Liew, and M. Parrinello, 2001, J. Chem. Phys. **115**, 2219.

Bonferroni, B., A. Ferretti, A. Calzolari, A. Ruini, M. J. Caldas, and E. Molinari, 2008, Nanotechnology **19**, 285201.

Bowler, D. R., and T. Miyazaki, 2012, Rep. Prog. Phys. **75**, 036503.

Boykin, T. B., 1995, Phys. Rev. B **52**, 16 317.

Boys, S. F., 1960, Rev. Mod. Phys. **32**, 296.

Boys, S. F., 1966, in *Quantum Theory of Atoms, Molecules, and the Solid State*, edited by P.-O. Löwdin (Academic Press, New York), p. 253.

Bradley, C. C., C. A. Sackett, J. J. Tollett, and R. G. Hulet, 1995, Phys. Rev. Lett. **75**, 1687.

Brandbyge, M., J. L. Mozos, P. Ordejón, J. Taylor, and K. Stokbro, 2002, Phys. Rev. B **65**, 165401.

Brouder, C., G. Panati, M. Calandra, C. Mourougane, and N. Marzari, 2007, Phys. Rev. Lett. **98**, 046402.

Brown, L. D., D. A. Kleier, and W. N. Lipscomb, 1977, J. Am. Chem. Soc. **99**, 6787.

Bucher, D., and S. Kuyucak, 2008, J. Phys. Chem. B **112**, 10 786.

Buongiorno Nardelli, M., J.-L. Fattebert, and J. Bernholc, 2001, Phys. Rev. B **64**, 245423.

Busch, K., S. F. Mingaleev, A. Garcia-Martin, M. Schillinger, and D. Hermann, 2003, J. Phys. Condens. Matter **15**, R1233.

Buth, C., U. Birkenheuer, M. Albrecht, and P. Fulde, 2005, Phys. Rev. B **72**, 195107.

Calandra, M., G. Profeta, and F. Mauri, 2010, Phys. Rev. B **82**, 165111.

Calzolari, A., A. Ferretti, and M. B. Nardelli, 2007, Nanotechnology **18**, 424013.

Calzolari, A., N. Marzari, I. Souza, and M. B. Nardelli, 2004, Phys. Rev. B **69**, 035108.

Cangiani, G., A. Baldereschi, M. Posternak, and H. Krakauer, 2004, Phys. Rev. B **69**, 121101.

Cantele, G., Y.-S. Lee, D. Ninno, and N. Marzari, 2009, Nano Lett. **9**, 3425.

Cao, C., P. J. Hirschfeld, and H. P. Cheng, 2008, Phys. Rev. B **77**, 220506.

Car, R., and M. Parrinello, 1985, Phys. Rev. Lett. **55**, 2471.

Cardoso, J.-F., and A. Soulomiac, 1996, SIAM J. Matrix Anal. Appl. **17**, 161.

Ceresoli, D., U. Gerstmann, A. P. Seitsonen, and F. Mauri, 2010, Phys. Rev. B **81**, 060409.

Ceresoli, D., N. Marzari, M. G. Lopez, and T. Thonhauser, 2010, Phys. Rev. B **81**, 184424.

Ceresoli, D., T. Thonhauser, D. Vanderbilt, and R. Resta, 2006, Phys. Rev. B **74**, 024408.

Chan, T. L., Y. X. Yao, C. Z. Wang, W. C. Lu, J. Li, X. F. Qian, S. Yip, and K. M. Ho, 2007, Phys. Rev. B **76**, 205119.

Chen, W., M. Sharma, R. Resta, G. Galli, and R. Car, 2008, Phys. Rev. B **77**, 245114.

Chico, L., L. X. Benedict, S. G. Louie, and M. L. Cohen, 1996, Phys. Rev. B **54**, 2600.

Chiofalo, M. L., M. Polini, and M. P. Tosi, 2000, Eur. Phys. J. D **11**, 371.

Cockayne, E., and K. M. Rabe, 1997, Phys. Rev. B **56**, 7947.

Cococcioni, M., and S. de Gironcoli, 2005, Phys. Rev. B **71**, 035105.

Coh, S., and D. Vanderbilt, 2009, Phys. Rev. Lett. **102**, 107603.

Coh, S., D. Vanderbilt, A. Malashevich, and I. Souza, 2011, Phys. Rev. B **83**, 085108.

Corsetti, F., 2012, On the properties of point defects in silicon nanostructures from *ab initio* calculations, Ph.D. thesis, (Imperial College London).

Corsetti, F., and A. A. Mostofi, 2011, Phys. Rev. B **84**, 035209.

Costanzo, F., and R. G. Della Valle, 2008, J. Phys. Chem. B **112**, 12 783.

Coudert, F. X., R. Vuilleumier, and A. Boutin, 2006, Chem. Phys. Chem. **7**, 2464.

CPMD, 1990, http://www.cpmd.org, copyright IBM Corp 1990-2008, Copyright MPI für Festkörperforschung Stuttgart 1997–2001.

Dabo, I., A. Ferretti, N. Poilvert, Y. L. Li, N. Marzari, and M. Cococcioni, 2010, Phys. Rev. B **82**, 115121.

Dabo, I., B. Kozinsky, N. E. Singh-Miller, and N. Marzari, 2008, Phys. Rev. B **77**, 115139.

Datta, S., 1995, *Electronic Transport in Moesoscopic Systems* (Cambridge University Press, Cambridge, England).

D'Auria, R., I. F. W. Kuo, and D. J. Tobias, 2008, J. Phys. Chem. A **112**, 4644.

d'Avezac, M., N. Marzari, and F. Mauri, 2007, Phys. Rev. B **76**, 165122.

Davis, K. B., M. O. Mewes, M. R. Andrews, N. J. Vandruten, D. S. Durfee, D. M. Kurn, and W. Ketterle, 1995, Phys. Rev. Lett. **75**, 3969.

Dawson, I., P. D. Bristowe, M.-H. Lee, M. C. Payne, M. D. Segall, and J. A. White, 1996, Phys. Rev. B **54**, 13 727.

Dederichs, P. H., S. Blügel, R. Zeller, and H. Akai, 1984, Phys. Rev. Lett. **53**, 2512.

de Gironcoli, S., S. Baroni, and R. Resta, 1989, Phys. Rev. Lett. **62**, 2853.

Dellago, C., and M. M. Naor, 2005, Comput. Phys. Commun. **169**, 36.

des Cloizeaux, J., 1963, Phys. Rev. **129**, 554.

des Cloizeaux, J., 1964a, Phys. Rev. **135**, A685.

des Cloizeaux, J., 1964b, Phys. Rev. **135**, A698.

Dovesi, R., B. Civalleri, R. Orlando, C. Roetti, and V. R. Saunders, 2005, in *Reviews in Computational Chemistry*, Vol. 21 (Wiley, New York), p. 1.

Duffin, R. J., 1953, Duke Math. J. **20**, 233.

Duffin, R. J., and D. H. Shaffer, 1960, Duke Math. J. **27**, 581.

Dyer, P. J., and P. T. Cummings, 2006, J. Chem. Phys. **125**, 144519.

Edmiston, C., and K. Ruedenberg, 1963, Rev. Mod. Phys. **35**, 457.

Eiguren, A., and C. Ambrosch-Draxl, 2008, Phys. Rev. B **78**, 045124.

Eisenschitz, R., and F. London, 1930, Z. Phys. A **60**, 491.

Enkovaara, J., *et al.*, 2010, J. Phys. Condens. Matter **22**, 253202.

Ercolessi, F., and J. B. Adams, 1994, Europhys. Lett. **26**, 583.

Espejo, C., T. Rangel, Y. Pouillon, A. H. Romero, and X. Gonze, 2012, Comput. Phys. Commun. **183**, 480.

Essin, A. M., J. E. Moore, and D. Vanderbilt, 2009, Phys. Rev. Lett. **102**, 146805.

Essin, A. M., A. M. Turner, J. E. Moore, and D. Vanderbilt, 2010, Phys. Rev. B **81**, 205104.

Evarestov, R. A., V. P. Smirnov, and D. E. Usvyat, 2003, Solid State Commun. **127**, 423.

Evarestov, R. A., V. P. Smirnov, and D. E. Usvyat, 2004, Int. J. Quantum Chem. **96**, 95.

Fabris, S., S. de Gironcoli, S. Baroni, G. Vicario, and G. Balducci, 2005, Phys. Rev. B **71**, 041102.

Fang, Z., N. Nagaosa, K. Takahashi, A. Asamitsu, R. Matthieu, T. Ogasawara, H. Yamada, M. Kawasaki, Y. Tokura, and K. Terakura, 2003, Science **302**, 92.

Faralli, C., M. Pagliai, G. Cardini, and V. Schettino, 2006, J. Phys. Chem. B **110**, 14 923.

Fattebert, J.-L., and M. Buongiorno Nardelli, 2003, in *Special Volume: Computational Chemistry*, edited by C. L. Bris, Vol. X of Handbook of Numerical Analysis (North-Holland, Amsterdam), p. 571.

Fernandez, P., A. Dal Corso, and A. Baldereschi, 1998, Phys. Rev. B **58**, R7480.

Fernandez, P., A. Dal Corso, F. Mauri, and A. Baldereschi, 1997, Phys. Rev. B **55**, R1909.

Ferretti, A., B. Bonferroni, A. Calzolari, and M. B. Nardelli, 2005, http://www.wannier-transport.org.

Ferretti, A., A. Calzolari, B. Bonferroni, and R. Di Felice, 2007, J. Phys. Condens. Matter **19**, 036215.

Ferretti, A., A. Calzolari, R. Di Felice, and F. Manghi, 2005, Phys. Rev. B **72**, 125114.

Ferretti, A., A. Calzolari, R. Di Felice, F. Manghi, M. J. Caldas, M. B. Nardelli, and E. Molinari, 2005, Phys. Rev. Lett. **94**, 116802.

Fetter, A. L., and J. D. Walecka, 2003, *Quantum Theory of Many-Particle Systems* (Dover Publications Inc., New York), Chap. 1.

Fisher, D. S., and P. A. Lee, 1981, Phys. Rev. B **23**, 6851.

Fisher, M. P. A., P. B. Weichman, G. Grinstein, and D. S. Fisher, 1989, Phys. Rev. B **40**, 546.

Fitzhenry, P., M. M. M. Bilek, N. A. Marks, N. C. Cooper, and D. R. McKenzie, 2003, J. Phys. Condens. Matter **15**, 165.

Flury, B. N., and W. Gautschi, 1986, SIAM J. Sci. Stat. Comput. **7**, 169.

Fornari, M., N. Marzari, M. Peressi, and A. Baldereschi, 2001, Comput. Mater. Sci. **20**, 337.

Foster, J. M., and S. F. Boys, 1960a, Rev. Mod. Phys. **32**, 300.

Foster, J. M., and S. F. Boys, 1960b, Rev. Mod. Phys. **32**, 303.

Foulkes, W. M. C., L. Mitas, R. J. Needs, and G. Rajagopal, 2001, Rev. Mod. Phys. **73**, 33.

Franchini, C., R. Kovacik, M. Marsman, S. S. Murthy, J. He, C. Ederer, and G. Kresse, 2012, J. Phys. Condens. Matter **24**, 235602.

Frederiksen, T., M. Paulsson, M. Brandbyge, and A.-P. Jauho, 2007, Phys. Rev. B **75**, 205413.

Freimuth, F., S. Blügel, and Y. Mokrousov, 2010, Phys. Rev. Lett. **105**, 246602.

Freimuth, F., Y. Mokrousov, D. Wortmann, S. Heinze, and S. Blügel, 2008, Phys. Rev. B **78**, 035120.

Gaigeot, M. P., M. Martinez, and R. Vuilleumier, 2007, Mol. Phys. **105**, 2857.

Gaigeot, M. P., and M. Sprik, 2003, J. Phys. Chem. B **107**, 10 344.

Gaigeot, M. P., R. Vuilleumier, M. Sprik, and D. Borgis, 2005, J. Chem. Theory Comput. **1**, 772.

Galli, G., 1996, Curr. Opin. Solid State Mater. Sci. **1**, 864.

Galli, G., and M. Parrinello, 1992, Phys. Rev. Lett. **69**, 3547.

Garcia-Martin, A., D. Hermann, F. Hagmann, K. Busch, and P. Wolfle, 2003, Nanotechnology **14**, 177.

Gervasio, F. L., P. Carloni, and M. Parrinello, 2002, Phys. Rev. Lett. **89**, 108102.

Ghosez, P., and X. Gonze, 2000, J. Phys. Condens. Matter **12**, 9179.

Ghosez, P., X. Gonze, P. Lambin, and J.-P. Michenaud, 1995, Phys. Rev. B **51**, 6765.

Giannozzi, P., *et al.*, 2009, J. Phys. Condens. Matter **21**, 395502.

Giustino, F., M. L. Cohen, and S. G. Louie, 2007, Phys. Rev. B **76**, 165108.

Giustino, F., M. L. Cohen, and S. G. Louie, 2008, Nature (London) **452**, 975.

Giustino, F., S. G. Louie, and M. L. Cohen, 2010, Phys. Rev. Lett. **105**, 265501.

Giustino, F., and A. Pasquarello, 2005, Phys. Rev. B **71**, 144104.

Giustino, F., and A. Pasquarello, 2006, Phys. Rev. Lett. **96**, 216403.

Giustino, F., P. Umari, and A. Pasquarello, 2003, Phys. Rev. Lett. **91**, 267601.

Giustino, F., J. R. Yates, I. Souza, M. L. Cohen, and S. G. Louie, 2007, Phys. Rev. Lett. **98**, 047005.

Goedecker, S., 1998, Phys. Rev. B **58**, 3501.

Goedecker, S., 1999, Rev. Mod. Phys. **71**, 1085.

Goedecker, S., T. Deutsch, and L. Billard, 2002, Phys. Rev. Lett. **88**, 235501.

Gonze, X., *et al.*, 2009, Comput. Phys. Commun. **180**, 2582.

Graf, M., and P. Vogl, 1995, Phys. Rev. B **51**, 4940.

Grimvall, G., 1981, *The Electron-Phonon Interaction in Metals* (North-Holland, New York).

Grossman, J. C., E. Schwegler, E. W. Draeger, F. Gygi, and G. Galli, 2004, J. Chem. Phys. **120**, 300.

Grosso, G., and G. P. Parravicini, 2000, *Solid State Physics* (Academic Press, New York).

Gygi, F., J. L. Fattebert, and E. Schwegler, 2003, Comput. Phys. Commun. **155**, 1.

Haldane, F. D. M., 1988, Phys. Rev. Lett. **61**, 2015.

Hamann, D. R., and D. Vanderbilt, 2009, Phys. Rev. B **79**, 045109.

Harrison, W. A., 1980, *Solid State Theory* (Dover, New York).

Hartmann, M. J., F. Brandão, and M. B. Plenio, 2008, Laser Photonics Rev. **2**, 527.

Hartmann, M. J., F. G. S. L. Brandão, and M. B. Plenio, 2006, Nature Phys. **2**, 849.

Hasan, M. Z., and C. L. Kane, 2010, Rev. Mod. Phys. **82**, 3045.

Hasan, M. Z., and J. E. Moore, 2011, Annu. Rev. Condens. Matter Phys. **2**, 55.

He, L. X., and D. Vanderbilt, 2001, Phys. Rev. Lett. **86**, 5341.

Heine, V., 1980, in *Solid State Physics*, edited by H. Ehrenreich, F. Seitz, and D. Turnbull (Academic Press, New York), Vol. 35, p. 1.

Held, K., 2007, Adv. Phys. **56**, 829.

Held, K., O. K. Andersen, M. Feldbacher, A. Yamasaki, and Y. F. Yang, 2008, J. Phys. Condens. Matter **20**, 064202.

Hermann, D., M. Schillinger, S. F. Mingaleev, and K. Busch, 2008, J. Opt. Soc. Am. B **25**, 202.

Hernández, E., and M. J. Gillan, 1995, Phys. Rev. B **51**, 10 157.

Hernández, E., M. J. Gillan, and C. M. Goringe, 1996, Phys. Rev. B **53**, 7147.

Heuft, J. M., and E. J. Meijer, 2005, J. Chem. Phys. **122**, 094501.

Hierse, W., and E. B. Stechel, 1994, Phys. Rev. B **50**, 17 811.

Hine, N. D. M., and W. M. C. Foulkes, 2007, J. Phys. Condens. Matter **19**, 506212.

Hirshfeld, F. L., 1977, Theor. Chim. Acta **44**, 129.

Ho, K. M., C. T. Chan, and C. M. Soukoulis, 1990, Phys. Rev. Lett. **65**, 3152.

Hod, O., J. E. Peralta, and G. E. Scuseria, 2006, J. Phys. Chem. **125**, 114704.

Hu, S. J., and X. Hu, 2010, J. Phys. Chem. C **114**, 11614.

Hubbard, J., 1963, Proc. R. Soc. A **276**, 238.

Hurd, C. M., 1972, *The Hall Effect in Metals and Alloys* (Plenum, New York).

Iftimie, R., J. W. Thomas, and M. E. Tuckerman, 2004, J. Chem. Phys. **120**, 2169.

Ikeda, T., M. Hirata, and T. Kimura, 2005, J. Chem. Phys. **122**, 024510.

Íñiguez, J., A. Garcia, and J. M. Pérez-Mato, 2000, Phys. Rev. B **61**, 3127.

Ismail-Beigi, S., and T. A. Arias, 1999, Phys. Rev. Lett. **82**, 2127.

Jahn, S., and P. A. Madden, 2007, Phys. Earth Planet. Inter. **162**, 129.

Jahn, S., P. A. Madden, and M. Wilson, 2006, Phys. Rev. B **74**, 024112.

Jaksch, D., C. Bruder, J. I. Cirac, C. W. Gardiner, and P. Zoller, 1998, Phys. Rev. Lett. **81**, 3108.

Janak, J. F., 1978, Phys. Rev. B **18**, 7165.

Jarvis, E. A. A., and E. A. Carter, 2001, J. Phys. Chem. B **105**, 4045.

Jiang, L., S. Levchenko, and A. Rappe, 2012, Phys. Rev. Lett. **108**, 166403.

Jiao, Y., S. H. Fan, and D. A. B. Miller, 2006, IEEE J. Quantum Electron. **42**, 266.

Joannopoulos, J. D., P. R. Villeneuve, and S. H. Fan, 1997, Nature (London) **387**, 830.

John, S., 1987, Phys. Rev. Lett. **58**, 2486.

Johnson, S. G., and J. D. Joannopoulos, 2001, Opt. Express **8**, 173.

Jungwirth, P., and D. J. Tobias, 2002, J. Phys. Chem. A **106**, 379.

Karabunarliev, S., and E. R. Bittner, 2003a, J. Chem. Phys. **119**, 3988.

Karabunarliev, S., and E. R. Bittner, 2003b, J. Chem. Phys. **118**, 4291.

Kim, S., and N. Marzari, 2012, arXiv:1204.6369.

King-Smith, R. D., and D. Vanderbilt, 1993, Phys. Rev. B **47**, 1651.

King-Smith, R. D., and D. Vanderbilt, 1994, Phys. Rev. B **49**, 5828.

Kioupakis, E., P. Rinke, A. Schleife, F. Bechstedt, and C. G. Van de Walle, 2010, Phys. Rev. B **81**, 241201.

Kirchner, B., 2007, Phys. Rep. **440**, 1.

Kirchner, B., and J. Hutter, 2004, J. Chem. Phys. **121**, 5133.

Koch, E., and S. Goedecker, 2001, Solid State Commun. **119**, 105.

Kohn, W., 1959, Phys. Rev. **115**, 809.

Kohn, W., 1964, Phys. Rev. **133**, A171.

Kohn, W., 1973, Phys. Rev. B **7**, 2285.

Kohn, W., 1996, Phys. Rev. Lett. **76**, 3168.

Kohn, W., and L. J. Sham, 1965, Phys. Rev. **140**, A1133.

Konotop, V. V., 1997, J. Opt. Soc. Am. B **14**, 364.

Korotin, D., A. V. Kozhevnikov, S. L. Skornyakov, I. Leonov, N. Binggeli, V. I. Anisimov, and G. Trimarchi, 2008, Eur. Phys. J. B **65**, 91.

Korshunov, M. M., V. A. Gavrichkov, S. G. Ovchinnikov, I. A. Nekrasov, Z. V. Pchelkina, and V. I. Anisimov, 2005, Phys. Rev. B **72**, 165104.

Korytár, R., M. Pruneda, J. Junquera, P. Ordejón, and N. Lorente, 2010, J. Phys. Condens. Matter **22**, 385601.

Kotliar, G., S. Y. Savrasov, K. Haule, V. S. Oudovenko, O. Parcollet, and C. A. Marianetti, 2006, Rev. Mod. Phys. **78**, 865.

Kovacik, R., and C. Ederer, 2010, Phys. Rev. B **81**, 245108.

Krakauer, H., R. C. Yu, C. Z. Wang, K. M. Rabe, and U. V. Waghmare, 1999, J. Phys. Condens. Matter **11**, 3779.

Kreitmeir, M., H. Bertagnolli, J. J. Mortensen, and M. Parrinello, 2003, J. Chem. Phys. **118**, 3639.

Krekeler, C., B. Hess, and L. Delle Site, 2006, J. Chem. Phys. **125**, 054305.

Kresse, G., and J. Furthmüller, 1996, Phys. Rev. B **54**, 11 169.

Ku, W., T. Berlijn, and C.-C. Lee, 2010, Phys. Rev. Lett. **104**, 216401.

Ku, W., H. Rosner, W. E. Pickett, and R. T. Scalettar, 2002, Phys. Rev. Lett. **89**, 167204.

Ku, W., H. Rosner, W. E. Pickett, and R. T. Scalettar, 2003, J. Solid State Chem. **171**, 329.

Kudin, K. N., and R. Car, 2008, J. Am. Chem. Soc. **130**, 3915.

Kudin, K. N., R. Car, and R. Resta, 2007, J. Chem. Phys. **127**, 194902.

Kulik, H. J., M. Cococcioni, D. A. Scherlis, and N. Marzari, 2006, Phys. Rev. Lett. **97**, 103001.

Kulik, H. J., and N. Marzari, 2008, J. Chem. Phys. **129**, 134314.

Kuneš, J., R. Arita, P. Wissgott, A. Toschi, H. Ikeda, and K. Held, 2010, Comput. Phys. Commun. **181**, 1888.

Kuo, I. F. W., and C. J. Mundy, 2004, Science **303**, 658.

Kuo, I. F. W., C. J. Mundy, B. L. Eggimann, M. J. McGrath, J. I. Siepmann, B. Chen, J. Vieceli, and D. J. Tobias, 2006, J. Phys. Chem. B **110**, 3738.

Kuo, I. F. W., C. J. Mundy, M. J. McGrath, and J. I. Siepmann, 2008, J. Phys. Chem. C **112**, 15 412.

Kuroki, K., S. Onari, R. Arita, H. Usui, Y. Tanaka, H. Kontani, and H. Aoki, 2008, Phys. Rev. Lett. **101**, 087004.

Lambrecht, W. R. L., and O. K. Andersen, 1986, Phys. Rev. B **34**, 2439.

Landauer, R., 1970, Philos. Mag. **21**, 863.

Lechermann, F., A. Georges, A. Poteryaev, S. Biermann, M. Posternak, A. Yamasaki, and O. K. Andersen, 2006, Phys. Rev. B **74**, 125120.

Lee, D. H., and J. D. Joannopoulos, 1981, Phys. Rev. B **23**, 4988.

Lee, J. H., U. V. Waghmare, and J. J. Yu, 2008, J. Appl. Phys. **103**, 124106.

Lee, Y.-S., 2006, Electronic Structure and Quantum Conductance of Nanostructures, Ph.D. thesis (MIT).

Lee, Y.-S., and N. Marzari, 2006, Phys. Rev. Lett. **97**, 116801.

Lee, Y.-S., M. B. Nardelli, and N. Marzari, 2005, Phys. Rev. Lett. **95**, 076804.

Leggett, A. J., 2001, Rev. Mod. Phys. **73**, 307.

Léonard, F., and J. Tersoff, 1999, Phys. Rev. Lett. **83**, 5174.

Leung, K., and S. B. Rempe, 2004, J. Am. Chem. Soc. **126**, 344.

Leung, K. M., 1993, J. Opt. Soc. Am. B **10**, 303.

Li, E. Y., and N. Marzari, 2011, ACS Nano **5**, 9726.

Li, E. Y., N. Poilvert, and N. Marzari, 2011, ACS Nano **5**, 4455.

Lidorikis, E., M. M. Sigalas, E. N. Economou, and C. M. Soukoulis, 1998, Phys. Rev. Lett. **81**, 1405.

Lightstone, F. C., E. Schwegler, M. Allesch, F. Gygi, and G. Galli, 2005, Chem. Phys. Chem. **6**, 1745.

Lightstone, F. C., E. Schwegler, R. Q. Hood, F. Gygi, and G. Galli, 2001, Chem. Phys. Lett. **343**, 549.

Lim, S. H. N., D. G. McCullooch, A. R. Merchant, N. A. Marks, M. M. M. Bilek, and D. R. McKenzie, 2002, Mol. Simul. **28**, 971.

Liu, Y., H.-J. Zhang, and Y. Yao, 2009, Phys. Rev. B **79**, 245123.

Lopez, M. G., D. Vanderbilt, T. Thonhauser, and I. Souza, 2012, Phys. Rev. B **85**, 014435.

López Sancho, M. P., J. M. López Sancho, and J. Rubio, 1984, J. Phys. F **14**, 1205.

López Sancho, M. P., J. M. López Sancho, J. M. L. Sancho, and J. Rubio, 1985, J. Phys. F **15**, 851.

Löwdin, P.-O., 1951, J. Chem. Phys. **19**, 1396.

Lu, D. Y., F. Gygi, and G. Galli, 2008, Phys. Rev. Lett. **100**, 147601.

Lu, W. C., C. Z. Wang, T. L. Chan, K. Ruedenberg, and K. M. Ho, 2004, Phys. Rev. B **70**, 041101.

Madsen, G. K. H., and D. J. Singh, 2006, Comput. Phys. Commun. **175**, 67.

Makov, G., and M. C. Payne, 1995, Phys. Rev. B **51**, 4014.

Malashevich, A., I. Souza, S. Coh, and D. Vanderbilt, 2010, New J. Phys. **12**, 053032.

Maradudin, A. A., and S. H. Vosko, 1968, Rev. Mod. Phys. **40**, 1.

Markussen, T., R. Rurali, M. Brandbyge, and A.-P. Jauho, 2006, Phys. Rev. B **74**, 245313.

Martin, R. M., 2004, *Electronic Structure: Basic Theory and Practical Methods* (Cambridge University Press, Cambridge, England).

Martonak, R., C. Molteni, and M. Parrinello, 2000, Phys. Rev. Lett. **84**, 682.

Martonak, R., C. Molteni, and M. Parrinello, 2001, Comput. Mater. Sci. **20**, 293.

Marx, D., and J. Hutter, 2009, *Ab initio Molecular Dynamics: Basic Theory and Advanced Methods* (Cambridge University Press, Cambridge, England).

Marzari, N., and D. Vanderbilt, 1997, Phys. Rev. B **56**, 12 847.

Marzari, N., and D. Vanderbilt, 1998, AIP Conf. Proc. **436**, 146.

Marzari, N., D. Vanderbilt, and M. C. Payne, 1997, Phys. Rev. Lett. **79**, 1337.

Matta, C. F., R. J. Boyd, and A. Becke, 2007, Eds., *The Quantum Theory of Atoms in Molecules: From Solid State to DNA and Drug Design* (Wiley-VCH, Weinheim).

Mauri, F., G. Galli, and R. Car, 1993, Phys. Rev. B **47**, 9973.

Mauri, F., B. G. Pfrommer, and S. G. Louie, 1996, Phys. Rev. Lett. **77**, 5300.

Mauri, F., O. Zakharov, S. de Gironcoli, S. G. Louie, and M. L. Cohen, 1996, Phys. Rev. Lett. **77**, 1151.

Mazin, I. I., D. A. Papaconstantopoulos, and D. J. Singh, 2000, Phys. Rev. B **61**, 5223.

McGrath, M. J., J. I. Siepmann, I. F. W. Kuo, and C. J. Mundy, 2007, Mol. Phys. **105**, 1411.

McMahan, A. K., J. F. Annett, and R. M. Martin, 1990, Phys. Rev. B **42**, 6268.

McWeeny, R., 1960, Rev. Mod. Phys. **32**, 335.

Meregalli, V., and M. Parrinello, 2001, Solid State Commun. **117**, 441.

Minehardt, T. J., N. Marzari, R. Cooke, E. Pate, P. A. Kollman, and R. Car, 2002, Biophys. J. **82**, 660.

Miyake, T., and F. Aryasetiawan, 2008, Phys. Rev. B **77**, 085122.

Miyake, T., F. Aryasetiawan, and M. Imada, 2009, Phys. Rev. B **80**, 155134.

Miyake, T., P. H. Zhang, M. L. Cohen, and S. G. Louie, 2006, Phys. Rev. B **74**, 245213.

Mogilevtsev, D., T. A. Birks, and P. S. Russell, 1999, J. Lightwave Technol. **17**, 2078.

Molteni, C., R. Martonak, and M. Parrinello, 2001, J. Chem. Phys. **114**, 5358.

Mori-Sánchez, P., A. J. Cohen, and W. Yang, 2008, Phys. Rev. Lett. **100**, 146401.

Morsch, O., and M. Oberthaler, 2006, Rev. Mod. Phys. **78**, 179.

Mostofi, A. A., J. R. Yates, Y.-S. Lee, I. Souza, D. Vanderbilt, and N. Marzari, 2008, Comput. Phys. Commun. **178**, 685.

Mulliken, R. S., 1955, J. Chem. Phys. **23**, 1833.

Mundy, C. J., and I. F. W. Kuo, 2006, Chem. Rev. **106**, 1282.

Murray, E. D., and D. Vanderbilt, 2009, Phys. Rev. B **79**, 100102.

Nagaosa, N., J. Sinova, S. Onoda, A. H. MacDonald, and N. P. Ong, 2010, Rev. Mod. Phys. **82**, 1539.

Nakamura, K., R. Arita, Y. Yoshimoto, and S. Tsuneyuki, 2006, Phys. Rev. B **74**, 235113.

Nakhmanson, S. M., M. B. Nardelli, and J. Bernholc, 2005, Phys. Rev. B **72**, 115210.

Nardelli, M. B., 1999, Phys. Rev. B **60**, 7828.

Naumov, I., A. M. Bratkovsky, and V. Ranjan, 2009, Phys. Rev. Lett. **102**, 217601.

Nenciu, G., 1983, Commun. Math. Phys. **91**, 81.

Nenciu, G., 1991, Rev. Mod. Phys. **63**, 91.

Niu, Q., 1991, Mod. Phys. Lett. B **05**, 923.

Noel, Y., C. M. Zicovich-Wilson, B. Civalleri, P. D'Arco, and R. Dovesi, 2001, Phys. Rev. B **65**, 014111.

Noffsinger, J., F. Giustino, S. G. Louie, and M. L. Cohen, 2008, Phys. Rev. B **77**, 180507.

Noffsinger, J., F. Giustino, S. G. Louie, and M. L. Cohen, 2009, Phys. Rev. B **79**, 104511.

Noffsinger, J., F. Giustino, B. D. Malone, C.-H. Park, S. G. Louie, and M. L. Cohen, 2010, Comput. Phys. Commun. **181**, 2140.

Noffsinger, J., E. Kioupakis, C. G. V. de Walle, S. G. Louie, and M. L. Cohen, 2012, Phys. Rev. Lett. **108**, 167402.

Nunes, R. W., and X. Gonze, 2001, Phys. Rev. B **63**, 155107.

Nunes, R. W., and D. Vanderbilt, 1994, Phys. Rev. Lett. **73**, 712.

Odelius, M., B. Kirchner, and J. Hutter, 2004, J. Phys. Chem. A **108**, 2044.

Ogitsu, T., F. Gygi, J. Reed, Y. Motome, E. Schwegler, and G. Galli, 2009, J. Am. Chem. Soc. **131**, 1903.

Okada, J. T., *et al.*, 2012, Phys. Rev. Lett. **108**, 067402.

OPENMX, 2011, http://www.openmx-square.org.

Ordejón, P., D. Drabold, M. P. Grumbach, and R. M. Martin, 1993, Phys. Rev. B **48**, 14 646.

O'Regan, D. D., N. D. M. Hine, M. C. Payne, and A. A. Mostofi, 2010, Phys. Rev. B **82**, 081102(R).

O'Regan, D. D., M. C. Payne, and A. A. Mostofi, 2011, Phys. Rev. B **83**, 245124.

O'Regan, D. D., M. C. Payne, and A. A. Mostofi, 2012, Phys. Rev. B **85**, 193101.

Ortiz, G., and R. M. Martin, 1994, Phys. Rev. B **49**, 14 202.

Pagliai, M., C. Cavazzoni, G. Cardini, G. Erbacci, M. Parrinello, and V. Schettino, 2008, J. Chem. Phys. **128**, 224514.

Panati, G., 2007, Ann. Inst. Henri Poincaré **8**, 995.

Panati, G., and A. Pisante, 2011, arXiv:1112.6197.

Park, C. H., F. Giustino, M. L. Cohen, and S. G. Louie, 2007, Phys. Rev. Lett. **99**, 086804.

Park, C. H., F. Giustino, M. L. Cohen, and S. G. Louie, 2008, Nano Lett. **8**, 4229.

Park, C.-H., A. Ferretti, I. Dabo, N. Poilvert, and N. Marzari, 2011, arXiv:1108.5726.

Park, C.-H., F. Giustino, C. D. Spataru, M. L. Cohen, and S. G. Louie, 2009, Phys. Rev. Lett. **102**, 076803.

Pasquarello, A., and R. Resta, 2003, Phys. Rev. B **68**, 174302.

Pauling, L., 1960, *The Nature of the Chemical Bond* (Cornell University Press, Ithaca), 3rd ed.

Payne, M. C., M. P. Teter, D. C. Allan, T. A. Arias, and J. D. Joannopoulos, 1992, Rev. Mod. Phys. **64**, 1045.

Peelaers, H., B. Partoens, M. Giantomassi, T. Rangel, E. Goossens, G.-M. Rignanese, X. Gonze, and F. M. Peeters, 2011, Phys. Rev. B **83**, 045306.

Pendry, J. B., 1996, J. Phys. Condens. Matter **8**, 1085.

Pendry, J. B., and A. Mackinnon, 1992, Phys. Rev. Lett. **69**, 2772.

Perdew, J. P., R. G. Parr, M. Levy, and J. J. L. Balduz, 1982, Phys. Rev. Lett. **49**, 1691.

Perdew, J. P., and A. Zunger, 1981, Phys. Rev. B **23**, 5048.

Piana, S., D. Sebastiani, P. Carloni, and M. Parrinello, 2001, J. Am. Chem. Soc. **123**, 8730.

Pickard, C. J., and F. Mauri, 2001, Phys. Rev. B **63**, 245101.

Picozzi, S., K. Yamauchi, I. A. Sergienko, C. Sen, B. Sanyal, and E. Dagotto, 2008, J. Phys. Condens. Matter **20**, 434208.

Pipek, J., and P. G. Mezey, 1989, J. Chem. Phys. **90**, 4916.

Pisani, C., M. Busso, G. Capecchi, S. Casassa, R. Dovesi, L. Maschio, C. Zicovich-Wilson, and M. Schutz, 2005, J. Chem. Phys. **122**, 094113.

Posternak, M., A. Baldereschi, S. Massidda, and N. Marzari, 2002, Phys. Rev. B **65**, 184422.

Posternak, M., A. Baldereschi, E. J. Walter, and H. Krakauer, 2006, Phys. Rev. B **74**, 125113.

Posternak, M., R. Resta, and A. Baldereschi, 1994, Phys. Rev. B **50**, 8911.

Pytte, E., and J. Feder, 1969, Phys. Rev. **187**, 1077.

Qi, X.-L., T. L. Hughes, and S.-C. Zhang, 2008, Phys. Rev. B **78**, 195424.

Qian, X., J. Li, and S. Yip, 2010, Phys. Rev. B **82**, 195442.

Qian, X. F., J. Li, L. Qi, C. Z. Wang, T. L. Chan, Y. X. Yao, K. M. Ho, and S. Yip, 2008, Phys. Rev. B **78**, 245112.

Rabe, K. M., and U. V. Waghmare, 1995, Phys. Rev. B **52**, 13 236.

Rasuli, R., H. Rafii-Tabar, and A. I. Zad, 2010, Phys. Rev. B **81**, 125409.

Raugei, S., G. Cardini, and V. Schettino, 1999, J. Chem. Phys. **111**, 10 887.

Raugei, S., and M. L. Klein, 2002, J. Chem. Phys. **116**, 196.

Reboredo, F. A., and A. J. Williamson, 2005, Phys. Rev. B **71**, 121105.

Resta, R., 1992, Ferroelectrics **136**, 51.

Resta, R., 1994, Rev. Mod. Phys. **66**, 899.

Resta, R., 1998, Phys. Rev. Lett. **80**, 1800.

Resta, R., 2000, J. Phys. Condens. Matter **12**, R107.

Resta, R., 2002, J. Phys. Condens. Matter **14**, R625.

Resta, R., 2006, J. Chem. Phys. **124**, 104104.

Resta, R., 2010, J. Phys. Condens. Matter **22**, 123201.

Resta, R., and S. Sorella, 1999, Phys. Rev. Lett. **82**, 370.

Resta, R., and D. Vanderbilt, 2007, in *Physics of Ferroelectrics: A Modern Perspective*, edited by C. Ahn and K. M. Rabe, Topics in Applied Physics Vol. 105 (Springer-Verlag, Berlin), p. 31.

Rocha, A. R., M. Rossi, A. Fazzio, and A. J. R. da Silva, 2008, Phys. Rev. Lett. **100**, 176803.

Roman, E., Y. Mokrousov, and I. Souza, 2009, Phys. Rev. Lett. **103**, 097203.

Romero, A. H., P. L. Silvestrelli, and M. Parrinello, 2000, Phys. Status Solidi B **220**, 703.

Romero, A. H., P. L. Silvestrelli, and M. Parrinello, 2001, J. Chem. Phys. **115**, 115.

Rotenberg, B., M. Salanne, C. Simon, and R. Vuilleumier, 2010, Phys. Rev. Lett. **104**, 138301.

Rowley, A. J., P. Jemmer, M. Wilson, and P. A. Madden, 1998, J. Chem. Phys. **108**, 10 209.

Sagui, C., P. Pomorski, T. A. Darden, and C. Roland, 2004, J. Chem. Phys. **120**, 4530.

Saharay, M., and S. Balasubramanian, 2004, Chem. Phys. Chem. **5**, 1442.

Saito, R., G. Dresselhaus, and M. S. Dresselhaus, 1996, Phys. Rev. B **53**, 2044.

Sakakibara, H., H. Usui, K. Kuroki, R. Arita, and H. Aoki, 2010, Phys. Rev. Lett. **105**, 057003.

Salanne, M., R. Vuilleumier, P. A. Madden, C. Simon, P. Turq, and B. Guillot, 2008, J. Phys. Condens. Matter **20**, 494207.

Salvador, P., J. E. Curtis, D. J. Tobias, and P. Jungwirth, 2003, Phys. Chem. Chem. Phys. **5**, 3752.

Sánchez-Portal, D., E. Artacho, and J. Soler, 1995, Solid State Commun. **95**, 685.

Santis, L. D., and R. Resta, 2000, Surf. Sci. **450**, 126.

Sasioglu, E., A. Schindlmayr, C. Friedrich, F. Freimuth, and S. Blügel, 2010, Phys. Rev. B **81**, 054434.

Satpathy, S., and Z. Pawlowska, 1988, Phys. Status Solidi B **145**, 555.

Savin, A., O. Jepsen, J. Flad, O. K. Andersen, H. Preuss, and H. G. von Schnering, 1992, Angew. Chem., Int. Ed. Engl. **31**, 187.

Savrasov, S. Y., D. Y. Savrasov, and O. K. Andersen, 1994, Phys. Rev. Lett. **72**, 372.

Schulz, W. W., P. B. Allen, and N. Trivedi, 1992, Phys. Rev. B **45**, 10886.

Schwarz, K., P. Blaha, and G. K. H. Madsen, 2002, Comput. Phys. Commun. **147**, 71.

Schwegler, E., G. Galli, and F. Gygi, 2001, Chem. Phys. Lett. **342**, 434.

Schwegler, E., G. Galli, F. Gygi, and R. Q. Hood, 2001, Phys. Rev. Lett. **87**, 265501.

Scipioni, R., D. A. Schmidt, and M. Boero, 2009, J. Chem. Phys. **130**, 024502.

Sebastiani, D., 2003, Mod. Phys. Lett. B **17**, 1301.

Sebastiani, D., G. Goward, I. Schnell, and M. Parrinello, 2002, Comput. Phys. Commun. **147**, 707.

Sebastiani, D., and M. Parrinello, 2001, J. Phys. Chem. A **105**, 1951.

Seeman, K. M., *et al.*, 2010, Phys. Rev. Lett. **104**, 076402.

Segall, M. D., R. Shah, C. J. Pickard, and M. C. Payne, 1996, Phys. Rev. B **54**, 16 317.

Selloni, A., P. Carnevali, R. Car, and M. Parrinello, 1987, Phys. Rev. Lett. **59**, 823.

Sgiarovello, C., M. Peressi, and R. Resta, 2001, Phys. Rev. B **64**, 115202.

Shaltaf, R., T. Rangel, M. Gruning, X. Gonze, G. M. Rignanese, and D. R. Hamann, 2009, Phys. Rev. B **79**, 195101.

Sharma, M., R. Resta, and R. Car, 2005, Phys. Rev. Lett. **95**, 187401.

Sharma, M., R. Resta, and R. Car, 2007, Phys. Rev. Lett. **98**, 247401.

Sharma, M., Y. D. Wu, and R. Car, 2003, Int. J. Quantum Chem. **95**, 821.

Shelley, M., and A. A. Mostofi, 2011, Europhys. Lett. **94**, 67001.

Shelley, M., N. Poilvert, A. A. Mostofi, and N. Marzari, 2011, Comput. Phys. Commun. **182**, 2174.

Shi, J., G. Vignale, D. Xiao, and Q. Niu, 2007, Phys. Rev. Lett. **99**, 197202.

Shi, N., and R. Ramprasad, 2006, Phys. Rev. B **74**, 045318.

Shi, N., and R. Ramprasad, 2007, Appl. Phys. Lett. **91**, 242906.

Shotter, M., D. Trypogeorgos, and C. Foot, 2008, Phys. Rev. A **78**, 051602.

Silvestrelli, P. L., 1999, Phys. Rev. B **59**, 9703.

Silvestrelli, P. L., 2008, Phys. Rev. Lett. **100**, 053002.

Silvestrelli, P. L., 2009a, Chem. Phys. Lett. **475**, 285.

Silvestrelli, P. L., 2009b, J. Phys. Chem. A **113**, 5224.

Silvestrelli, P. L., F. Ancilotto, and F. Toigo, 2000, Phys. Rev. B **62**, 1596.

Silvestrelli, P. L., K. Benyahia, S. Grubisic, F. Ancilotto, and F. Toigo, 2009, J. Chem. Phys. **130**, 074702.

Silvestrelli, P. L., N. Marzari, D. Vanderbilt, and M. Parrinello, 1998, Solid State Commun. **107**, 7.

Silvestrelli, P. L., and M. Parrinello, 1999a, J. Chem. Phys. **111**, 3572.

Silvestrelli, P. L., and M. Parrinello, 1999b, Phys. Rev. Lett. **82**, 3308.

Singh-Miller, N. E., 2009, Molecular-Scale Devices from First Principles, Ph.D. thesis (MIT).

Sit, P. H.-L., C. Bellin, B. Barbiellini, D. Testemale, J. L. Hazemann, T. Buslaps, N. Marzari, and A. Shukla, 2007, Phys. Rev. B **76**, 245413.

Skylaris, C. K., P. D. Haynes, A. A. Mostofi, and M. C. Payne, 2005, J. Chem. Phys. **122**, 084119.

Skylaris, C. K., A. A. Mostofi, P. D. Haynes, O. Dieguez, and M. C. Payne, 2002, Phys. Rev. B **66**, 035119.

Smirnov, V. P., R. A. Evarestov, and D. E. Usvyat, 2002, Int. J. Quantum Chem. **88**, 642.

Smirnov, V. P., and D. E. Usvyat, 2001, Phys. Rev. B **64**, 245108.

Soler, J. M., E. Artacho, J. D. Gale, A. Garcí, J. Junquera, P. Ordejón, and D. Sánchez-Portal, 2002, J. Phys. Condens. Matter **14**, 2745.

Solovyev, I. V., 2004, Phys. Rev. B **69**, 134403.

Solovyev, I. V., 2008, J. Phys. Condens. Matter **20**, 293201.

Solovyev, I. V., and M. Imada, 2005, Phys. Rev. B **71**, 045103.

Soluyanov, A. A., and D. Vanderbilt, 2011a, Phys. Rev. B **83**, 235401.

Soluyanov, A. A., and D. Vanderbilt, 2011b, Phys. Rev. B **83**, 035108.

Souza, I., J. Íñiguez, and D. Vanderbilt, 2002, Phys. Rev. Lett. **89**, 117602.

Souza, I., N. Marzari, and D. Vanderbilt, 2001, Phys. Rev. B **65**, 035109.

Souza, I., and D. Vanderbilt, 2008, Phys. Rev. B **77**, 054438.

Souza, I., T. Wilkens, and R. M. Martin, 2000, Phys. Rev. B **62**, 1666.

Spiegel, K., and P. Carloni, 2003, J. Phys. Chem. B **107**, 2091.

Spiegel, K., and A. Magistrato, 2006, Org. Biomol. Chem. **4**, 2507.

Sporkmann, B., and H. Bross, 1994, Phys. Rev. B **49**, 10 869.

Sporkmann, B., and H. Bross, 1997, J. Phys. Condens. Matter **9**, 5593.

Springer, M., and F. Aryasetiawan, 1998, Phys. Rev. B **57**, 4364.

Stengel, M., and N. A. Spaldin, 2006a, Phys. Rev. B **73**, 075121.

Stengel, M., and N. A. Spaldin, 2006b, Nature (London) **443**, 679.

Stengel, M., and N. A. Spaldin, 2007, Phys. Rev. B **75**, 205121.

Stengel, M., and N. A. Spaldin, 2008, Phys. Rev. B **77**, 155106.

Stengel, M., N. A. Spaldin, and D. Vanderbilt, 2009a, Nature Phys. **5**, 304.

Stengel, M., N. A. Spaldin, and D. Vanderbilt, 2009b, Nature Mater. **8**, 392.

Stengel, M., D. Vanderbilt, and N. A. Spaldin, 2009, Phys. Rev. B **80**, 224110.

Stephan, U., R. M. Martin, and D. A. Drabold, 2000, Phys. Rev. B **62**, 6885.

Strange, M., I. S. Kristensen, K. S. Thygesen, and K. W. Jacobsen, 2008, J. Chem. Phys. **128**, 114714.

Subotnik, J. E., A. Sodt, and M. Head-Gordon, 2007, Phys. Chem. Chem. Phys. **9**, 5522.

Sullivan, D. M., K. Bagchi, M. E. Tuckerman, and M. L. Klein, 1999, J. Phys. Chem. A **103**, 8678.

Sulpizi, M., and P. Carloni, 2000, J. Phys. Chem. B **104**, 10 087.

Sulpizi, M., A. Laio, J. VandeVondele, A. Cattaneo, U. Rothlisberger, and P. Carloni, 2003, Proteins: Struct., Funct., Genet. **52**, 212.

Sulpizi, M., P. Schelling, G. Folkers, P. Carloni, and L. Scapozza, 2001, J. Biol. Chem. **276**, 21 692.

Suzuki, K., H. Usui, and K. Kuroki, 2011, J. Phys. Soc. Jpn. **80**, 013710.

Suzuki, T., 2008, Phys. Chem. Chem. Phys. **10**, 96.

Taflove, A., and S. C. Hagness, 2005, *Computational electrodynamics: the finite-difference time-domain method* (Artech House, Norwood, MA), 3rd ed.

Takeda, H., A. Chutinan, and S. John, 2006, Phys. Rev. B **74**, 195116.

Tang, H., and S. Ismail-Beigi, 2009, Phys. Rev. B **80**, 134113.

Taraskin, S. N., D. A. Drabold, and S. R. Elliott, 2002, Phys. Rev. Lett. **88**, 196405.

Thomas, H., and K. A. Muller, 1968, Phys. Rev. Lett. **21**, 1256.

Thonhauser, T., D. Ceresoli, A. A. Mostofi, N. Marzari, R. Resta, and D. Vanderbilt, 2009, J. Chem. Phys. **131**, 101101.

Thonhauser, T., D. Ceresoli, D. Vanderbilt, and R. Resta, 2005, Phys. Rev. Lett. **95**, 137205.

Thonhauser, T., and D. Vanderbilt, 2006, Phys. Rev. B **74**, 235111.

Thouless, D. J., 1983, Phys. Rev. B **27**, 6083.

Thygesen, K. S., L. B. Hansen, and K. W. Jacobsen, 2005a, Phys. Rev. Lett. **94**, 026405.

Thygesen, K. S., L. B. Hansen, and K. W. Jacobsen, 2005b, Phys. Rev. B **72**, 125119.

Thygesen, K. S., and K. W. Jacobsen, 2005, Chem. Phys. **319**, 111.

Tindemans-van Eijndhoven, J. C. M., and C. J. Kroese, 1975, J. Phys. C **8**, 3963.

Tkatchenko, A., and M. Scheffler, 2009, Phys. Rev. Lett. **102**, 073005.

Tobias, D. J., P. Jungwirth, and M. Parrinello, 2001, J. Chem. Phys. **114**, 7036.

Todorova, T., P. H. Hunenberger, and J. Hutter, 2008, J. Chem. Theory Comput. **4**, 779.

Todorova, T., A. P. Seitsonen, J. Hutter, I. F. W. Kuo, and C. J. Mundy, 2006, J. Phys. Chem. B **110**, 3685.

Trimarchi, G., I. Leonov, N. Binggeli, D. Korotin, and V. I. Anisimov, 2008, J. Phys. Condens. Matter **20**, 135227.

Trombettoni, A., and A. Smerzi, 2001, Phys. Rev. Lett. **86**, 2353.

Tse, J. S., 2002, Annu. Rev. Phys. Chem. **53**, 249.

Tuckerman, M. E., 2002, J. Phys. Condens. Matter **14**, R1297.

Tuckerman, M. E., and G. J. Martyna, 2000, J. Phys. Chem. B **104**, 159.

Uehara, K., and J. S. Tse, 2000, Phys. Rev. B **61**, 1639.

Umari, P., and N. Marzari, 2009, J. Chem. Phys. **131**, 094104.

Umari, P., and A. Pasquarello, 2002, Phys. Rev. Lett. **89**, 157602.

Umari, P., and A. Pasquarello, 2003, Phys. Rev. B **68**, 085114.

Umari, P., G. Stenuit, and S. Baroni, 2009, Phys. Rev. B **79**, 201104.

Umari, P., A. J. Williamson, G. Galli, and N. Marzari, 2005, Phys. Rev. Lett. **95**, 207602.

Usui, H., R. Arita, and K. Kuroki, 2009, J. Phys. Condens. Matter **21**, 064223.

Usui, H., S. Shibata, and K. Kuroki, 2010, Phys. Rev. B **81**, 205121.

Usvyat, D. E., R. A. Evarestov, and V. P. Smirnov, 2004, Int. J. Quantum Chem. **100**, 352.

Vanderbilt, D., and R. D. King-Smith, 1993, Phys. Rev. B **48**, 4442.

Vanderbilt, D., and R. Resta, 2006, in *Conceptual foundations of materials properties: A standard model for calculation of ground- and excited-state properties*, edited by S. G. Louie and M. L. Cohen, Contemporary Concepts of Condens. Matt. Science Vol. 1 (Elsevier, New York), p. 139.

van Erp, T. S., and E. J. Meijer, 2003, J. Chem. Phys. **118**, 8831.

Vaucher, B., S. R. Clark, U. Dorner, and D. Jaksch, 2007, New J. Phys. **9**, 221.

Volja, D., B. Kozinsky, A. Li, D. Wee, N. Marzari, and M. Fornari, 2012, Phys. Rev. B **85**, 245211.

von Niessen, W., 1972, J. Chem. Phys. **56**, 4290.

Vuilleumier, R., 2006, in *Computer Simulations in Condens. Matt. Systems: from Materials to Chemical Biology*, edited by M. Ferrario, G. Ciccotti, and K. Binder (Springer, New York), Vol. 1.

Vuilleumier, R., and M. Sprik, 2001, J. Chem. Phys. **115**, 3454.

Waghmare, U. V., and K. M. Rabe, 1997, Phys. Rev. B **55**, 6161.

Wahn, M., and J. Neugebauer, 2006, Phys. Status Solidi B **243**, 1583.

Wang, X., J. R. Yates, I. Souza, and D. Vanderbilt, 2006, Phys. Rev. B **74**, 195118.

Wang, X., J. R. Yates, D. Vanderbilt, and I. Souza, 2007, Phys. Rev. B **76**, 195109.

Wannier, G. H., 1937, Phys. Rev. **52**, 191.

Watkins, G. D., and R. P. Messmer, 1974, Phys. Rev. Lett. **32**, 1244.

Weber, C., K. Haule, and G. Kotliar, 2010, Phys. Rev. B **82**, 125107.

Whittaker, D. M., and M. P. Croucher, 2003, Phys. Rev. B **67**, 085204.

Williamson, A. J., R. Q. Hood, and J. C. Grossman, 2001, Phys. Rev. Lett. **87**, 246406.

Wu, X., M. Stengel, K. M. Rabe, and D. Vanderbilt, 2008, Phys. Rev. Lett. **101**, 087601.

Wu, X. F., O. Dieguez, K. M. Rabe, and D. Vanderbilt, 2006, Phys. Rev. Lett. **97**, 107602.

Wu, X. F., A. Selloni, and R. Car, 2009, Phys. Rev. B **79**, 085102.

Wu, Y., 2004, Molecular Dynamics Study of Chemical Reactions, Ph.D. thesis (Princeton University).

Xia, Y., *et al.*, 2009, Nature Phys. **5**, 398.

Xiao, D., M.-C. Chang, and Q. Niu, 2010, Rev. Mod. Phys. **82**, 1959.

Xiao, D., J. Shi, and Q. Niu, 2005, Phys. Rev. Lett. **95**, 137204.

Yablonovitch, E., 1987, Phys. Rev. Lett. **58**, 2059.

Yamauchi, K., F. Freimuth, S. Blügel, and S. Picozzi, 2008, Phys. Rev. B **78**, 014403.

Yang, H., *et al.*, 2008, Phys. Rev. Lett. **101**, 067001.

Yang, W., 1991, Phys. Rev. Lett. **66**, 1438.

Yao, Y., L. Kleinman, A. H. MacDonald, J. Sinova, T. Jungwirth, D.-S. Wang, E. Wang, and Q. Niu, 2004, Phys. Rev. Lett. **92**, 037204.

Yariv, A., Y. Xu, R. K. Lee, and A. Scherer, 1999, Opt. Lett. **24**, 711.

Yates, J. R., X. Wang, D. Vanderbilt, and I. Souza, 2007, Phys. Rev. B **75**, 195121.

Yazyev, O. V., E. Kioupakis, J. E. Moore, and S. G. Louie, 2012, Phys. Rev. B **85**, 161101(R).

Yazyev, O. V., J. E. Moore, and S. G. Louie, 2010, Phys. Rev. Lett. **105**, 266806.

Yee, K. S., 1966, IEEE Trans. Antennas Propag. **14**, 302.

Yukalov, V. I., 2009, Laser Phys. **19**, 1.

Zhang, H., F. Freimuth, S. Blügel, Y. Mokrousov, and I. Souza, 2011, Phys. Rev. Lett. **106**, 117202.

Zhang, H. J., C. X. Liu, X. L. Qi, X. Dai, Z. Fang, and S. C. Zhang, 2009, Nature Phys. **5**, 438.

Zhang, H.-J., S. Chadov, L. Muchler, B. Yan, X.-L. Qi, J. Kubler, S.-C. Zhang, and C. Felser, 2011, Phys. Rev. Lett. **106**, 156402.

Zhang, H.-J., C.-X. Liu, X.-L. Qi, X.-Y. Deng, X. Dai, S.-C. Zhang, and Z. Fang, 2009, Phys. Rev. B **80**, 085307.

Zhang, W., R. Yu, H.-J. Zhang, X. Dai, and Z. Fang, 2010, New J. Phys. **12**, 065013.

Zhong, W., D. Vanderbilt, and K. M. Rabe, 1994, Phys. Rev. Lett. **73**, 1861.

Zhong, W., D. Vanderbilt, and K. M. Rabe, 1995, Phys. Rev. B **52**, 6301.

Zicovich-Wilson, C. M., R. Dovesi, and V. R. Saunders, 2001, J. Chem. Phys. **115**, 9708.

Zurek, E., O. Jepsen, and O. K. Andersen, 2005, Chem. Phys. Chem. **6**, 1934.